

POLITECNICO DI TORINO

CORSO DI LAUREA MAGISTRALE IN INGEGNERIA DEI MATERIALI

MASTER THESIS

Fabrication and characterization of SOC single repeating units: implementation of glass-ceramic sealants



Accademic Supervisor:

Prof. Federico Smeacetto
Prof. Milena Salvo

Candidate:

Diego Orifici

IREC Supervisor:

Prof. Albert Tarancón
Dr. Antonio Gianfranco Sabato
Dr. Lucile Bernadet

Summary

Summary	3
1. Introduction	5
1.1 Fuel Cells	7
2. Solid Oxide Fuel Cells (SOFC)	9
2.2 SOFC stacks components: materials and properties	11
2.2.1 Electrolyte	12
2.2.2. Anode materials	13
2.2.3 Cathode materials	14
2.2.4 Interconnect materials	15
2.2.5 Protective Coatings	16
2.2.6 Sealants	18
2.2.6.1 Glass-ceramic sealants.....	20
3. Experimental	22
3.1 SRU elements and materials	22
3.1.1 Sealants	23
3.1.2 Solid oxide cell	25
3.1.3 Interconnector	26
3.1.4 Endplate	26
3.2 Glass Deposition by Robocasting	27
General principles and “Machine Explanation”	27
3.3 Materials Characterization	32
3.3.1 Base Materials characterization	32
3.3.2 Compatibility tests	33
3.3.5 MC12 characterization.....	40
3.4 Single cells and SRU characterization	41
3.4.2 Single Cell Assembly.....	43
3.4.2 SRU Assembly.....	44
3.4.3 Test Station	46
3.5 Test Procedure	48
4. Results	50
4.1 Materials Characterization	50
4.1.1 Glass Characterization	50
4.1.2 Compatibility tests	53
4.1.3 Coating characterization	61
4.2 Single cell and SRU characterization	64
4.2.1 Test 1.....	64
4.2.2 Test 2.....	66
4.2.3 Test 3.....	69
4.2.4 Test 4.....	72
5. Conclusions and future development	76
6. Bibliography	77
7 Ringraziamneti	80

Abstract

Nowadays, there is an evident interest and demand of the industrial and domestic energy sectors to start the energy transition from fossil fuels-based energies to renewable sources. New and efficient clean power have to be implemented and Solid Oxide Fuel Cells (SOFC) are a suitable candidate to address this challenge. SOFC stacks are composed by several elements (cells, interconnects, endplates, sealants) that need to be optimized in order to maximize their performance.

This work presents the implementation of glass-ceramic sealants in the setup used for large area SOFC cells, single repeating units (SRU) and stack tests at IREC. Two commercial sealants were studied, one produced by tape-casting (sealant 1) and another in form of powder (sealant 2) that was deposited by robocasting. As a first step the compatibility of these sealants with other materials involved in SRU/stack at IREC was tested. Both sealants showed excellent compatibility with all the interfaced counterparts: bare and coated Crofer22APU, bare and coated IC, anode of the cell, electrolyte of the cell.

Large-area single cells and SRU were then tested in fuel cell mode performing polarization curves, electrochemical impedance spectroscopy and durability tests. Even though single cell characterization was not successful probably due to gas overpressure leading to important leakages, SRU characterization using with either sealant 1 or sealant 2 led to good results. In both cases, good OCV values were obtained, corresponding to limited leakages between the anode and cathode chambers and proves the effectivity of the tested glass-sealants. Polarization curves allowed to reach 0,3-0,4 A/cm² at 0.7 V. Finally, a durability test of 800 h could be performed at 800°C for the SRU made with robocasted sealant 2. Higher degradation rate was observed during the first 300 h (8,4 %) and then decreased to 3-4 %.

1. Introduction

Nowadays, one of the most important topics is the “Climate Change Challenge” [1]. Sustainability is the key to avoid the pollution, which is unlikely increased during these years. Moreover, many activities and a really big quantity of problems involved to serious and dramatic situation, putting at risk the whole world’s health. For this reason, we are going to focus on news sustainable technologies, which actually implement and try to get better our situation.



Figure 1: Challenge Climate Change [1]

The Paris Agreement set a maximum level of emissions, to obtain a global average temperature less than 2°C above pre-industrial levels, decreasing the value to 1,5°C [2]. In relation to these aspects, there is the need to invest in low-carbon energy production technologies, since carbon-based energy production is considered to be responsible of circa two-thirds of global emissions. International Renewable Energy Agency estimates that renewable energy sector could provide 90% of the CO₂ emissions reductions needed by 2050 [3]. Observing figure 2 it is possible to understand the importance of renewable energies, which increase in year by year. There are different kinds of promising technologies.

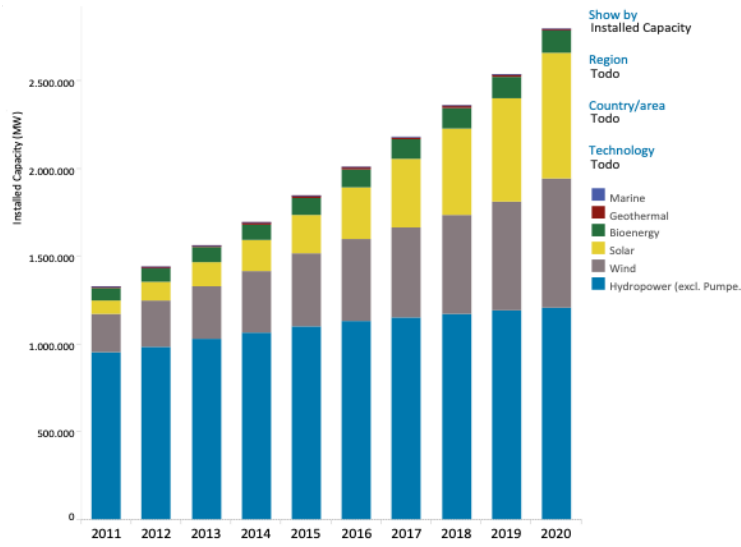


Figure 2: Installed Capacity Trends [3]

Among different technologies, fuel cells represent a promising solution in order to produce clean energy with high efficiencies (figure 3). Fuel cells can potentially lead to a carbon-free scenario thanks to their applications in different field: domestic, automotive, backup generators, auxiliary power generation.

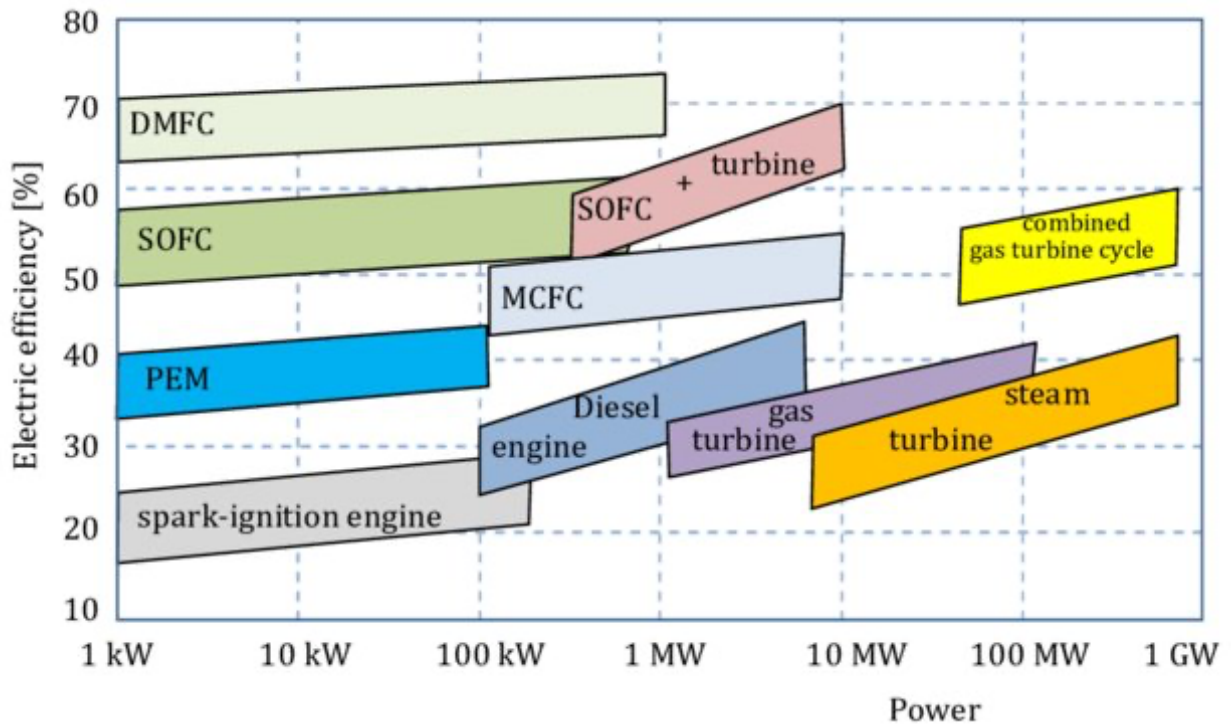


Figure 3: efficiency comparison between Fuel Cell and conventional energy production technologies [4]

1.1 Fuel Cells

The wide use of harmless gas, like Hydrogen or methane, from biogas has obtained an incredible success applied to Fuel cells. These devices are able to convert the electrochemical energy into electric energy, through electrochemical reactions avoiding any type of combustion. In a typical Fuel Cell, the main actors of this process are three: two electrodes (anode and cathode) where the electrochemical reactions occur and one electrolyte that act as separator between the electrodes and allows the ionic transportation from one electrode to the other. The electrolyte, anode and cathode together form a single cell unit. As it is possible to see by figure 4, there are different kinds of Fuel Cells depending on the materials and reactions involved. The Figure depicts the reactions and typical working temperatures for each kind of fuel cells technology. Moreover, the level of temperature is linked to the efficiency of a single cell.

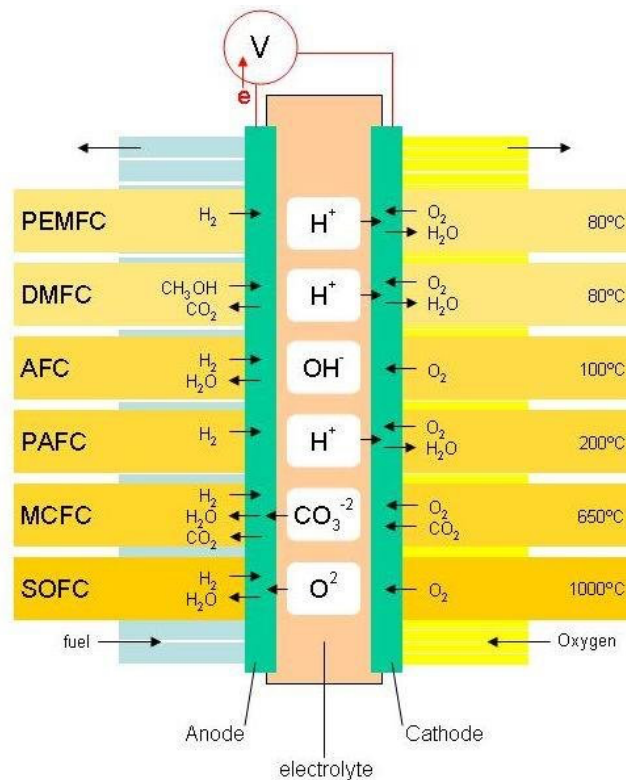


Figure 4: Fuel Cell types and reaction temperatures [5]

The main way to obtain useful performance is to connect many cells, to set up a system of them, that is called “stack “. Below this paragraph there are different types of fuel cells:

1. **PEMFC** : Proton Exchange Membrane FC
2. **DMFC**: Direct Methanol FC
3. **AFC**: Alkaline FC
4. **PAFC**: Phosphoric Acid FC
5. **MCFC**: Molten Carbonate FC
6. **SOFC**: Solid Oxide FC

For each kind of Fuel Cell, there are different reactions at the cathode and anode side, which are shown in the *table 1*:

Table 1: typical reactions occurring at the electrodes in different kinds of Fuel Cell [6]

Fuell Cells	Anode Reaction	Cathode Reaction
AFC	$H_2 + 2OH^- \rightarrow 2 H_2O + 2e^-$	$O_2 + 2H_2O + 4e^- \rightarrow 4 OH^-$
PAFC	$H_2 \rightarrow 2H^+ + 2e^-$	$O_2 + 4H^+ + 4e^- \rightarrow 2 H_2O$
PEMFC	$H_2 + CO_3^{2-} \rightarrow H_2O + CO_2 + 2e^-$ $CO + CO_3^{2-} \rightarrow 2CO_2 + 2e^-$	$O_2 + 4H^+ + 4e^- \rightarrow 2 H_2O$
MCFC	$H_2 + O^{2-} \rightarrow H_2O + 2e^-$	$O_2 + 2 CO_2 + 4e^- \rightarrow 2CO_3^{2-}$
SOFC	$CO + O^{2-} \rightarrow CO_2 + 2e^-$	$O_2 + 4e^- \rightarrow 2 O^{2-}$

Despite low temperature fuel cells (i.e. AFC, PAFC or PEMFC) may seem more attractive thanks to the lower temperatures required it is necessary to specify that they require noble metals-based catalysts and that they can be used only if H₂ is involved as fuel. This since at lower temperatures only H₂ has a usable electrochemical potential. The use of different fuels in low T fuel cells is possible only if an external reformer is implemented but, in any case, carbon-containing fuels may lead to electrodes poisoning and to a consequent decreasing in the cells performances.

2. Solid Oxide Fuel Cells (SOFC)

As mentioned in the previous paragraph, SOFC usually work on a temperature range between 700 - 1000 °C because they are based on the ionic conductivity of ceramic materials. As described in Figure 5 Figure 5 and the video available through the QRcode 1, the air is reduced at the cathode into oxygen anions. Those anions are conducted by the electrolyte to the anode, where they oxidize a fuel like H_2 . This reaction produces H_2O and liberates the electrons that will flow into the external circuit and generate power. The electrodes are just catalyzing the redox reaction, which allows a continuous operation of fuel cells as long as the reactive are provided to the cell. On the contrary, redox reactions taking place inside batteries are directly involving the electrodes' materials, corresponding to an important limitation in term of continuous operation.

Operating at high temperatures presents several advantages like operating with fuels that are not highly pure or avoiding the use of precious metals as catalysts. Moreover, by increasing the temperature, the cell operating voltage decreases, which allows to obtain a high efficiency around 50-60 % [4]

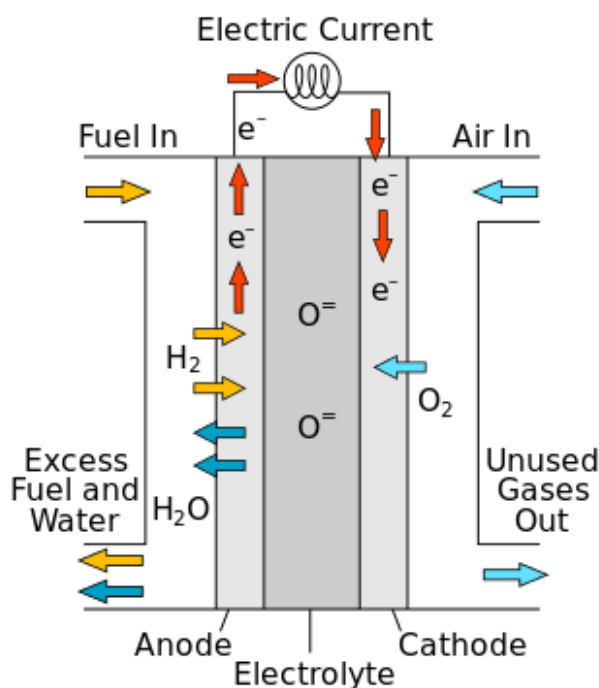
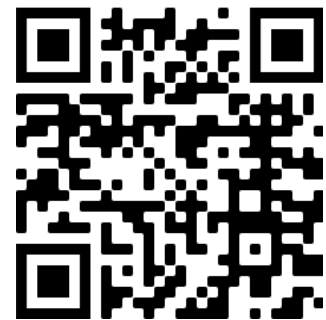


Figure 5: Typical functioning of SOFC [7]



QRcode 1: SOFC Explained with animation

2.1 SOFC designs

In order to reach high power, several SOFC are assembled into stacks by connecting the cells in series. The number of cells can change regarding the application and the desired power. Moreover, stacks can be connected in parallel if higher power is necessary.

Different designs of SOFC are used to build up the stacks, which are briefly presented in **Errore. L'origine riferimento non è stata trovata.:**

- **Tubular:** the cell has a tube shape where one electrode is the inner part and the other electrode on the outer part. Cells can be connected in series or parallel.
- **Segmented:** cells are supported by an insulating material allowing the use of thin electrode. Cells are placed in series on top of the same support.
- **Monolithic:** corrugated cells are assembled to favor the gas circulation.
- **Planar:** planar cells are stacked in series with interconnectors (IC) in between in order to separate the gas atmospheres and conduct the electrons from one cell to the other. This design is the most common one.

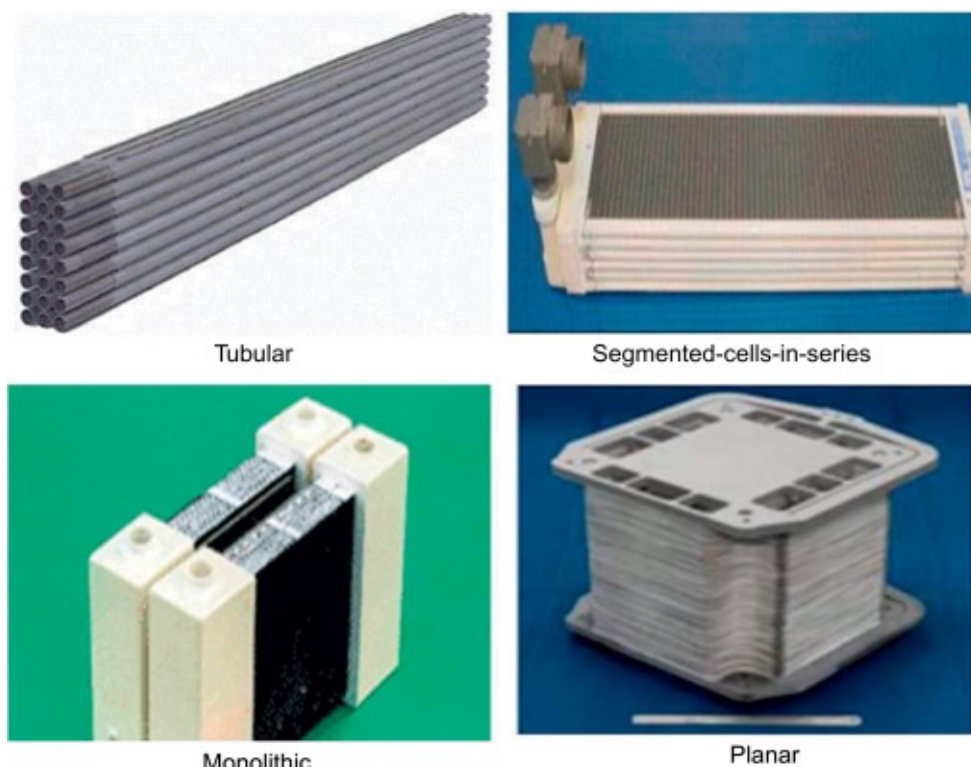


Figure 6: Examples of SOFC stacks of different designs [8]

As the planar design is the most common design and the one that will be studied in this work, a schematic representation is shown in Figure 7. The cell is sandwiched between two IC with main functions are the fuel and air separation from the anode of the lower cell and the cathode of the upper cell respectively and the current conduction. Moreover, it can be seen that the IC have channels that help the gas distribution. It is not visible in this figure but the use of sealants is also mandatory between the cells and IC to make sure the gas cannot escape from the chamber where it has to flow. The sandwich of one cell between two IC is the principal element that is repeated in a stack and is then called cell repeat unit or, more commonly, Single Repeating Unit (SRU).

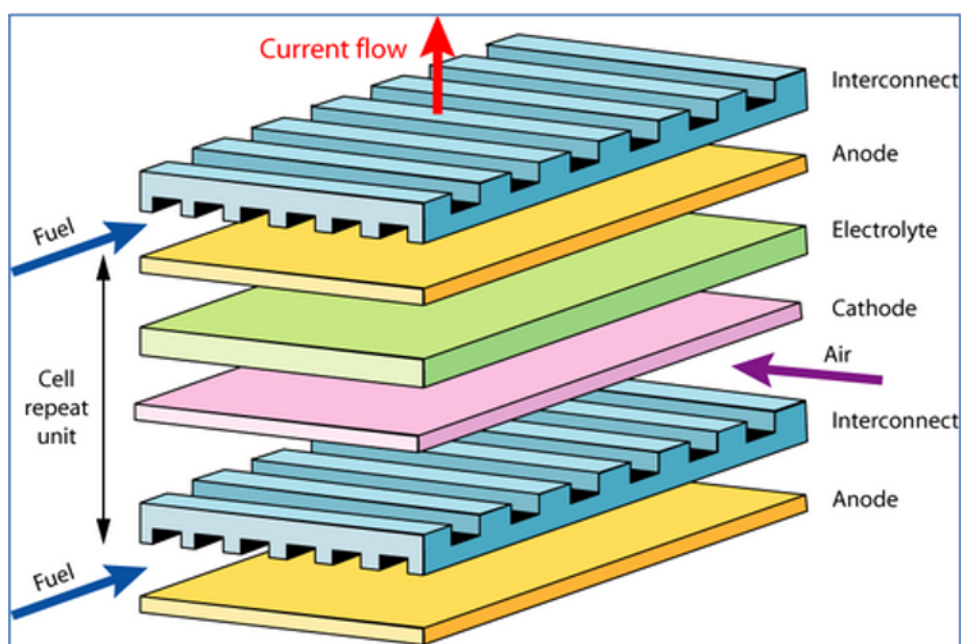


Figure7: Schematic representation of a SOFC SRU [9]

There are plenty of researches focused on finding out new niche materials, getting better and adopting their performance for this application.

2.2 SOFC stacks components: materials and properties

Due to the high working temperatures, materials that can be used for the different components are limited to metals and ceramics. Figure 8 presents an overview of the different materials used for SOFC cells, interconnects and seals [10]. All of those materials were developed in order to obtain higher performances, overcome degradation issues or secondary phase formation between the layers,

etc... The next paragraphs will describe the state-of-the-art materials and more specifically the ones present in the components used in this work.

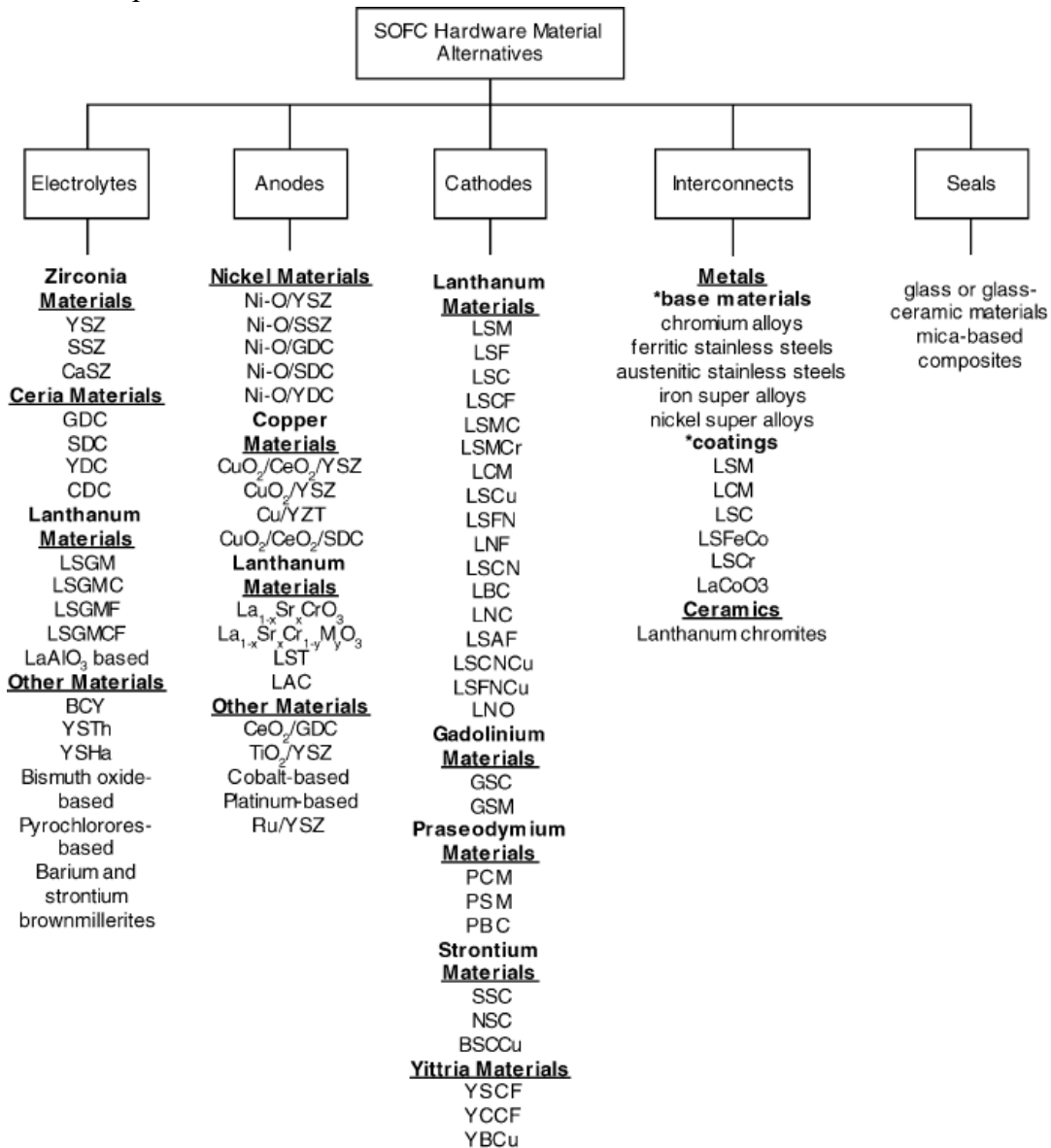


Figure 8: Materials used for SOFC components [10]

2.2.1 Electrolyte

The electrolyte main role is to conduct the oxygen anions from the cathode to the anode. It also has to avoid gas mixing between the anodic and cathodic gas chambers, meaning that this layer needs to be dense. In addition, others important properties are listed below [11]:

- Electronically insulating
- Chemically stable at high temperatures

- Chemically stable in reducing and oxidizing environments
- Production as a uniformly thin layer (to minimize ohmic losses)
- Thermal expansion that matches the electrodes ones
- Use of inexpensive materials

Actually, it is possible to divide electrolyte materials in two groups: fluorite or perovskite structure electrolytes. The first one has face-centered cubic arrangement. It shows an open structure with interstitial voids, which help rapid oxygen diffusion. One of the materials that meets all the criteria, is yttria stabilized zirconia ($Y_2O_3-ZrO_2$, YSZ). It is an excellent oxide-ion conductivity at temperature around 800 °C and can be easily manufacture in form of thin dense layers (5-20 μm) by tape-casting [12]. The second type of electrolyte has a perovskite crystal structure, with formulation ABO_3 . One of the most common one is $La_{1-x}Sr_xGa_{1-y}Mn_yO_3$ (Lanthanum Gallate doped with Strontium Oxide and Magnesium Oxide). This configuration offers an ionic and electronic conductivity higher than YSZ. Indeed, that structure results to be one of the most promising for these devices even though stability issues still need to be solved.

In addition, both type of electrolyte materials usually requires the addition of a thin barrier layer made of another ionic conductor (gadolinium doped ceria, $Ce_{1-x}Gd_xO_2$) to improve the compatibility between the electrolyte and the electrodes by preventing the inter diffusion of some ions, especially Zr and La from the electrolyte and Sr from the cathode [12].

2.2.2. Anode materials

The anode or commonly called “fuel electrode” allows to carry out the oxidation of the fuel. To occur, the reaction has to take place at Triple Phase Boundaries (TPB) where the oxygen anions meet the fuel molecules and evacuate the electrons. Those TPB can only be present if the electrode presents simultaneously electrical conductivity, ionic conductivity and pores where the gas can circulate. Moreover, the perfect anode candidate also has to present the following properties [13]:

- High electrocatalytic activity
- Avoid coke deposition
- Stable in a reducing environment
- Can be made thin enough to avoid mass transfer losses, but thick enough to provide area and distribute current
- Able to provide mechanical support to electrolyte and cathode if the cell is anode supported
- Thermal expansion coefficient (CTE) similar to the neighboring cell components (electrolyte, IC)
- Chemically compatible with neighboring cell components
- Present a fine particle size
- Use of relatively inexpensive materials.

As seen Figure 8, Ni-based anodes are the most common SOFC fuel electrodes. Despite pure nickel has a CTE too high compare to the typical YSZ electrolyte CTE, it is widely used in this application, but under shape of ceramic-metal composite called cermet material. In this case the nickel will be the electronic conductor and the ceramic material, YSZ in general, will conduct the oxygen ions. It includes 40-60% of nickel particles mixed with YSZ. Nickel has different excellent characteristics, matching with some parameters listed before like the affordable cost, chemical stability and catalytic activity. Cermet electrodes are fabricated to present a porosity in the range of 20-40 % to facilitate the gas flow and increase the amount of TPB [14]. However, some limitations are now well known for this type of material as Ni agglomeration after thousands of hours of operation due to the tendency to grow and aggregate at high temperature, Ni particles desactivation or re-oxidation [15].

2.2.3 Cathode materials

The cathode or commonly air electrode is where the reduction reaction takes place. As for the anode, the cathode must present TPBs where oxygen ions, electrons and oxygen molecules can react. Moreover, there are others important requirements for a cathode [13]:

- Chemically compatible with neighboring cell components (especially with electrolyte and IC)
- Can be made thin and porous (thin enough to avoid mass transfer losses, but thick enough to provide area and distribute current)
- Stable in an oxidant environment
- Thermal expansion coefficient similar to other SOFC materials
- Affordable material

The most common cathode materials, considering those parameters, are perovskites with crystal formula ABO_3 [16]. The first oxygen electrodes were made of substituted manganites, mainly co-doped with strontium and lanthanum (LSM). As this perovskite has poor ionic conductivity, LSM was mixed with YSZ to provide higher ionic conductivity to the oxygen electrodes. However, delamination of the electrode as well as poor performance at intermediate temperature were reported, which led to develop other type of perovskites [17]. Mixed ionic electronic conductor (MIEC) perovskites like lanthanum strontium cobalt iron oxide ($La_{1-x}Sr_xCo_{1-y}FyO_3$) were proposed to increase the quantity of reactive sites by having the whole surface in contact with the gas able to host the reaction. Its ionic conductivity comes from the lower valent cation used to dope the A-site [18]. Another studied configuration to increase the electrode performance is based on making composites of LSCF and CGO by directly mixing the powder before the electrode deposition or by developing backbone structures of one material that are infiltrated with a solution containing the other material [19]. Degradation phenomena reported for those electrodes are mainly the cation segregation like Sr from the LSCF structure to react with Zr from the electrolyte and the cathode poisoning by Cr coming from the IC, which will be described in the paragraph 2.1.3 [17].

2.2.4 Interconnect materials

The interconnect plays a crucial role in a SOFC stack, mainly for two aspects: 1) it separates the anode side of one cell from the cathode side of the following one, thus avoiding gas mixing; 2) it provides electrical connection between two consecutive cells in a stack. Considering the severe working conditions, it is not easy to find the perfect material candidate. Ideally a good interconnect material should have the following characteristics [20]:

- Chemically stable with others stack components especially at high temperatures for prolonged times (600-1000 °C up to 40000 h);
- High electrical conductivity;
- Thermal expansion coefficient similar to other SOFC materials;
- Low cost (raw material and processing);

In the past, ceramic materials were usually selected for this component, especially because the working temperatures were $T > 1000$ °C. In this condition, the best materials candidate were rare earth chromites, like LaCrO_3 , doped with Sr, Mg or Ca.

In the last decades the general trend was to lower the operating temperatures (600-800 °C) of SOC, which correspond in a first instance to an advantage in terms of costs and time, and in a second instance to the possibility to wide the materials selection. For this reason, metallic materials started to be investigated as interconnect materials. Also, thanks to their easier manufacturing process (even for complex shapes), lower constant electrical conductivity [13,21]. Specific metallic alloys were investigated in order to resist to the harsh SOC operating environment (oxidizing and reducing atmospheres and high temperatures) with the main objective to avoid corrosion phenomena.

Among the best materials candidates, there are Chromia-forming alloys (such as Crofer22APU and Crofer22H stainless steels). These alloys typically form a coherent Cr_2O_3 scale that protect the underlying alloy from excessive and uncontrolled corrosion, limiting oxygen penetration, despite high temperatures and oxidizing environments. [21]. However, an excessive growth in the thickness of oxide scale may be detrimental for two main reasons: firstly, because it has a lower electrical conductivity compared with the bare metals, so the overall resistance increases with the increasing thickness, secondly it may have an excessive difference in the CTE in comparison with the underlying alloy leading to spallation of the scale and consequently catastrophic corrosion in the operating conditions. In *figure 11* it is possible to see a common example of this phenomenon.

Moreover, at the same time, chromium evaporation occurs through the formation of Cr-containing volatile species such as $\text{CrO}_2(\text{OH})_2$. A common problem related to the evaporation of these compounds is the Cathode poisoning. This phenomenon occurs when Cr-containing volatile species react with the cathode resulting in the deposition of solid poisoning compounds (i.e. CrMn_2O_4) in the cathode and specifically at the three-phase boundary, thus leading to a drastic decrease of Cell

performance. This is due not only to a decreasing in the cathode porosity but also to the occlusion of the active sites for oxygen reduction at the three phase boundaries.

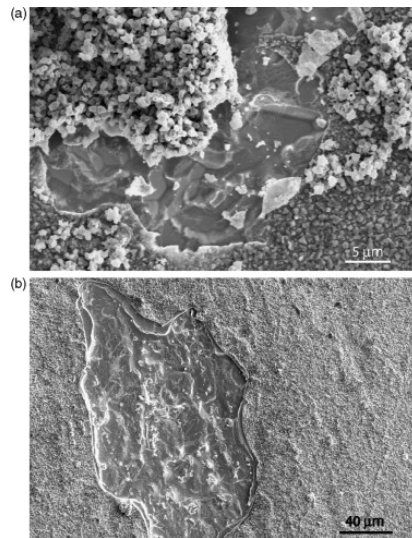


Figure 11: Spallation with an oxidation treatment for (a) 14h and (b) 170 at 800 °C [22].

One of the most used solution to limit these phenomena is the deposition of protective coatings on the surface of the interconnects which should at physical barrier against the diffusion of oxygen towards the interconnect and evaporation of Cr-containing species from it. This, on one side limits the excessive growth of Cr_2O_3 scale and on the other prevents cathode poisoning. [23].

2.2.5 Protective Coatings

As mentioned in the previous paragraph, deposition of protective coatings on metallic interconnect is necessary for two reasons: to limit the growth of Cr_2O_3 and to avoid cathode poisoning. In order to be suitable for these applications a good protective layer should possess the following characteristics [24]:

- High electrical conductivity;
- Good CTE match with others materials;
- Possibility to apply simple and economic deposition techniques;
- Sufficient thickness and densification in order to act as a barrier;

Considering all these aspects, some spinel-based compounds have attracted the attention as valid candidates. The general spinel formula can be written as AB_2O_4 , where changing the cations in A and B positions or their ratio, it is possible to obtain an increase the electronic conductivity and to tune the CTE of the materials [25]. Among the different spinel compositions investigated in recent years, a predominant role is occupied by $(\text{Mn},\text{Co})_3\text{O}_4$ based spinels. In particular MnCo_2O_4 composition

demonstrated excellent CTE match with the other involved materials ($\approx 9.7 \cdot 10^{-6} \text{ }^\circ\text{C}^{-1}$) and electrical conductivity at 800°C ($\approx 60 \text{ S cm}^{-1}$) [26]. $(\text{Mn,Co})_3\text{O}_4$ spinel based coatings have been deposited successfully with different techniques (i.e. electrophoretic deposition, dip-coating, plasma spray, sputtering and others). Furthermore, this material is very prone to achieve a satisfactory densification and thus excellent barrier performances. In *figure 12* for example it is represented the morphological and compositional analysis of a $(\text{Mn,Co})_3\text{O}_4$ spinel based coating deposited on Crofer22APU stainless steel. The coating appears to be very dense and able to confine the Cr at the interface with the underlying metal even after an aging in static air at 800°C . Another relevant example of coating densification is illustrated in the fig 13, where the coating shows a progressive improvement in terms of densification after the thermal treatments. This example in particular show the beneficial impact of a reducing step that improves the densification thanks to the formation of metallic Co and MnO.

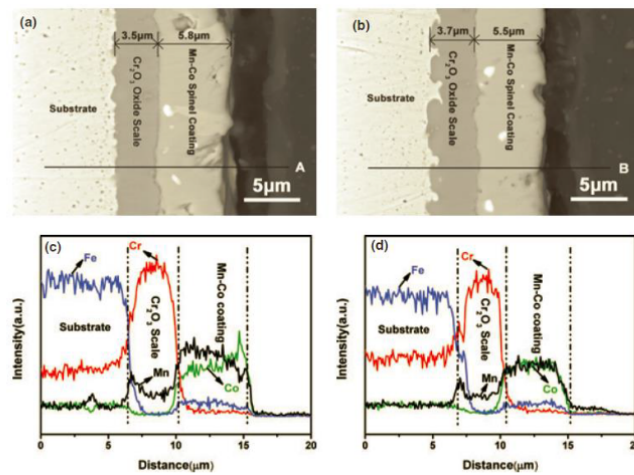


Figure 12: SEM and EDX views of Mn-Co coating with Crofer 22 APU (a) before and (b) after an oxidation treatment at 800°C for 120 h [27].

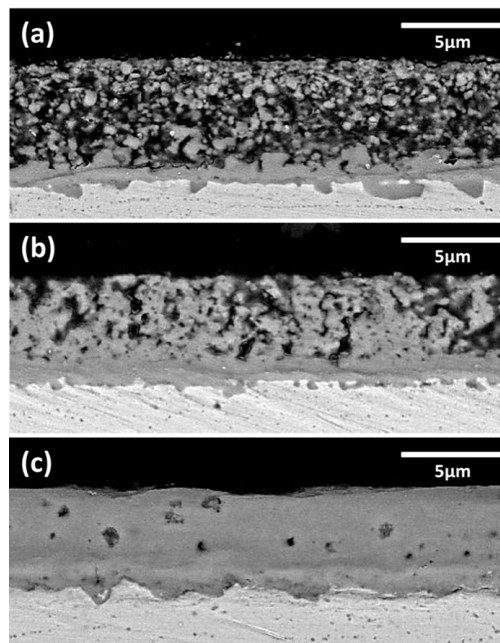


Figure 13: SEM picture of $\text{Mn}_{1.5}\text{Co}_{1.5}\text{O}_4$ coatings deposited on Crofer22APU after different treatments: 800°C in static air (a), 1000°C in reduction atmosphere of $\text{N}_2\text{-H}_2$ (4% H_2) (b), after a re-oxidation at 800°C in air (c)[28].

As anticipated before, another important role of protective coatings for IC in SOC application is to limit the excessive growth of the Cr_2O_3 scale on the metal. One of the reasons related to this, is the relatively lower electrical conductivity of this scale in comparison with the metallic interconnect and the coating itself. A way to evaluate the impact of chromia scale growth on the electrical performances of the interconnect, is to measure the area specific resistance (ASR) of interconnects in real operating conditions (oxidizing atm. for prolonged periods at 700-900 °C). For example, in *figure 14* it is possible to see the effect of the protective coatings on Crofer22APU. The ASR for the coated sample remained stable for the duration of the test (2500h), on the contrary the uncoated Crofer22APU shows a strong increase of this value, this is due to the growth of the oxide scale.

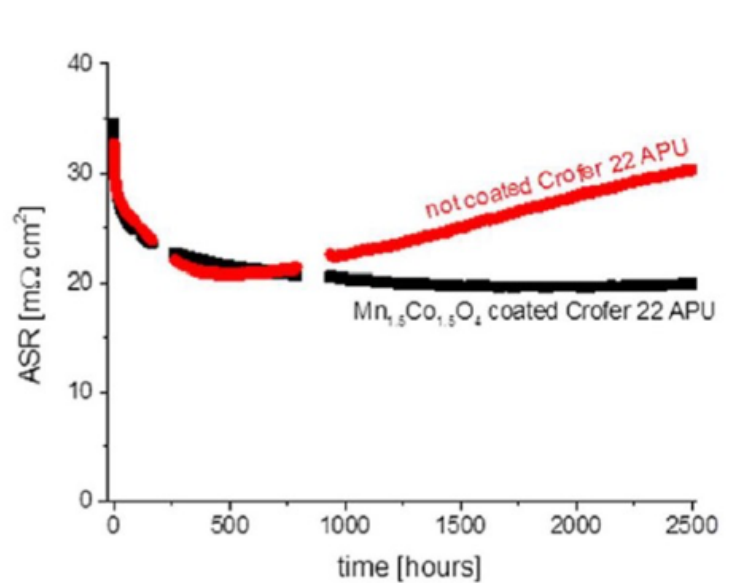


Figure 14: Comparison between not coated Crofer 22 APU and coated Crofer 22 APU in terms of ASR, under $500 \text{ mA} \cdot \text{cm}^{-2}$ current load in air [29].

2.2.6 Sealants

In a typical SOC planar stack configuration the use of sealants is necessary, in order to prevent gases mixing. The overall performance of a SOC stack is strictly related to the role of the sealant for the entire working life of the device. Indeed, a failure in the sealant may lead not only to a loss in gasses but also to different phenomena related to this: for example, re-oxidation of the anode with possible mechanical failure and/or formation of localized hot spots due to the direct reaction between the oxidizing gas and the fuel which may lead to a strong increase in the temperatures and likely to corrosion or degradation of the surrounding materials.

In *figure 15* it is possible to see the typical location where a sealant can be placed in a planar stack. So, the sealant typically has to be interfaced with different materials both metallic (in the case of endplates, interconnects or frames) and ceramic (i.e., elements of the cell, typically the electrolyte or the anode).

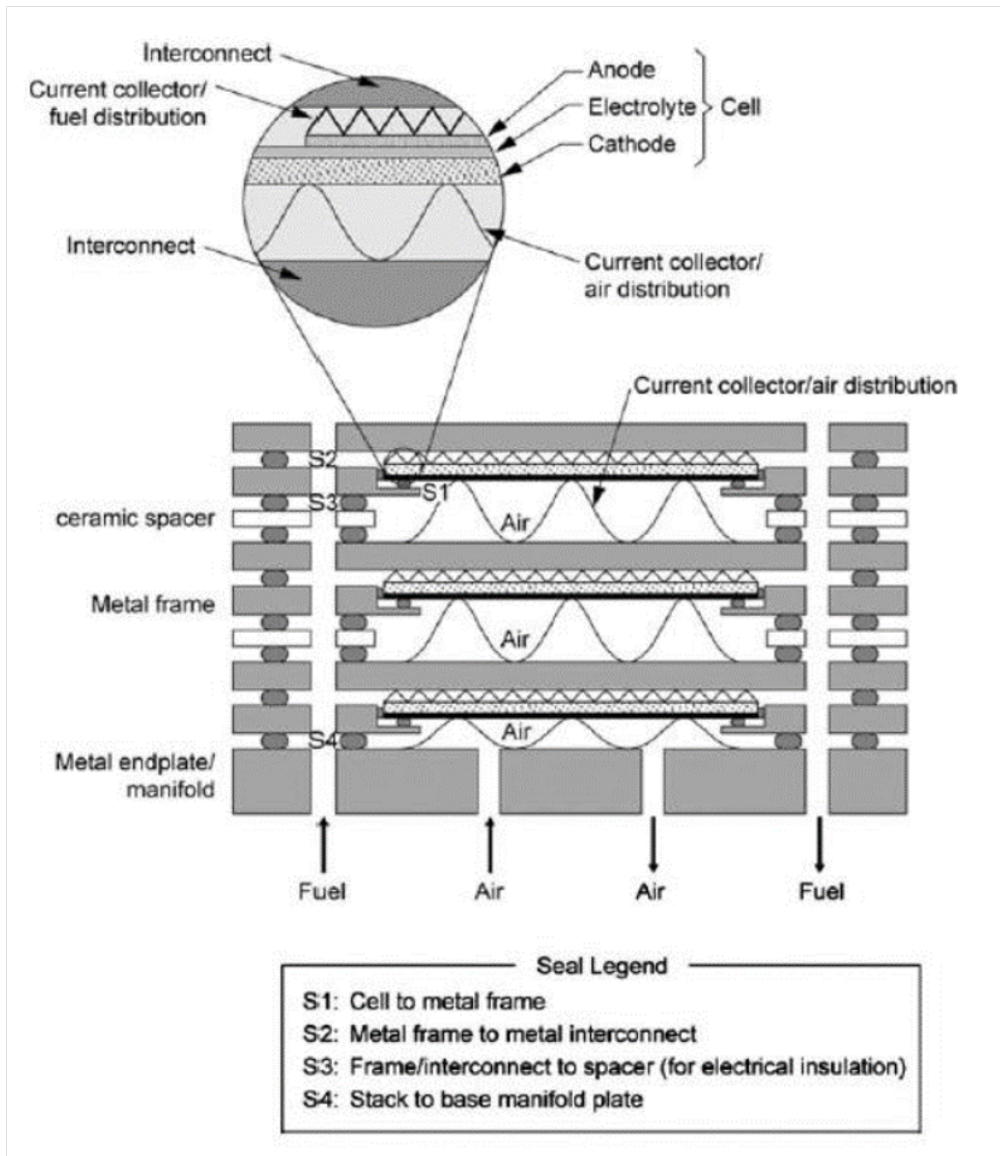


Figure 15: Common sealing design for the planar stack [30].

Due to its role and the harsh operating environments, the main characteristics that a sealant should have are [30-31]:

- Good CTE compatibility with other interfaced materials (typically in the range of $10-12 \times 10^{-6} \text{ K}^{-1}$)
- Resistance to thermal shock
- Resistance and stability at high working temperatures (600-800°C)
- Electrical resistivity $>10^4 \Omega \text{ cm}$ at working temperatures
- High gas tightness in the operating conditions
- Affordable

. Generally, there are different kinds of sealant, which can be classified in two main categories:

- 1) **Compressive sealants:** These sealants need the application of an external compressive load during the operations in order to reach the required gas tightness. These materials do not form a rigid bond with the joined parts, so the requirements on the CTE mismatch are less tight, furthermore the thermal stresses can be accommodated by plastic deformation of the sealant itself or by its sliding respect to the joined counterparts. However, despite these positive aspects, the needs of the application of a consistent load in the relevant operating conditions of a SOC stack leads to complications in the design of the system in addition to possible mechanical failures of other components in the stack. Some examples are: Mica sealant, ceramic fibres and metallic compressive sealants.
- 2) **Rigid sealants:** in contrast to the compressive ones, in this case these sealants bond with the joined materials, forming a hermetic sealing. Their application is easier than compressive sealants and do not require a compressive load during stack operation. However, the formation of a bonding with the sealed surfaces requires in general a specific thermal treatment and, especially, a good thermo-mechanical and chemical compatibility between the sealant and its counterparts. The most common rigid sealants are glasses and glass-ceramic based or metallic brazes. A more detailed section on glass-ceramic sealants is dedicated in the following part.

2.2.6.1 Glass-ceramic sealants

Nowadays glass-ceramics are the principal types of sealants used in SOC applications. Among their main advantages, there is the possibility to change their properties changing the composition of the starting glasses. Indeed, the introduction of different oxides in the glass can have an effect on the CTE of the material, on glass transition temperature (T_g), on the sintering and on the chemical resistance in the SOC operating conditions. Furthermore, not only the composition of the parent glass should be taken into account but also the amount and the nature of the crystalline phases that can be formed during the joining thermal treatment or the prolonged exposure at high temperatures. Glass-ceramic sealants are typically applied in form of powders and then a thermal treatment is performed in order to lead to the sinter-crystallization of the sealants and especially to the bonding with the components to be sealed. Figure 16 represents an example of an excellent compatibility and sintering behavior of a glass-ceramic sealant (labelled SACN in the picture). In this case the sealant was used to join Crofer22APU with YSZ so it represents a typical example of the joining/sealing between the interconnect and the electrolyte.

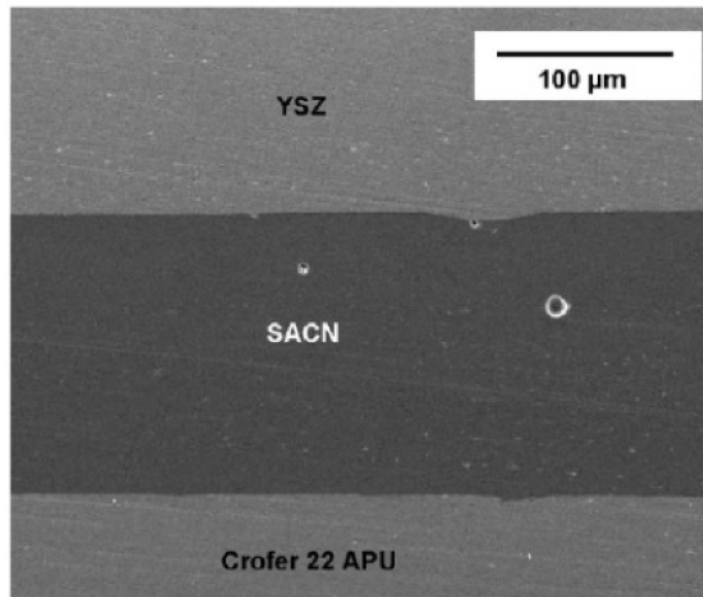


Figure 16: Example of excellent junction [32].

A part of the stability and properties of the glass-ceramic itself, the interfaces between this material and the joined components are very important. In particular, many attentions have been dedicated to the interface with Cr-containing metallic interconnect, since many detrimental reactions have been investigated in this region. This is due to the high reactivity between the typical elements present in the glass composition and Cr, due to the operating conditions. For example, some alkali-containing glasses showed degradation due to the formation of volatile Na_2CrO_4 or K_2CrO_4 . The formation of these species compromises the integrity of the sealant and to the loss of its tightness on one side and to corrosion phenomena in the metals on the other.

Many glass-ceramic compositions investigated in the last decades and some commercial ones are Ba-based and alkali-free. Up to now these represent the most promising solution in terms of glass-ceramic sealants.

3. Experimental

This chapter will present the experiments conducted to study two different glass sealants, which have been characterized from the powders to their final application within a SOFC single repeating unit (SRU). First of all, the different materials involved in this study will be presented. The deposition of one glass by robocasting will be then explained, followed by the characterization of both studied glasses. Finally, the mounting process and electrochemical characterization of the SRU will be detailed.

3.1 SRU elements and materials

As seen in the introduction of this work, glass sealant is a key component of SOFC stack to ensure the gas tightness of each electrode chamber. In this sense, this material aims to be placed between different elements as presented in *figure 17*. Here in particular, the sealant is placed between the endplate and the IC, both made of steel and also between the cell and the IC. Each of those elements will be presented hereafter.

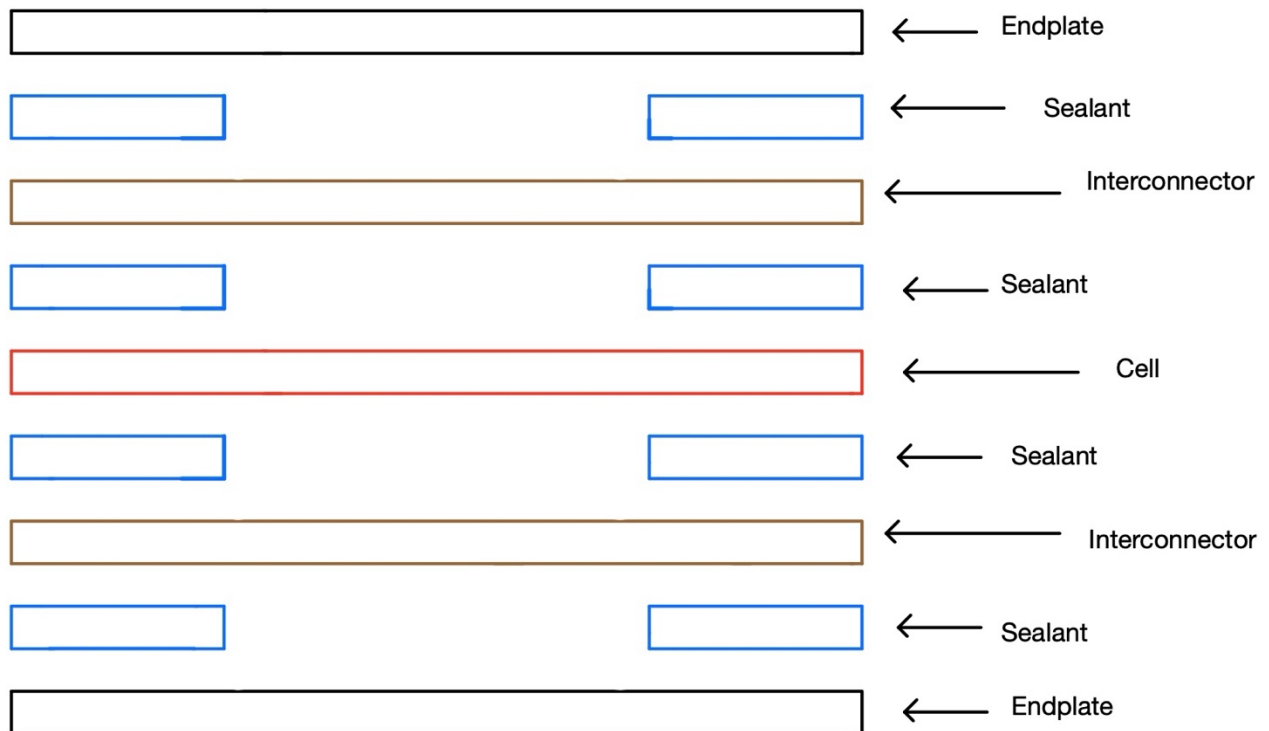


Figure 17: schematic representation of a single repeating unit placed between two endplates.

3.1.1 Sealants

Two different types of sealants have been used in this work:

1. **Glass Sealant G018-311 (Schott, Germany)**: received in the form of sheets produced by tape casting. Its chemical composition is detailed in Table 2 and its properties are listed below. Moreover, the required heat treatment for the glass formation is indicated on Table 3. This glass will be named in the rest of the document as Sealant 1.



Figure 18: Glass sealant by SCHOTT

Table 2: Chemical composition of Sealant 1

Chemical composition	
Al ₂ O ₃	1-10 WT.-%
B ₂ O ₃	1-10 WT.-%
BaO	>50 WT.-%
MgO	1-10 WT.-%
SiO ₂	10-50 WT.-%

- Thermal expansion coefficient: $9.9 \cdot 10^{-6} \text{ K}^{-1}$
- Transition Temperature: 620 °C
- Density: 3,57 g/cm³
- Thickness: 255 µm

Table 3: Heat treatment of glass sealant G018-311

HEAT TREATMENT	Ramp [C°/min]	Temperature [C°]	Time [min]
Initial temperature	/	25	/
1. Heating up	1	850	/
2. Holding time	/	850	30
3. Cooling down	1	810	/
4. Holding time	/	810	90
5. Cooling down	1	25	/

2. **Glass sealant G018-392 (Schott, Germany):** received in the form of a powder in order to be deposited by Robocasting. Chemical composition and properties are listed in Table 4 and below. The thermal treatment presented in Table 5 is slightly different from the one of sealant 1, skipping the step at 810°C. This glass will be named as Sealant 2.

Table 4: Chemical composition of Sealant 2.



Figure 19: Glass sealant by SCHOTT.

Chemical composition	
Al ₂ O ₃	1-10 WT.-%
B ₂ O ₃	1-10 WT.-%
BaO	>50 WT.-%
MgO	1-10 WT.-%
SiO ₂	10-50 WT.-%
CaO	1-10 WT.-%
ZnO	1-10 WT.-%

- Thermal expansion coefficient: $10.6 \cdot 10^{-6} \text{ K}^{-1}$
- Transition Temperature: 590 °C
- Density: 4,0025 g/cm³

Table 5: Heat treatment of glass sealant G019-392.

HEAT TREATMENT	Ramp [C°/min]	Temperature [C°]	Time [min]
Initial temperature	/	25	/
1. Heating up	1	850	/
2. Holding time	/	850	30
3. Cooling down	1	25	/

All the data of sealants have been provided directly by SCHOTT. Both are silica-based glasses, in which the main network former is SiO₂, together with B₂O₃ and Al₂O₃ (intermediate oxide). Glass network formers are the basic constituent of the network, since they allow the connection of the polyhedral units. In both cases BaO is predominant as network modifier. Network modifiers are able to modify different properties, such as T_g, T_s, CTE, maintain charge neutral and create non-bridging oxygen atoms [31]. The use of BaO is very common in glass-based sealants for SOC applications. The same role is for MgO in both the compositions. It is possible to identified two relevant differences in these glass compositions: the presence of CaO and ZnO in the sealant 2. CaO act as network modifier as-well, while ZnO is typically considered as an additive. It helps to tune different parameters in terms of viscosity, flowability, CTE and, above all, the adhesion between other components.

3.1.2 Solid oxide cell

The SOFC cells used in this work are shown in *figure 20* and was provided by SOFCMAN (China). This cell has an anode-supported configuration, because the main support of all materials is the anode, by being thicker than the electrolyte and the cathode. The composition and thickness of each layer is provided in *table 6*.

Table 6: Technical data of SOFCMAN cell [33].

Product Type	Anode-Supported Cell
Cathode/Thickness	LSCF+GDC/20~25 μ m
Diffusion Barrier Layer/Thickness	GDC/2~3 μ m
Electrolyte/Thickness	YSZ/10~15 μ m
Anode/Thickness	NiO+YSZ/400 μ m
Bending Strength	≥ 250 MPa
Power Density	≥ 0.7 W/cm ² (750°C, 0.7V)
Size	Button to 7cm \times 7cm

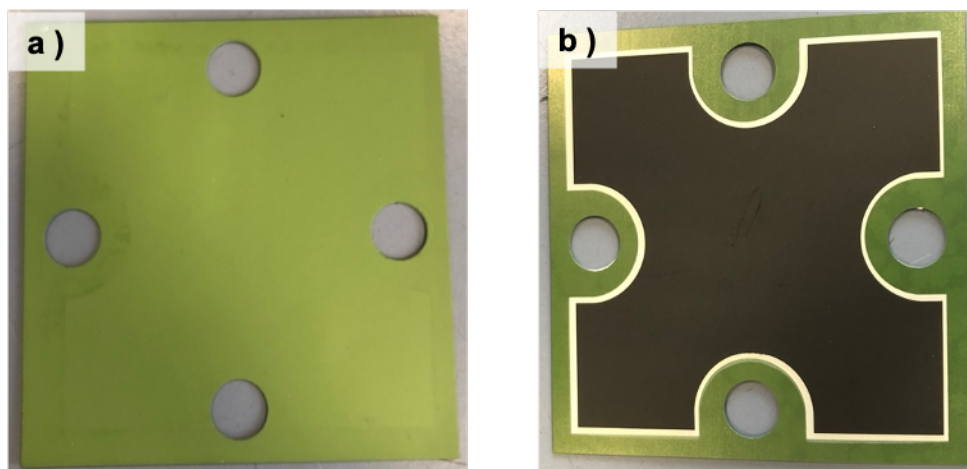


Figure 20: (a) Anode side and (b) Cathode side, where the black layer corresponds to the cathode, the white layer to the diffusion barrier layer and the shiny transparent layer on top of the anode corresponds to the electrolyte.

3.1.3 Interconnector

The interconnectors used for this thesis are provided by AMES (Spain). They are made by powder metallurgy and composed of steel SUS445, which is a Cr-rich stainless steel. Their composition is presented in Table 7:

Table 7: Typical chemical composition of IC.

INTERCONNECTOR							
	C	Cr	Fe	S	Mn	Si	P
VALUE %	0,004	22,6	Bal	0,010	0,65	0,01	0,005

As presented in the chapter 2.1.3, IC must be coated for an efficient use in SOFC. Here, IC have been directly coated by AMES, using a solution of ethanol and MC12 powder to form a $(\text{Mn,Co})_3\text{O}_4$ spinel protective coating layer. Figure 21 shows a picture of one coated IC.



Figure 21: Metal interconnector made by AMES.

3.1.4 Endplate

The steel used for the end plates is **CROFER22APU** [34], which is one of the most common steel for SOFC application, especially for IC, thanks to excellent performance at high temperatures. Its chemical composition is presented in Table 8.

Table 8: Chemical composition (%) according to ASTM A 240 [34]

CROFER 22 APU											
	%C	%Cr	%Fe	%S	%Mn	%Si	%Ti	%Cu	%P	%Al	%La
MIN		20,0	Bal		0,30		0,03				0,04
MAX	0,03	25,0		0,020	0,80	0,50	0,20	0,50	0,050	0,50	0,2



Figure 22 Crofer 22 APU already covered by the coating:

3.2 Glass Deposition by Robocasting

General principles and “Machine Explanation”



Figure 23: Overview of Nordson EFD robocasting.

Robocasting allows to deposit pastes with high x,y,z accuracy using an extrusion technique. This technique allows to minimize process material losses, furthermore it is highly flexible, allowing the deposition of potentially every material following the desired geometry. In this work, a robocasting machine by Nordson EFD was used to deposit the powder sealant (sealant 2) on IC, endplates and cells.

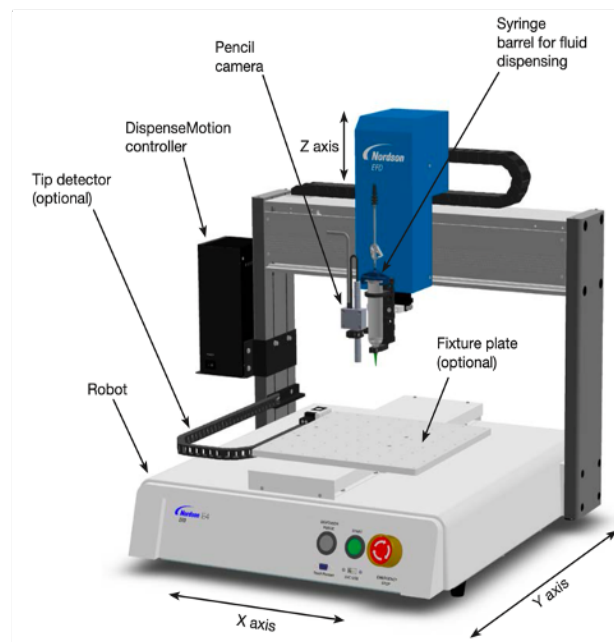


Figure 24: Components of Robocasting [35]

The photo of the robocasting used in this work, together with a schematization of its components are reported respectively in figure 23 and 24. As is shown in the figure 23, there are different components which help the correct working of the machine. Principally, the process is managed by a robot. The paste to be deposited is placed inside a syringe barrel, and extruded out of a nozzle through the application of a pressure on the piston. In this work, the deposition was performed under the application of a pressure of 2atm. A detailed picture of the extrusion head is reported in figure 25.

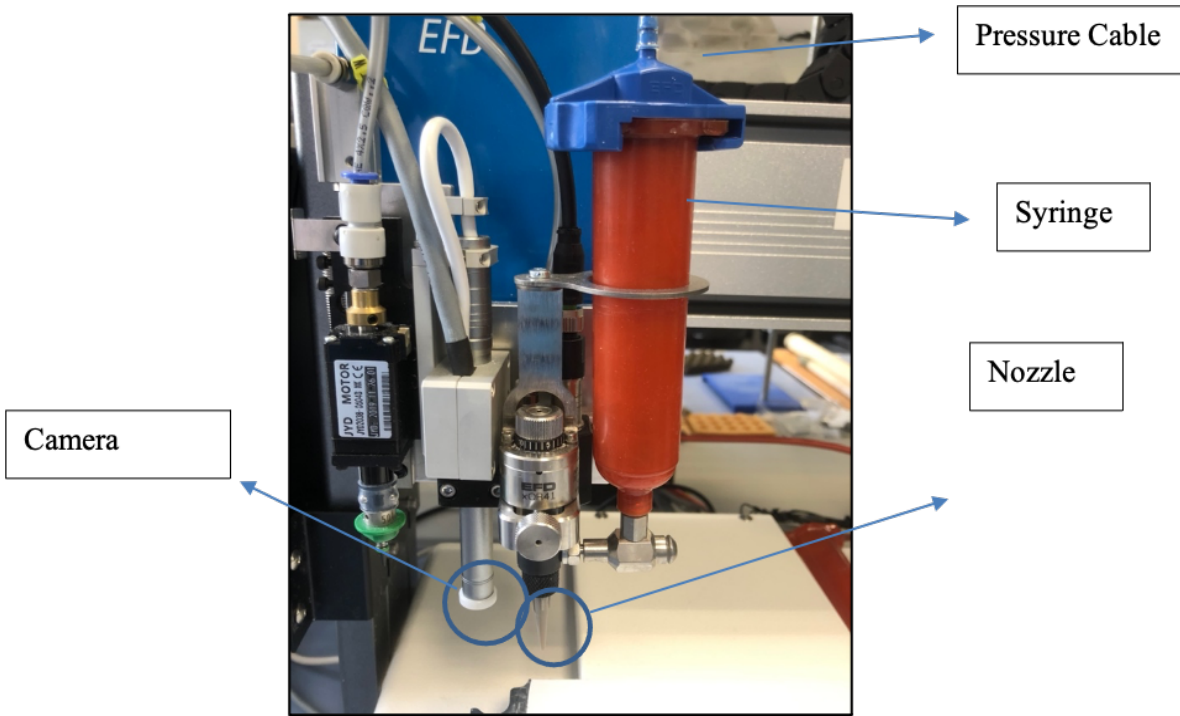


Figure 25: Some components of the robocasting

The syringe barrel can move on the X and Z axis, while the plate (figure below) on Y axis. The deposition path is literally written directly by “Dispense motion” program, recommended by the company itself. Through the software it is also possible to modify different deposition parameter in order to optimize the process to obtain the desired result.

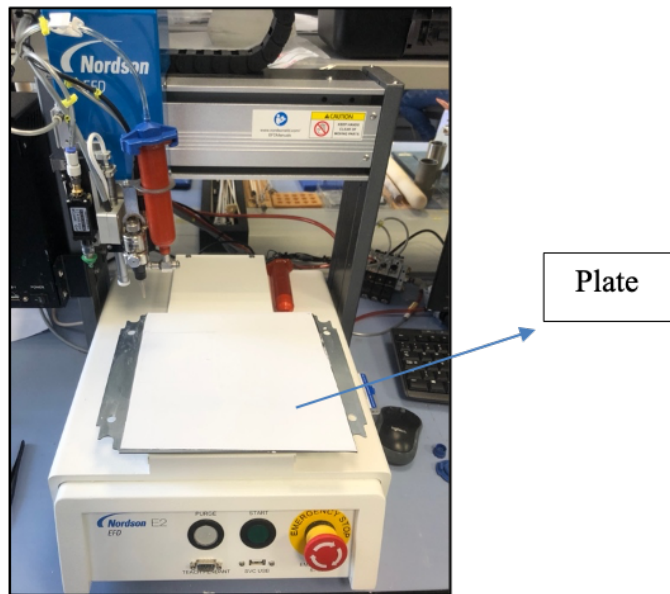


Figure 26: work surface of Robocasting.

The paste recipe used in the present thesis was:

80 wt.% sealant 2 powder + 20 wt.% terpineol

After the weighting of the material and a first manual mixing, the paste was subjected, to a mixing process for 15 minutes at 1500 rpm, followed by defoaming process for 15 minutes at 1500 rpm. Finally, the paste was placed inside the syringe, which was mounted in the robocasting support.

After the preparation of the paste, the deposition parameters were optimized through a “try and error approach” in order to obtain a deposition of the desired thickness and width. The parameters considered were the following ones:

- **Line speed:** This is the speed with which the syringe (or the plate in the case of Y axis) moves following its path.
- **Pre moved delay:** it corresponds to the time in which the syringe “waits” in the starting point before starting moving. It has to be regulated in order to correspond to the time that the paste needs to flow from the nozzle to the plate at the beginning of de deposition.
- **Shut off distance:** it is the distance before the end of the path where the valve is closed and the extrusion stops.
- **Nozzle diameter:** it is Inner diameter of the nozzle and it corresponds to the width of a deposited line (if the paste does not flow laterally after the deposition).
- **Pressure:** it is the pressure of the pressurized air used to push the piston and extrude the paste. In fact, it manages the amount of material to be used for the deposition. Pressure and amount of material extruded per second are proportional.
- **Distance between nozzle and plane:** This value is set before each deposition. It is related to the nozzle diameter since in general has to be one half of this value. The distance between the nozzle and the plate gives the thickness of the deposited layer. The distance, which has been used for this project was 500 microns. The figure below helps to describe better the important role of this parameter.

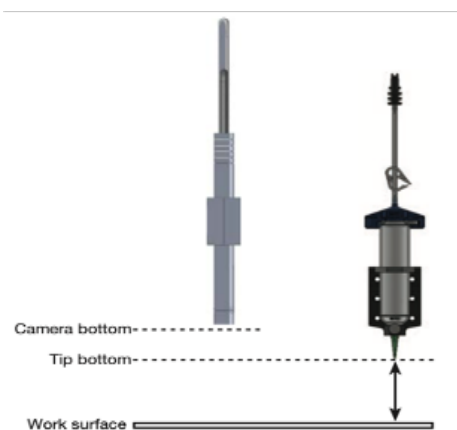


Figure 27: working distance [35]

Different try and error attempts were performed in order to optimize the thickness and width of the deposited lines, their uniformity and the excess of paste at the beginning and at the end of the path. Some of these attempts are reported in figure 28. The optimization led to the selection of the parameters that were used in all the following deposition of the sealant 2. These values are reported in Table 9.

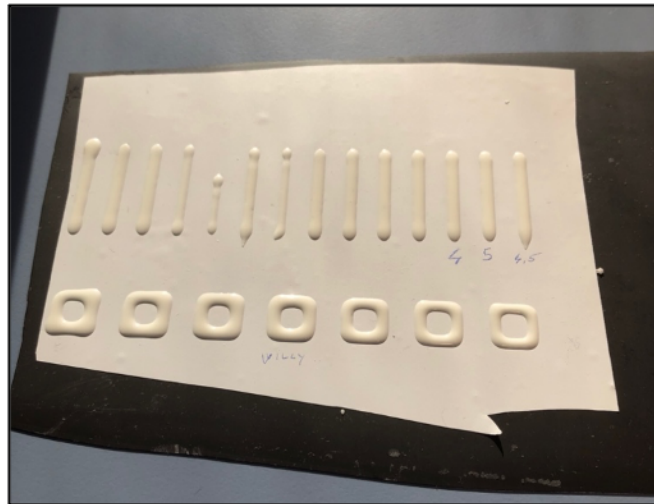


Figure 28: Some depositions tests, where parameters has been changed.

Table 9: Parameters used for robocasting

Parameters					
Line speed [mm/s]	Pre moved delay[s]	Shut off distance[mm]	Nozzle diameter [mm]	Pressure [bar]	Distance between nozzle and plane [μm]
7,5	1	4	1,19	2	500

3.3 Materials Characterization

In this paragraph the techniques and the approach used to characterize the material, before the single cells and SRU tests, are described.

3.3.1 Base Materials characterization

Sealants:

As anticipated, two glass sealants were used. They were characterized under a chemical and compositional point of view in addition to the investigation of their characteristic temperatures. Furthermore, their compatibility with the interfaced components was studied (see section 3.3.2 “compatibility tests”).

X-Ray diffraction (XRD) analysis

This technique allows to define the crystalline phases present in any material. In this case, XRD analyses (D8 Avance Bruker, Germany) were carried out on the both sealants obtained after the joining process described in 3.1.1. Indeed, after the sinter-crystallization treatment the parent glass partially crystallize forming a glass-ceramic. XRD was performed in order to detect the nature of the crystalline phases formed in the material. The samples, which are presented in the *figure 29*, have been milled manually in an agate mortar, reducing them in form of powders, which were analyzed. The XRD pattern was collected in a 2θ range $20-80^\circ$ using Cu $K\alpha$ as incident radiation. Crystalline phases were identified through the use of the software “xpert highscore”



Figure 29: sealant 1 after sealing treatment (on the left) sealant 2 after sealant treatment (on the right).

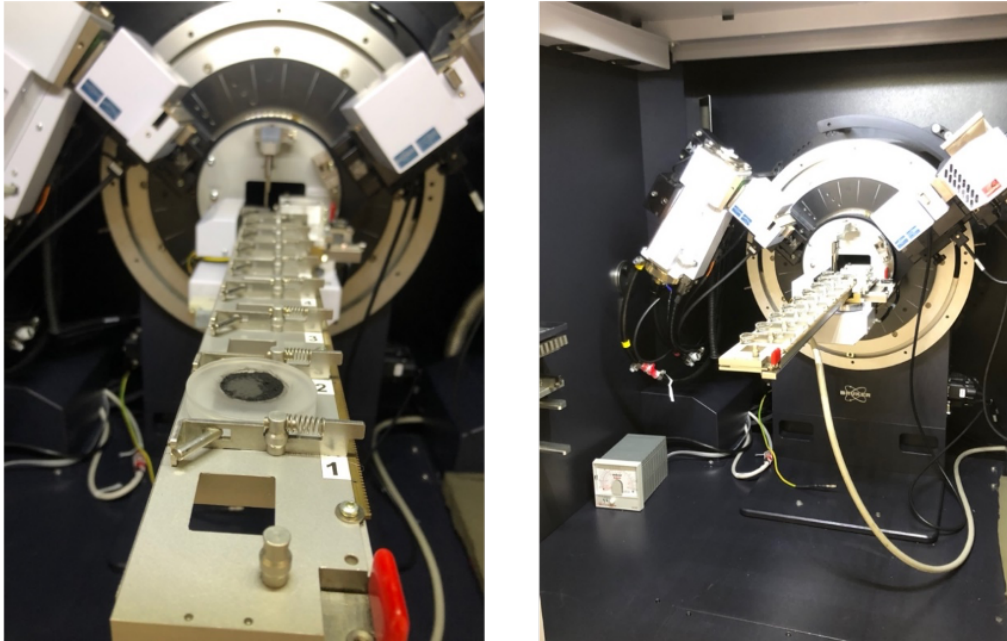


Figure 30: XRD machine used for analysis.

Differential Thermal Analysis (DTA)

This technique is relevant to focus on the endotherm and exotherm transformations. In the case of glasses and glass-ceramics DTA allow the detection of characteristic temperature associated with the release or abortion of heat during a heating ramp, such as: glass transition temperature (T_g), crystallization temperature (T_c), “melting” (T_m). The DTA analyses (Netzsch DTA 404 PC) were carried out by using Al_2O_3 powders (Alfa Aesar, 99,99% purity) as the reference. The same amount (about 100 mg) of sample and reference was used in Pt crucibles. The analyses were conducted from room temperature to 1300 °C using a heating rate of 20°C/min.

3.3.2 Compatibility tests

As anticipated, the main goal of the present work was to implement the use of glass-based sealants in SRU tests at IREC. In order to understand the compatibility of these materials with the other involved in the set-up of a SRU, a first step involved the preparation of small samples in order to investigate the interfaces between the glass-ceramics and the joined components.

In general, for each sealant the considered aspects were:

- To evaluate the thickness reduction of the joining under the application of a load. Indeed, the test design requires a thickness of the sealant below 100 microns. In order to not affect the electrical contact between different components, guaranteed by the use of conductive meshed of 100 μ m.

- Evaluate the adhesion between different materials together with the integrity of the joining itself low level or absence of porosities, cracks and delamination.

In order to investigate all these aspects before the single cells and SRU tests, small samples were prepared, in order to study the compatibility of the different materials and adjust the subsequent tests on the basis of the information collected here. In figure 31 it is reported a picture and the dimension of steel coupons used to produce these small samples. Due to the different materials involved (two sealants, two metallic materials, the presence of the coating) a working plan was done. In table 10, a schematization of all the samples prepared for this preliminary investigation is reported. These samples were sandwich samples metal/sealant/coated metal. In this way in every sample, it was possible to investigate the interfaces with both the bare steels and the coated ones.

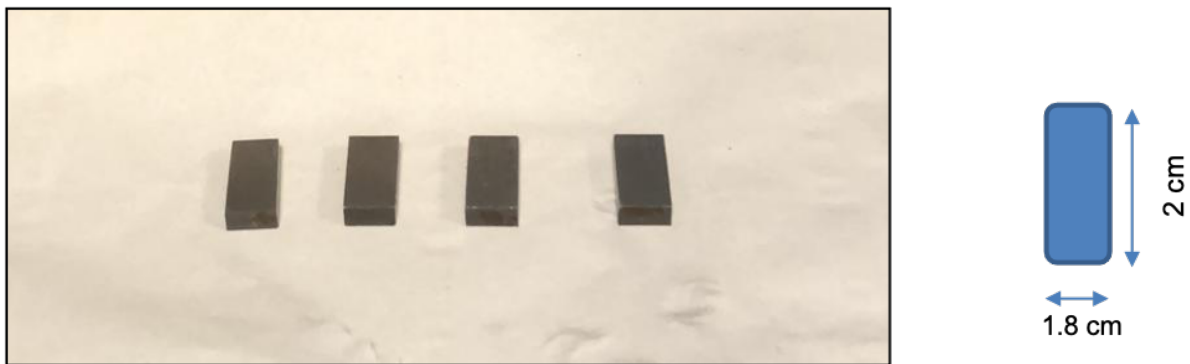
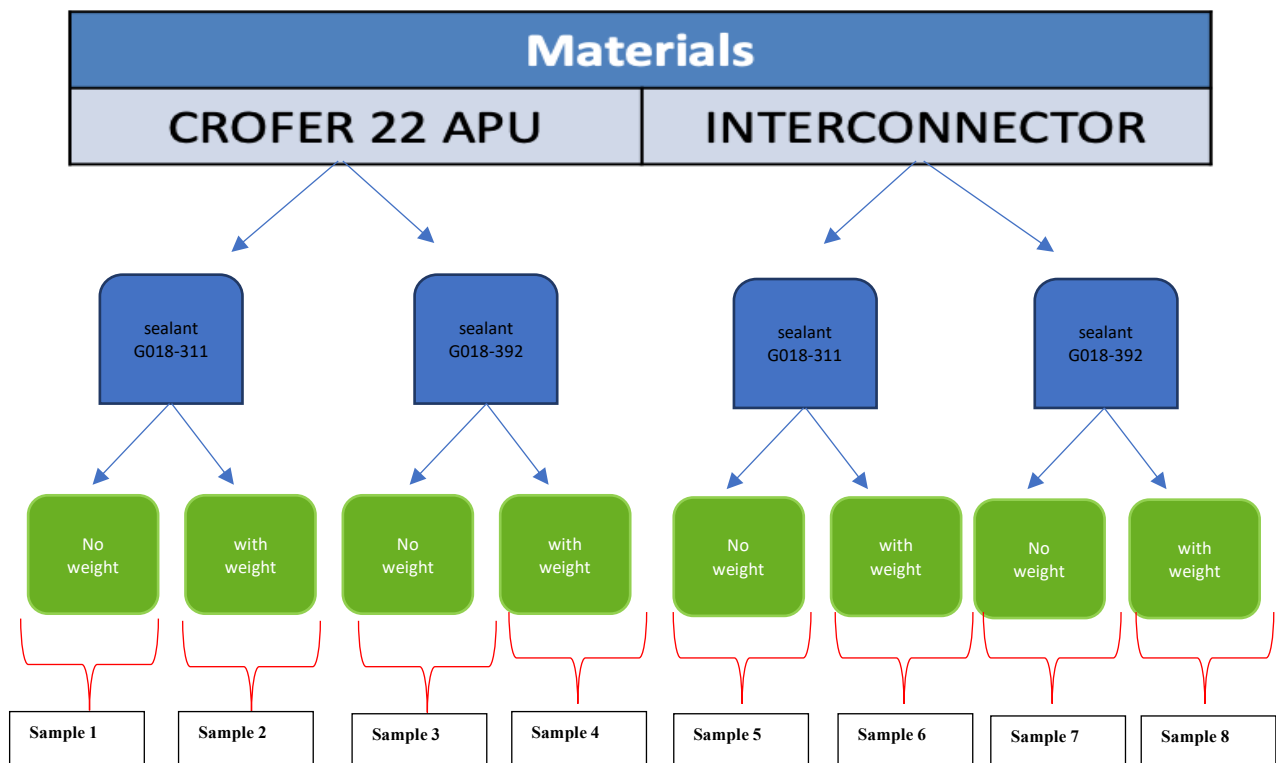


Figure 31: size of small samples.

Table 10: Working plan.



The coating preparation on small metallic coupons for this compatibility study was performed by manual painting (using a brush) the MC12 on the substrates. A first step consisted in the ink development, MC12 (MnCo_2O_4) powders were mixed with Terpeneol, used as solvent, illustrated in the *fig 33, picture 1*. The suspension used follows this formulation:

INK: 33 % weight MC12 + 67% weight Terpeneol

Consequently, the formulation used was:

MC12 = 4,93 g and Terpeneol = 10,01 g

The suspension was mixed firstly, under stirring with 100 rpm for 60 seconds on the hot plate, then, with ultrasounds for 5 minutes, as is possible to see in the *fig.33, picture 2*. The next step was polished process of the coupons, as shown in the *figure 32*, followed by a suspension deposition directly on the steel polished, by a manually painting. Thus, two coating layers were applied, as it is possible to see in the image below, by paintbrush (*fig. 33, picture 3*). In addition, between the first and the second deposition, the sample was placed on the heating plate at 50 °C, to speed up the dry up process, that lasted 5 minutes to complete the first layer deposition.

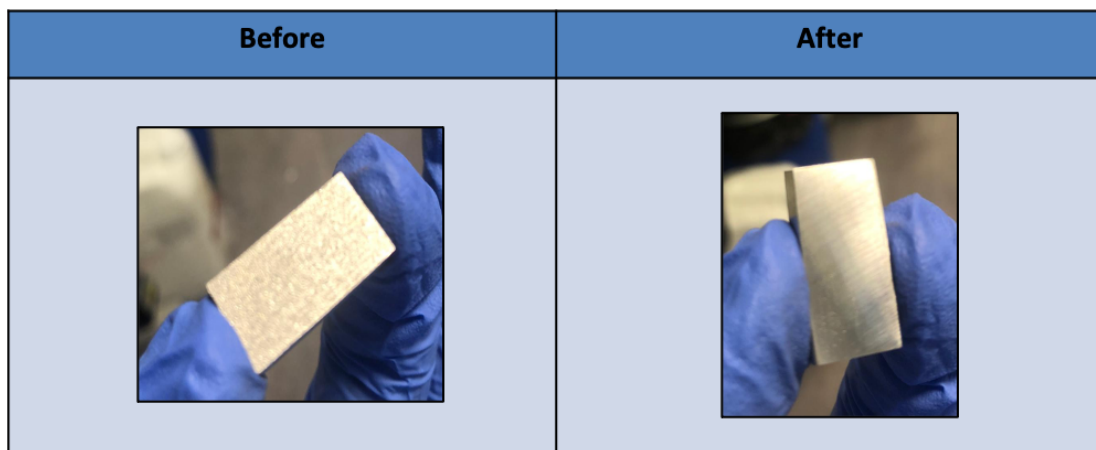


Figure 32: Bare sample before and after polished process

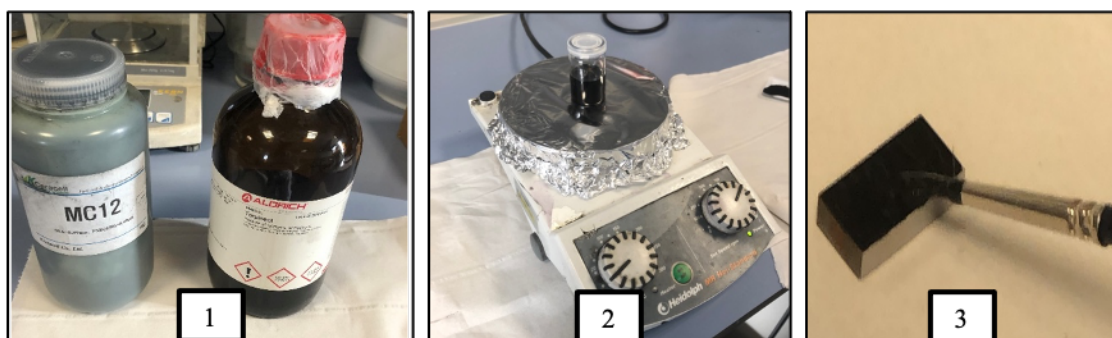


Figure 33: MC12 powder + terpeneol solvent (1), Suspension under stirring process (2), Coating Deposition by painting brush (33).

Since in the SRU tests the sealant would have been interfaced with the reduced coatings, the coatings produced on these small samples were reduced as well, in order to reproduce the surface chemistry and reactivity of the interface in the real operating conditions. So, the sample already painted has been treated in reduced atmosphere with the parameters reported in table 11.

Table 11: Reduction treatment for compatibility test samples

Reactive Sintering			
Temperature (C°)	Rampe rate (C/min)	Time (h)	Gas
900	5	2	5% H ₂ + Argon

Despite the manual deposition method, the reduced coating on small samples resulted to be homogeneous and free of cracks as shown in figure 34.

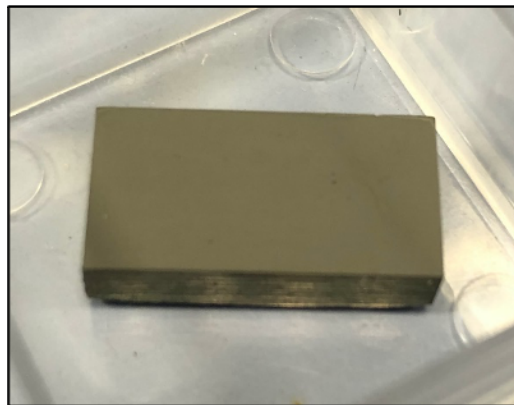


Figure 34: Sample after coating sintering.

Moreover, as already described in the previous paragraph, each sample was prepared in two different configurations: one with a weight added and another one without any weight added, as shown in the figure 35. The reason of it has been to predict and to simulate the real condition of the SRU, where a certain load is always applied. In this case, the weight that was used for these samples was 0,059 kg.

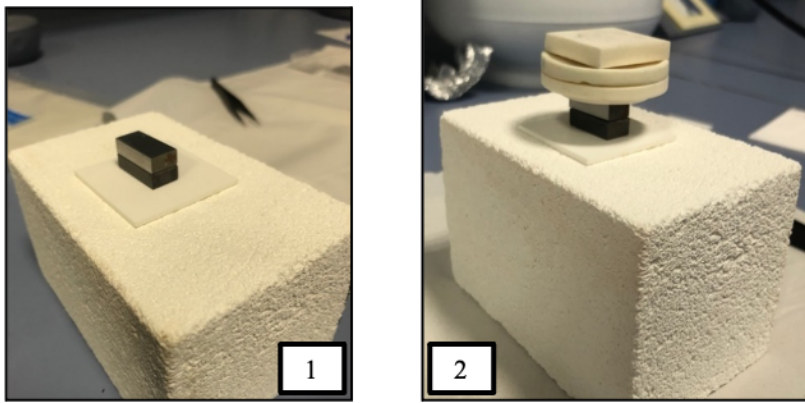


Figure 35: Example of sample without weight (1), Example of sample with a weight (2)

Sealant 1 was provided in form of “sheets”; thus, pieces of suitable dimensions were cut directly with a scissor. After this, it was placed between two steel coupons. The next step was the heat treatment of the sealant, already shown in the *table 3*.

On the other hand, **Sealant 2** was deposited as already explained in 3.2 chapter by robocasting. The sealant was deposited on one coupon as shown in *figure 36, picture (2)*, and left to consolidate (solvent evaporation) in air before to apply the second steel coupon on it forming a sandwich.

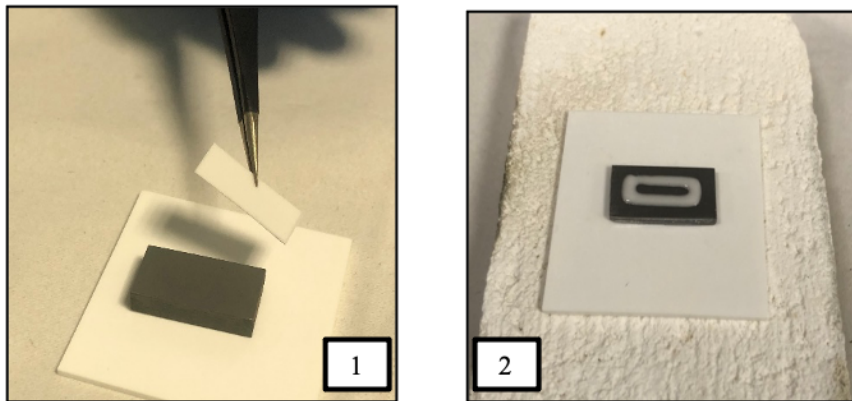


Figure 36: Deposition of sealant 1 “sheet” (1), Example of robocasting deposition of sealant 2(2).

After the sealing treatment of each sealant, all samples were prepared for a Secondary Electron Microscopy (SEM) and X-ray electron dispersion spectroscopy (EDS), by metallographic preparation. Each sample was embedded in an epoxy resin, as in the *figure 37* below. The recipe used was: 21 g of resin and 2,77 g of hardener.

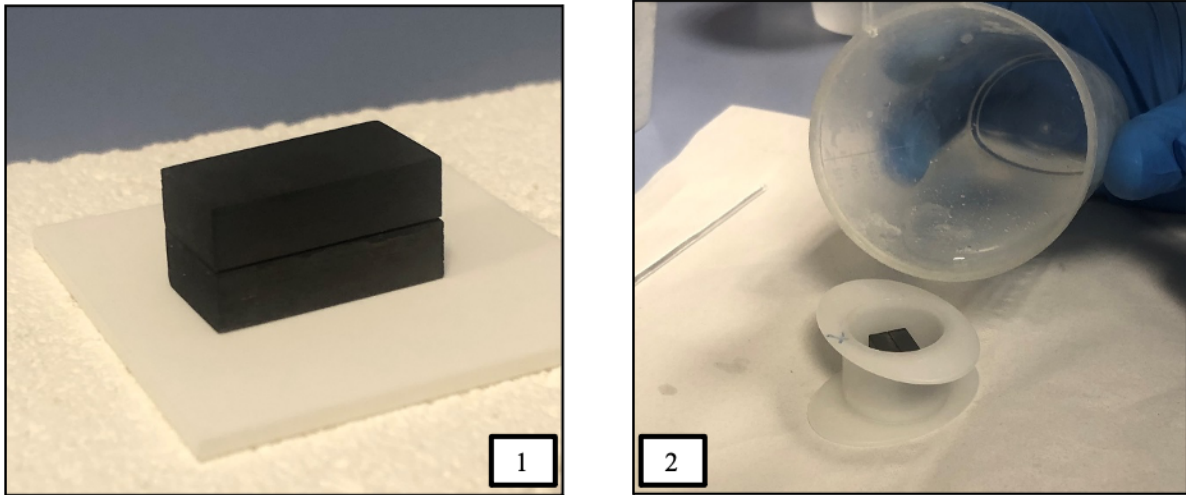


Figure 37:(1) a sample after the sealing treatment (2) Incorporating a sample in a resin.

After the resin consolidation, all samples were polished through the polishing machine (TECNIMETAL) (Figure 38), using SiC fine grit sand papers (320-500-800-1200-2400-4000). After that, in order to obtain a smoother and less rough surface, the polishing process was finished using, firstly a diamond paste of 3 μm , secondly a diamond paste of 1 μm (MetaDi, monocrystal diamond suspension). After the polishing, the samples were subjected to sputtering deposition, which provided a gold layer deposition during 30 seconds and 80 mA of current.

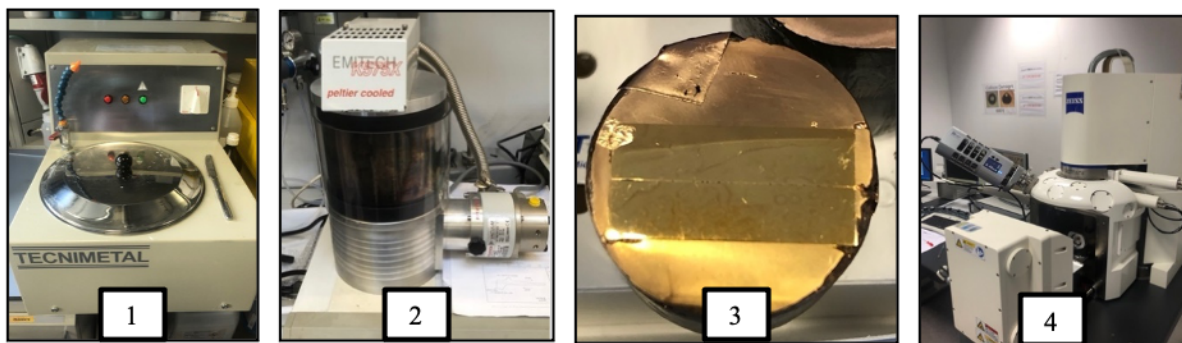


Figure 38: Polishing machine (1) Sputtering Machine (2), Sample after gold deposition (3) Secondary Electron Microscope (SEM) (4).

In addition to the previous samples, two additional ones were prepared in order to investigate the compatibility of the sealants with the cell after the joining thermal treatment. For doing this a piece of cell was placed in the middle of the joining forming a sandwich sample: Crofer22APU/sealant/cell/sealant/Crofer22APU. This was done for each sealant. In this way it was possible to study the interfacing of each sealant with both the anode on one side and the electrolyte on the other one.

Resistivity Test

Another important characteristic of a sealant is its electrical resistivity; indeed, a good sealant should be an insulator at relevant operating conditions. To test this aspect both the sealants were joined with Crofer 22 APU. After the joining thermal treatment 4 Ni-Cr wires were welded on the steel coupons (two for each coupon). The resistivity measurement was performed in a probostat station (figure 39).

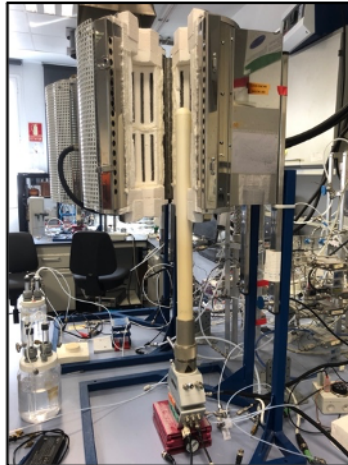


Figure 39: Probostat station.

The sample was always maintained under constant voltage of 1,3 V during all the test and the current was measured. The test was performed in static air at 800°C. Measuring the current for all the duration of the test it was possible to calculate the resistance thanks to the Ohm law:

$$U = R * I \quad (3.1)$$

U = Voltage [V]
R = Resistance [Ω]
I = Current [A]

Knowing the eq. (3.3), is possible to achieve the resistivity ρ , which is defined as (3.4):

$$R = \rho * \frac{l}{A} \quad (3.3)$$

l = lenght of specimen [m]
A = cross section area [m²]

$$\rho = R * \frac{A}{l} \quad (3.4)$$

The current was monitored for 240 h, in order to verify its stability during a long period and the possible development of electrochemical reactions.

3.3.5 MC12 characterization

XRD analysis

In order to obtain information about powders, XRD was performed on the as-received material. Furthermore, XRD were carried out on reduced powder, which was subjected to the reducing treatment by AMES at 1120°C in Air/H₂ (5vol% of H₂).

Dynamic Light scattering (DLS)

Dynamic light scattering is a non-invasive technique, which allows to obtain a granulometry distribution of particles and the average particle sizes. The powders are dispersed in a suspension to be studied. In this work light scattering was performed on MC12 suspension, which was used in the airbrush (described in the 3.4.1 chapter).



Figure 40: DLS used for MC12 analysis.

3.4 Single cells and SRU characterization

Once the glasses characterized and especially their compatibility with the rest of the materials, the next step has been to characterize them in real conditions: through electrochemical tests of single cell and SRU. A first common step consisted in preparing the endplate by coating the one that would be in contact with air. This work is detailed in the next paragraph.

3.4.1 Endplate preparation

To avoid the oxidation of the endplate that would be in contact the air and to reduce the Cr evaporation occurring in this case, it has been coated with MC12 by using an airbrush (*figure 41*). It allows a homogeneous deposition on a large surface, by spraying a material suspension. This airbrush can be controlled by a 3D printing frame (Printing3DSolutions).

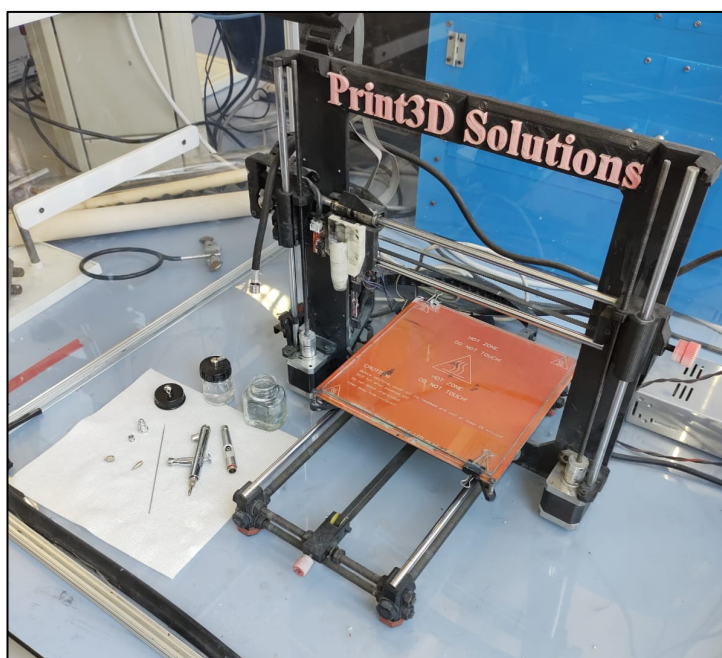


Figure 41: Airbrush machine.

Before the deposition process, two steps were carried out:

- 1) Writing G-code program

The sprayer pathway has been defined following a code-program, which has been created converting a cad program into a G-code file. The draw cad has been written by FreeCad, while Prusaslicer and Cura have been used to convert the cad files into G-code files.

2) Ink preparation

After this, a suspension of coating has been prepared, using a material conductive powder with a certain amount of solvent. In this case, the final recipe has been as following:

$$\text{MC12} = 2 \text{ g} \quad \text{and} \quad \text{ethanol} = 20 \text{ g}$$

Subsequently, to get better densification and to avoid agglomeration phenomena, the suspension has been subjected to ultrasounds for 30 minutes. Once the ink has been prepared, it has been put inside an adapted baker for the airbrush.

Despite the fact of having an automatic displacement of the aerograph, the deposition has been carried out by controlling manually the valve regulating the speed and the amount of the suspension flow as seen in the *figure 42(1)*. The deposition result has been satisfactory in terms of uniformity and consistency of the suspension. Then the coating sintering has been carried out.

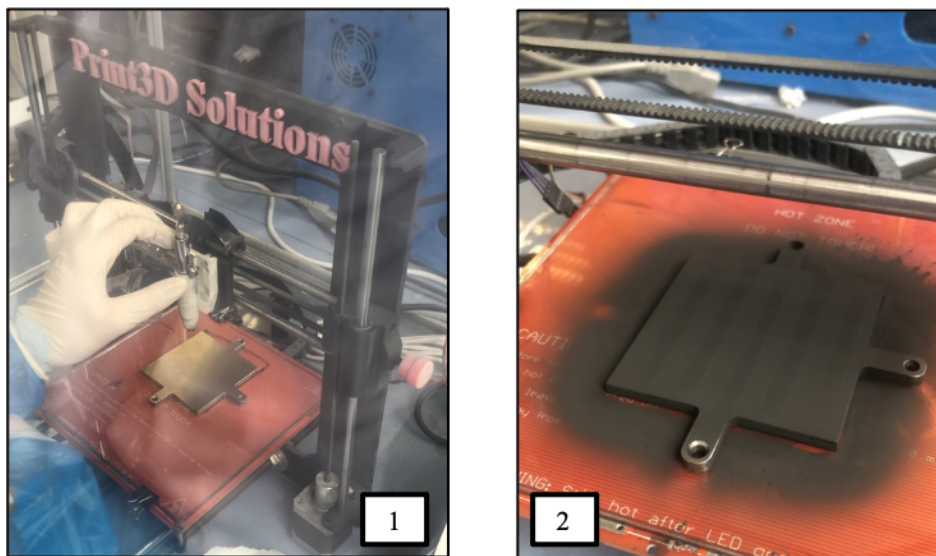


Figure 42: Coating Deposition (1), Final result of deposition (2):

3.4.2 Single Cell Assembly

Characterization of a single cell has been first elected in order to simplify the system, avoiding the use of IC and reducing the number of sealants. The assembly procedure of this configuration is detailed hereafter (see Figure 43). First of all, the coated endplate had been placed as the lower endplate, aiming to be in contact with the oxygen electrode of the cell. A layer of sealant 1 was then placed on top of the endplate to delimitate the edge of the oxygen electrode as well as the holes where the H₂ would flow. A silver mesh was added on top the endplate in order to collect the current from the cell. After this, a cell, which has been already painted with LSC paste to improve the current collection, was placed having the cathode facing down. The anode was then painted with a Ni paste and covered with a Ni mesh and another piece of sealant 1. Finally, the top bare endplate has been put on the top of all.

Generally, an insulating material has been located between the higher endplate and the compressive plate, which is explained in the 3.4.3 chapter.

Tests 1 and 2 were assembled this way.

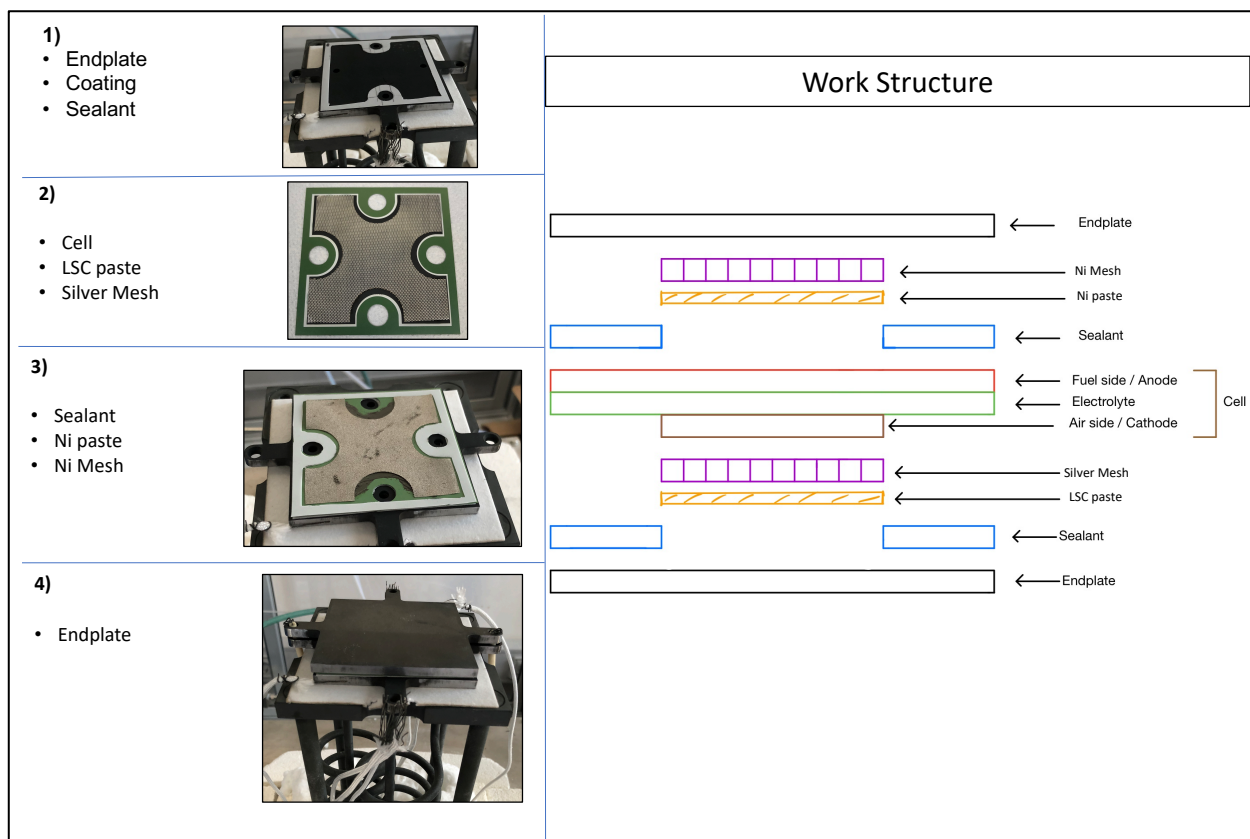


Figure 43: Configuration of test 1 & 2.

3.4.2 SRU Assembly

In this configuration, ICs were added to get a Single Repeat Unit. The assembly was performed layer by layer as previously described, placing the ICs between the cell and the endplates has seen in figure 44. A layer of sealing and an Ag mesh were placed between the endplate and IC to ensure the gas tightness between the gas chambers and the electrical contact respectively. It is worth noting that in this case the cell has been rotated, placing the fuel electrode on the bottom. This means that the upper endplate was coated while the lower one was kept uncoated.

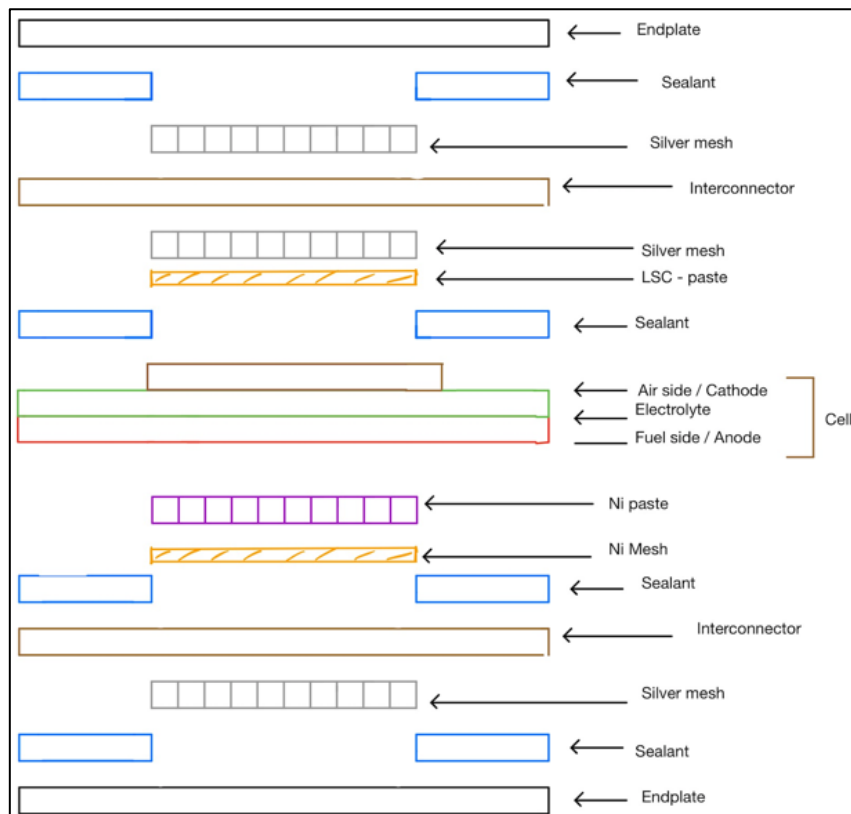


Figure 44: Configuration of test 3 and 4.

The main difference between test 3 and 4 comes from the type of glass sealant that had been used. Test 3 was assembled with the glass sealant 1 as seen on Figure 45 and test 4 with the glass sealant 2 deposited by robocasting as presented on Figure 46.

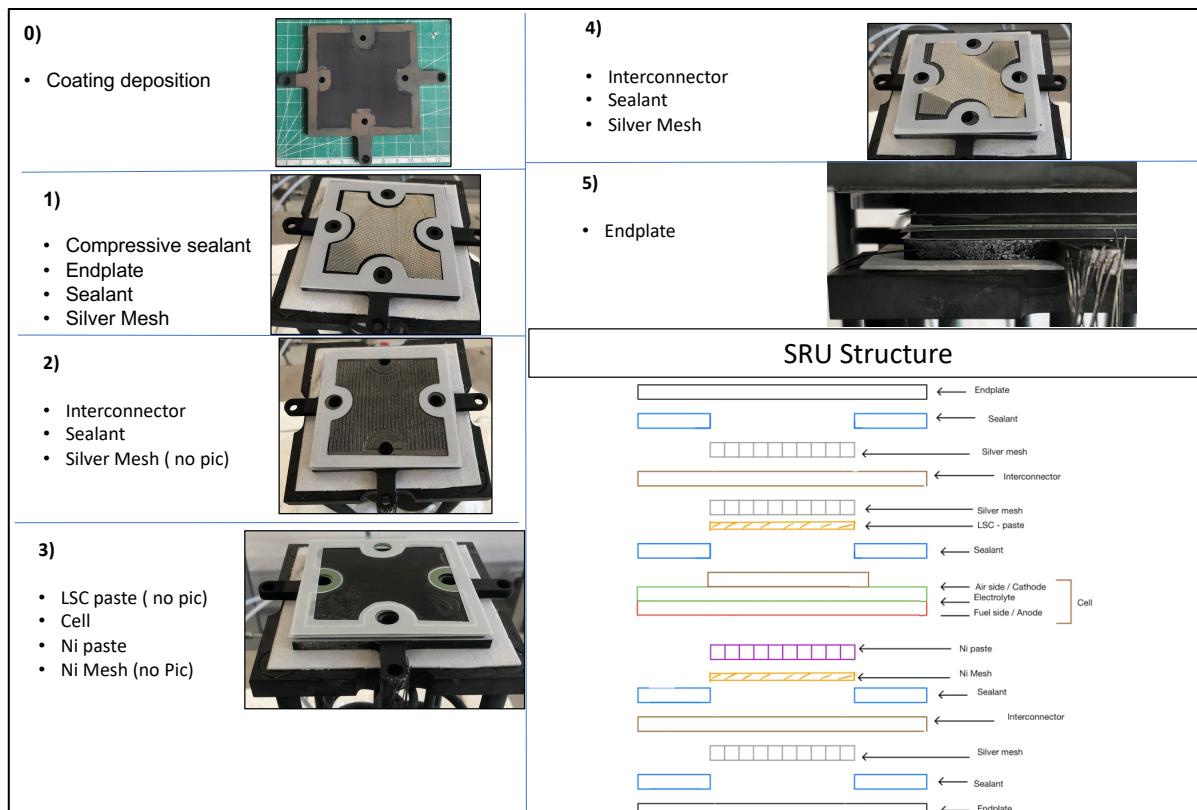


Figure 45: Configuration of test 3

Hence, for the test 4 the deposition has been carried out by robocasting, followed by short drying step in order to consolidate the paste before assembling the rest of the layers. Therefore, all materials were covered by two lines deposition, in order to obtain a suitable size in terms of thickness and width of the sealant.

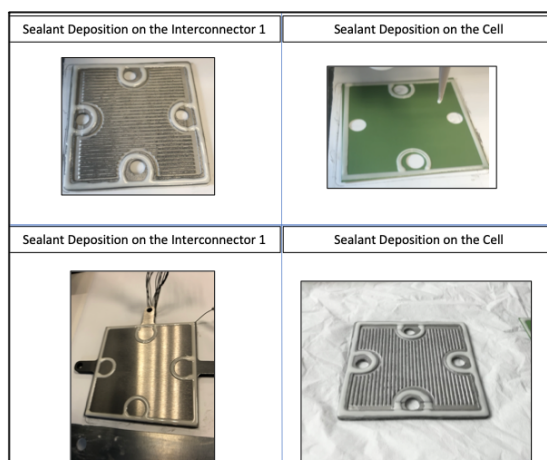


Figure 46: Sealant deposition on different materials.

3.4.3 Test Station

The test bench used for this work is composed by several elements presented in the *figure 47, 48 and 49*. *Figure 47* corresponds to the support plate where the lower endplate is installed. The gas tubes (air inlet and outlet, fuel inlet and outlet) are welded to the plate. The gas tightness and electrical insulation between the lower endplate and the support plate was carried out trying different techniques along the tests as shown in *Figure 48*. In one case, a compressive sealant was tried (Test 1) while in other tests this compressive sealant was impregnated with an alumina slurry in order to improve its efficiency (Test 3 and 4). A sheet of mica combined with rings of sealant 1 was also tried (Test 2). *Table 12* summarizes the specificity of each test.

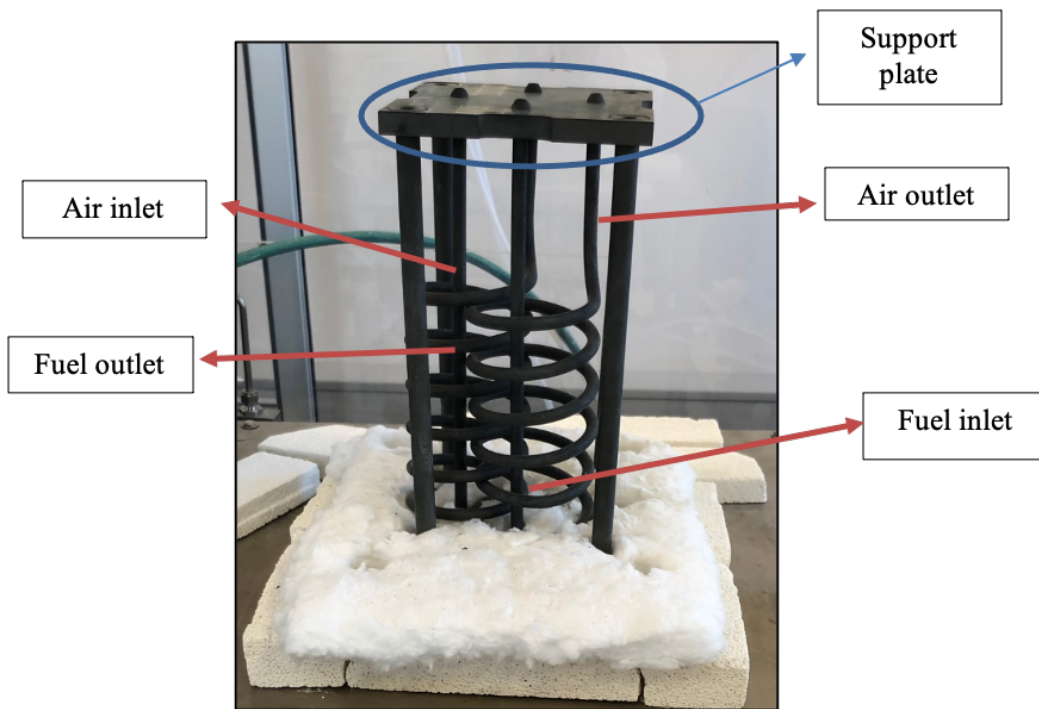


Figure 47: Support station.

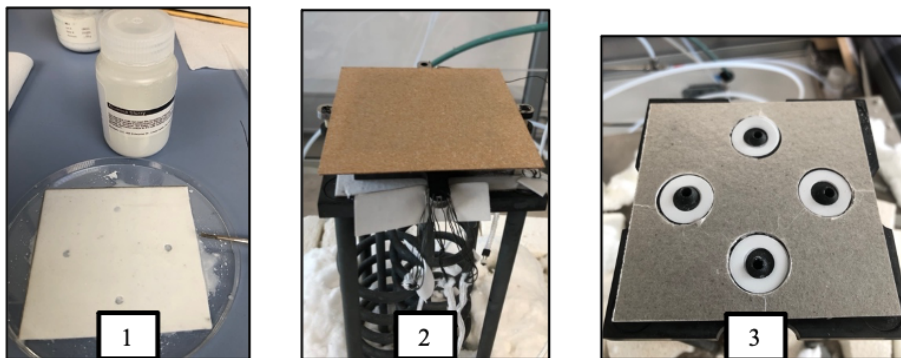


Figure 48: Alumina slurry put on the compressive sealant (1), Mica compressive sealant (2), Mica compressive sealant + 4 rings of sealant 1

Another important component of the station is the tightening system, which allows to apply weight on top the cell/SRU and so, onto the sealants to ensure the gas tightness between all the layers. In this case, the weight is applied using a plate placed on top of the upper endplate with 4 legs that goes out of the oven. Those legs are threaded to tighten with a screw a set of springs with known stiffness. Controlling the length of the springs, the weight applied onto the cell can be known. Test 1 has been carried out by tightening the screw using a regular wrench. However, it appeared that spring's length was not controlled precisely enough to exactly know the weight applied to the cell and if it was equilibrated between the legs. A dynamometric wrench was then used. For all tests, 40 kg were applied, corresponding to 10 kg by springs. The dynamometric wrench was set to 2 N·m to reach this value. A sheet of insulating material was placed between the upper endplate and the compression plate to avoid any short-circuit. Compressive sealant and mica were tested. As already mentioned, the detailed for each test can be found in Table 12.



Figure 49: Station with SRU.

The rest of the elements necessary to set-up a cell or SRU measurements are shown in *Figure 49*. There are electrical cables that have been spot-welded onto the endplates to measure the voltage and allow the current to flow. Special care to avoid short-circuit was required when installing the wires. Finally, two thermocouples were placed close to the cell/SRU in order to control the temperature inside the furnace.

Once all the elements presented above had been installed, the oven was installed as seen on *figure 50, picture b*. The electronic equipment (power supply Kepco and electronic load Mayuno M9812

DC) to perform the electrochemical characterization and the oven controller were located below the station (fig.50, picture a). Electrochemical measurements were then performed using the software M9800 associated to the electronic load, allowing to control the current while measuring the voltage.



Figure50: Electronic equipment (1), Placing of the oven (2).

Table 12: Overview of working strategies.

	Use of IC	Type of glass sealant	Type of insulation between lower endplate and support plate	Tightening technique	Type of insulation between higher endplate and compressive plate
TEST 1	No	Sealant 1 (tape casted)	Compressive	Use of regular wrenches	Compressive
TEST 2	No	Sealant 1 (tape casted)	Mica + glass sealant 1	Use of dynamometric wrench	Mica
TEST 3	Yes	Sealant 1 (tape casted)	Compressive + Alumina slurry	Use of dynamometric wrench	Mica
TEST 4	Yes	Sealant 2 (robocasting)	Compressive + Alumina slurry	Use of dynamometric wrench	Mica

3.5 Test Procedure

Warm-up

The warm-up has been carried out, firstly, considering the sealing treatment of each sealant, and secondly, the desired working temperature to measure the cell performance, such as the OCV, the polarization curve and EIS. In this case, a ramp temperature of 1 °C/min has been set to avoid any problems in terms of CTE, such as cracking or defects related to thermal shock. The final temperature

was set at 800 °C, after performing the sealing thermal treatment detailed in chapter 3.1.1. Heating procedure was carried out under air to burn all the organics present in the current collection inks and to oxide the coating of the endplate and the interconnects in the case of the SRU.

Reduction Procedure

Once the working temperature was achieved, the reduction procedure has been carried out, considering that the NiO, which is presented in the anode, needs to be reduced into Ni, and become an electronic conductor. In order to obtain a homogenous reduction process, gas flows have been changed gradually, following these steps:

Table 13: Reduction procedure.

Cathode atmosphere	Anode atmosphere		Time [min]
Air [l/min]	H ₂ [l/min]	N ₂ [l/min]	
0.5	0	0,5	20
0,5	0,05	0,45	60
0,5	0,1	0,4	10
0,5	0,2	0,3	10
0,5	0,3	0,2	10
0,5	0,4	0,1	10
0,5	0,5	0	10

Once the reduction procedure over, the value of OCV (open circuit voltage) has been checked as first indicator about cell performance, especially to identify any important leakage problem. The OCV corresponds to the maximum value of voltage when no current is flowing. It is typically in a value range of 1.1 - 1.2 V. Below this value it means that molecules of water are present in the atmosphere, coming from the combustion reaction of H₂ and O₂ where leakages are occurring.

Polarization Curves (IV Curves)

The polarization curve is a way to obtain several information about cell performance. It consists in applying a sweep in current and measuring the resulting cell voltage. From this curve it is possible to obtain the total resistance and the output of power density in fuel cell mode (SOFC). In order to avoid any unwanted cell degradation, the current sweep is stopped when the voltage value reach 0,6 V.

Electrochemical Impedance Spectroscopy (EIS)

Electrochemical impedance spectroscopy is a characterization technique to study the behavior of cells in operation at a steady state point. The principle consists in imposing a small perturbation in current (or voltage) of variable frequency around the studied operating point and measuring the resulting voltage (or current). The frequency analysis of the system transfer function or impedance makes it possible to separate and identify the elementary contributions associated with the different processes and interfaces involved during the operation of the cell. This measurement was performed with an impedance analyzer galvanostat/potentiostat Parstat and have been carried out in two different conditions: the first one at OCV and the second one, applying 2 A of current with a signal amplitude of 50 mA.

Degradation Test

The degradation test aims to define the degradation rate of a cell or SRU. It is performed by applying a constant current, monitoring the evolution of the voltage with time. This kind of measurement has been carried out for the tests 3 and 4, choosing the current in each case to obtain an initial voltage around 0.8 V.

4. Results

4.1 Materials Characterization

4.1.1 Glass Characterization

XRD analysis:

As described in the chapter 3.3 of experimental section, XRD analyses were carried out for the two glass-ceramics, to collect information in terms of crystalline phases.

Sealant 1

In *figure 51*, it is shown the XRD results about sealant 1, which was analyzed after its joining treatment. The constant presence of an amorphous halo in the whole diffraction pattern indicates the presence of a residual glassy phase, particularly at $2\theta < 50$. The crystalline phase identified in the *figure 51(b)* is related to $\text{Ba}_5\text{Si}_8\text{O}_{21}$. However, several studies have shown the growth of a different phase: $\text{Ba}_3\text{Si}_2\text{O}_8$. [36].

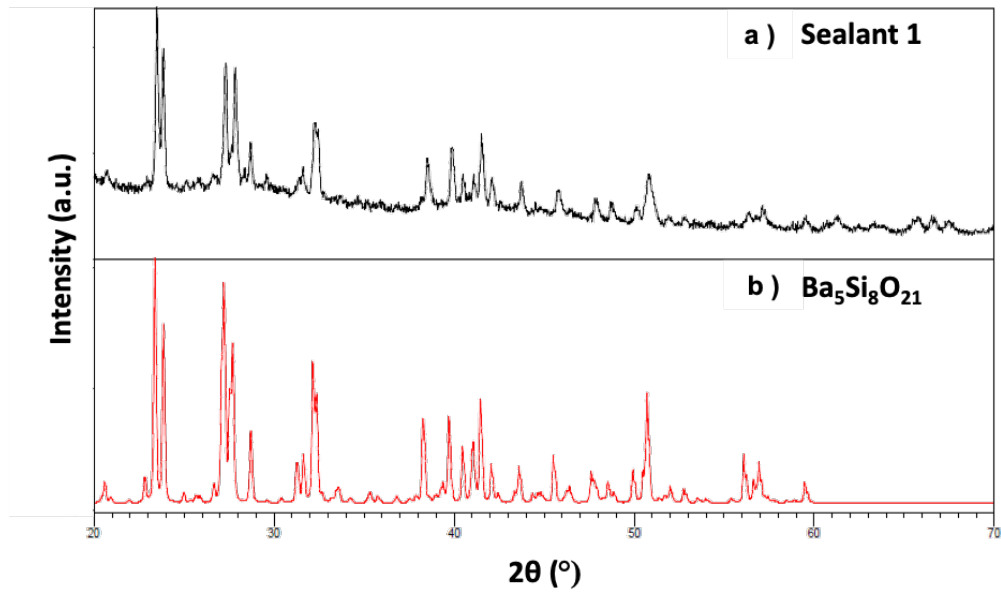


Figure 51: XRD diffraction patterns for Sealant 1, after the sinter-crystallization joining treatment.

Sealant 2

The XRD results of sealant 2 is shown in *figure 52(a)*. Also, in this case it is present an amorphous halo at $2\theta < 50^\circ$ suggesting the presence of a residual glassy phase. Two different phases were identified: SiO_2 and BaSiO_3 . The first one, typically called cristobalite, is characterized by polymorphism behavior. In fact, under determinate conditions, in particular with temperatures around 270°C , it changes its crystalline structure with a strong change in specific volume, which usually leads to formation of stresses in the surrounding material. In addition, this particular effect could be dangerous in terms of mechanical properties, because the stress could lead to cracks formation [37].

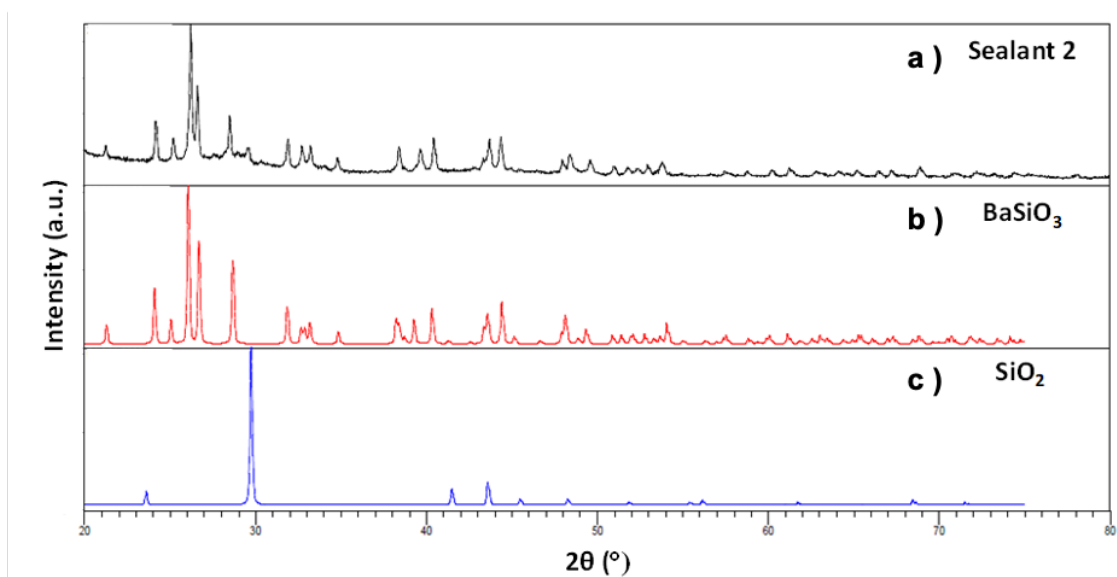


Figure 52: XRD diffraction patterns for Sealant 2, which was subjected to joining treatment before to be analyzed.

DTA analysis:

The DTA analyses, were carried out at Politecnico di Torino, on both sealants. In this experiment, was possible to collect information in terms of glass transition temperatures (T_g), crystallization peak temperature (T_p) and melting temperature (T_m). In particular, the last one corresponds to the melting temperature of the crystallized phases and not to the melting temperatures of the glass. On the other hand, the T_g is identified as the onset temperature of the first endothermic transition at lower temperatures. For the **sealant 1** T_g was measured 623,2 °C, while its crystallization peak temperature was detected at 831.5°C. For **sealant 2** T_g corresponds to 607,8 °C and the crystallization peak was at 763.3°C.

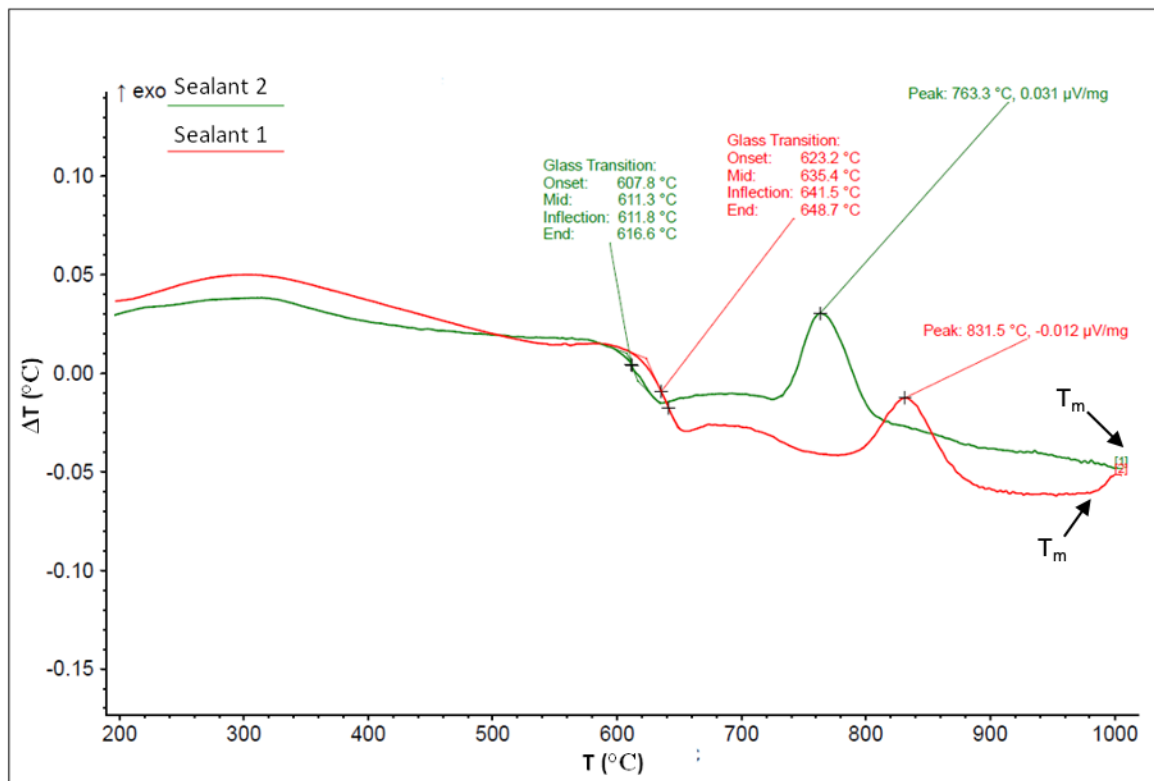


Figure 53: DTA analysis for Sealant 1 and 2

Resistivity Test:

This test was carried out at 800°C in air for 170 hours for the glass sealant 1. The test was carried out applying a 1,3 V in DC mode. The resistance has been measured for all the duration of the test, in order to achieve the resistivity value, following the calculations described in the 3.3.2 chapter of the experimental part. Observing the results reported in *figure 54* it is clear that during the first 40 hours the resistivity decreased and, after that, the value seems to maintain a constant value around $1 \cdot 10^5 \Omega \cdot \text{cm}$. This value is higher than the minimum required for these applications ($10^4 \Omega \cdot \text{cm}$). This

constant value suggest that no detrimental electrochemical reactions took place between the sealant and the interfaced steel, furthermore the formation of conductive phases or “bridges” between the two metallic coupons can be excluded. The formation of these phases can be detrimental in a stack because may lead to short circuits with consequent loss of current.

Concerning sealant 2, it was no possible to record its resistivity due to a short circuit between the two metallic coupons.

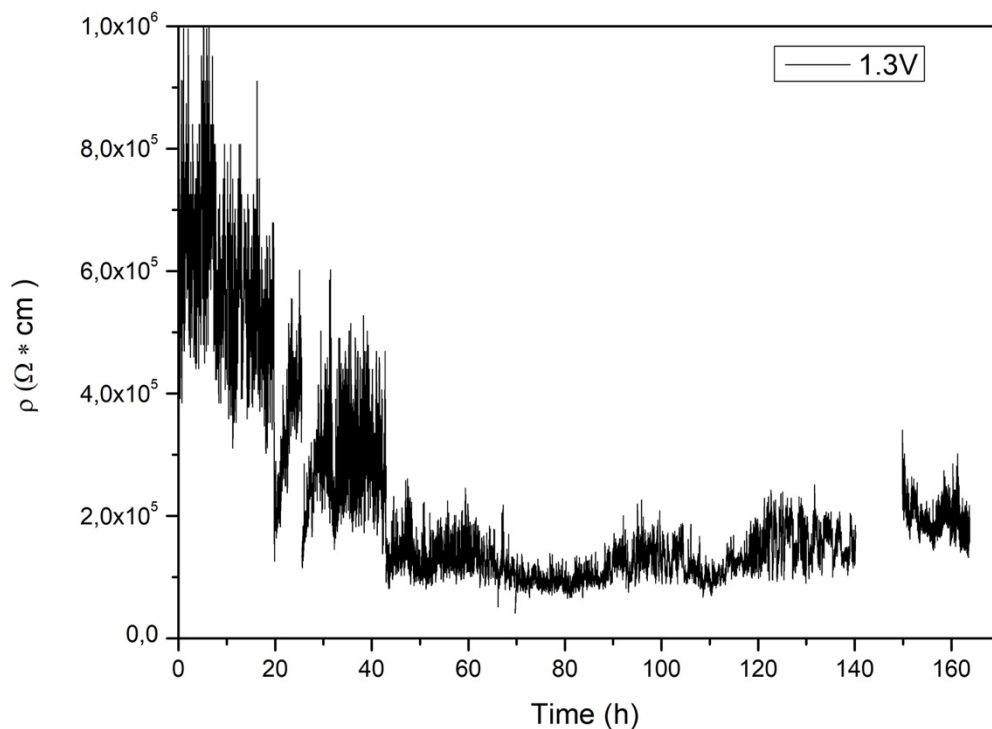


Figure54: Resistivity vs. Time of the samples Crofer22APU/sealant1/Crofer22APU

4.1.2 Compatibility tests

As described in the chapter 3.3.2, eight samples in total were prepared, with different configurations. In this chapter, SEM, XRD and others results are presented. In particular, the focus was placed on the effect of the applied load during the joining treatment and, especially, to the thermomechanical compatibility at the different interfaces.

Sample 1 & 2

The *figure 55* represents the first two small samples prepared, one with a weight applied on the top (*figure 55, b*) and another without the weight. In both sealant 1 was used (*figure 55*). In this case, the sealant 1 was placed between two Crofer 22 APU coupons, where one of them was coated by reduced MC12. The effect of the weight applied is clearly visible considering these 2 following micrographs. In fact, the first one (a) has a thickness around 210 μm , while, the second one (b) around 129 μm , obtaining 80 μm of difference. Another important parameter considered is the porosity. In *figure 55 (b)*, it is possible to see the positive contribution of the weight, because it allows to decrease the porosity percentage. In addition, the residual porosity is not dangerous for the junction, considering that all the pores are closed, thus not leading to open paths for the gasses.

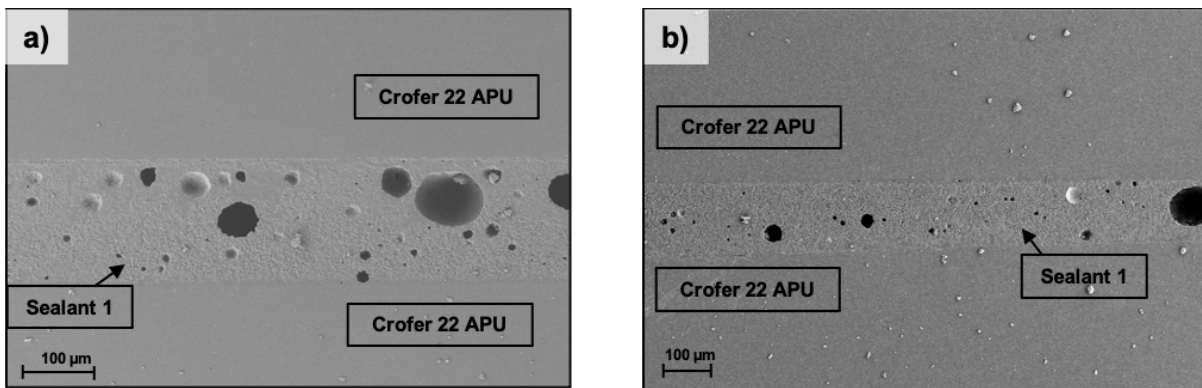


Figure 55: SEM pictures of the joined samples Crofer22APU-sealant1-coatedCrofer22APU: joined without the application of a weight (a) and joined with the application of a weight (b)

The microstructure showed in the *figure 56* confirms the XRD analysis for the sealant 1. The high amount of amorphous phase is in agreement with XRD analysis. It is possible to see the crystalline phase (brighter in the picture) embedded in a consisted residual glassy phase.

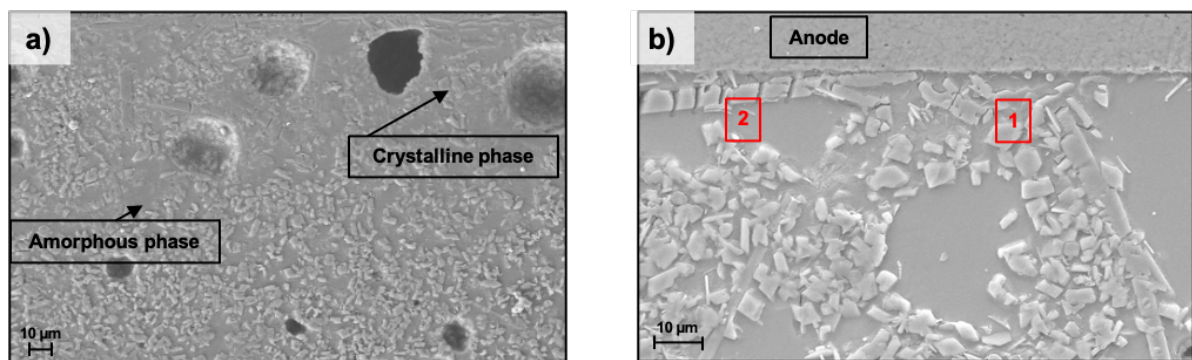


Figure 36: SEM picture of the microstructure of the sealant 1 after the joining thermal treatment (1), points studied by EDS (2).

Table 14: EDS related to picture b of the figure 56

		EDS point	
		1	2
Element (at%)	O	62.13	55.61
	Al	1.96	-
	Mg	3.13	16.29
	Mn	1.40	-
	Ni	1.75	0.68
	Si	16.54	18.89
	Ba	13.09	8.52

Furthermore, in order to investigate the compatibility, more attention was dedicated to the interfaces with both bare and coated (reduced coating) Crofer22APU. In particular, it is possible to see in figure 58 the behavior of the reduced coating interfaced between the sealant 1 and the Crofer 22 APU. This interface shows a perfect adhesion between the materials, without any relevant defects. Concerning the coating, it seems pretty uniform and homogeneous. On the other hand, also the joining with bare Crofer22APU and sealant 1 appears quite regular. These analyses shown the good compatibility of sealant 1 with both bare and coated Crofer22APU.

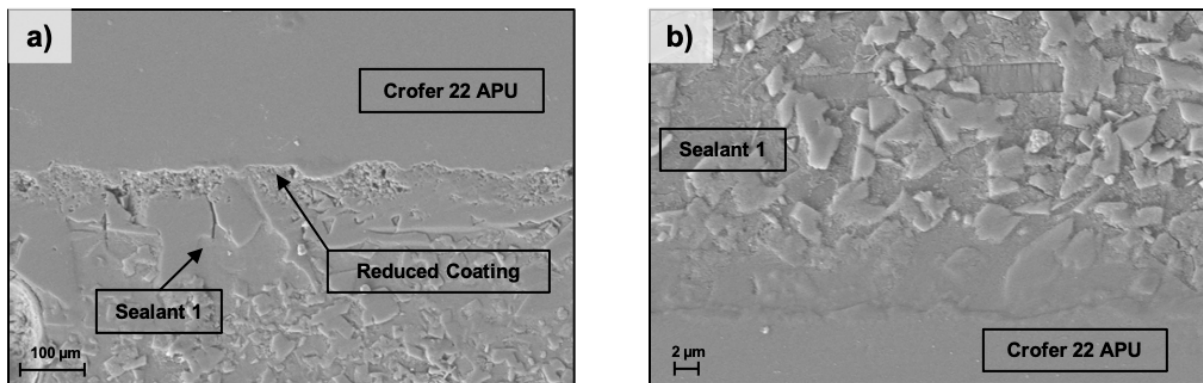


Figure 58: interfaces between the sealant 1 and coated crofer22APU (a) and a bare crofer22APU after the joining thermal treatment(b)

Sample 3 & 4

These samples were prepared using sealant 2. In this case it is possible to see another satisfactory result, in terms of thickness and porosity aspect. In fact, in the sample 3, showed in *figure 5* (a), the sealant has a thickness of 197 µm, while the sample 4, indicated as (b) in the figure, is about 112 µm. That means that, under load condition, it was possible to decrease the thickness of about 85 µm. As in the previous samples, the densification of the sealant appears to be effective with low level of closed porosities. Furthermore, the samples appear to be intact without macroscopic cracks or delamination after the joining treatment

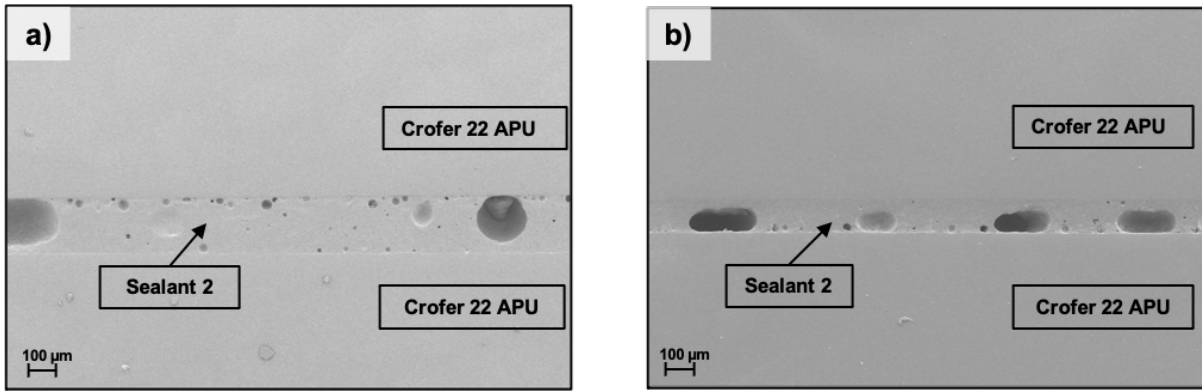


Figure 59: SEM pictures of the joined samples Crofer22APU-sealant2-coatedCrofer22APU: joined without the application of a weight (a) and joined with the application of a weight (b)

In the *figure 60* it is shown the microstructure of sealant 2. In accordance with the XRD analysis, it is visible a residual glassy phase in addition to two different types of crystals. It is possible to distinguish big and regular crystals (brighter) together with smaller ones which appear to be darker in the SEM image (see figure 60b). Another relevant aspect is the presence of microcracks, which are shown more in detail in the picture (b), they seem to surround the small dark crystals which are constituted by cristobalite as detected in the XRD. The polymorphic change of this compound with a strong volume change, lead to the formation of microcracks surrounding the SiO₂ crystals. Despite the overall soundness of the joining, the presence of these microcrack may lead to sealing failure in real operations especially if thermal cycles occur. The EDX analyses reported in table 15 confirmed the formation of SiO₂ that correspond to the dark crystals in the SEM image. Thus, in accordance with XRD analyses. While the composition of the other crystalline phase (point 3 of the EDX) is compatible with BaSiO₃ with a possible incorporation of Ca in the structure.

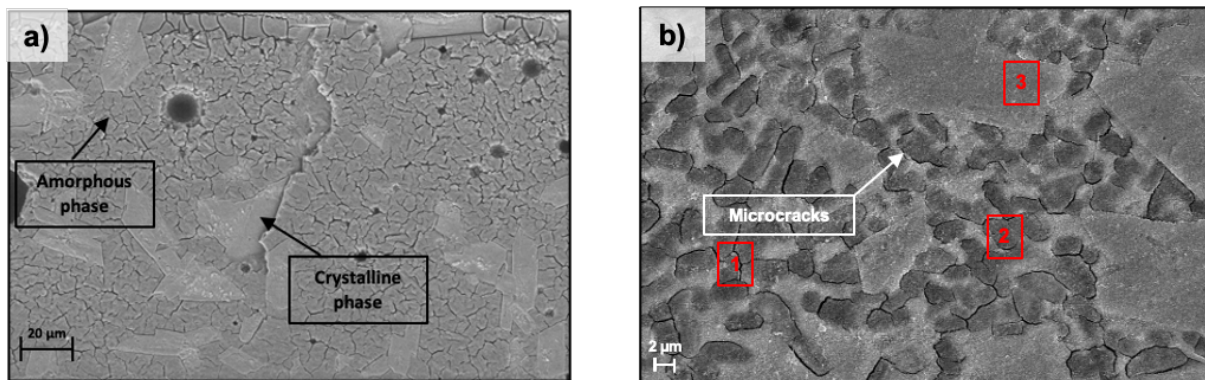


Figure 60: SEM picture of the microstructure of the sealant 2 after the joining thermal treatment (a), SEM picture used for EDS analysis (b).

Table 15: EDS analysis related to the picture (b) in the figure 6

		EDS point		
		1	2	3
Element (at%)	O	45.02	41.36	36.68
	Al	1.75	1.46	-
	Ca	1.16	1.12	16.14
	Si	40.28	43.96	32.73
	Ba	11.79	12.10	13.85
	Fe	-	-	0.60

In addition, the two interfaces were studied, the micrographs are reported in *figure 61*. In the picture (a) is possible to see the adhesion between sealant – coating – steel. It is clear the good match between all materials and, that there are not any relevant defects. The coating appears to be homogeneous and well densified; it shows an excellent compatibility with other materials. On the other hands in figure 61 (b) the interface with bare Crofer22APU is reported. Also, in this case the sealant appears to be well bonded to the steel without presence of delamination or cracks due to thermal mismatch or formation of detrimental phases. Thus, suggesting the good compatibility of sealant 2 with both bare and coated Crofer22APU.

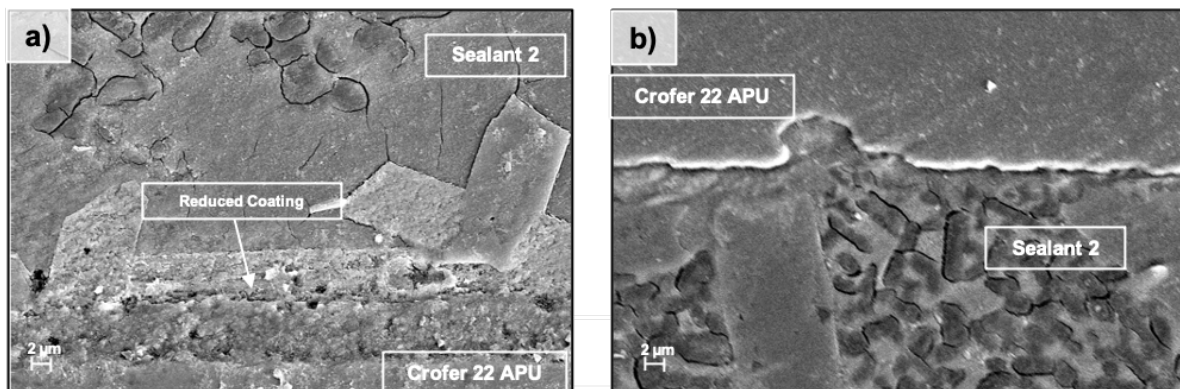


Figure 61: interfaces between the sealant 2 and coated crofer 22APU (a) and bare crofer22APU (b) after the joining thermal treatment.

Sample 5 & 6

In this case, the sealant 1 was in contact with the IC, both bare on one side of the sample and coated on the other side. As described with the sample 1&2 and 3&4, both junctions appear without any damages and with an excellent adhesion among all materials. The thickness measure of the sample without weight (a) is 153 µm, while, the sample with weight (b) 94 µm. This highlights the importance of the application of a light weight to the joining in order to reach a thickness that would not compromise the contact between the meshes and the IC in the real SRU setup.

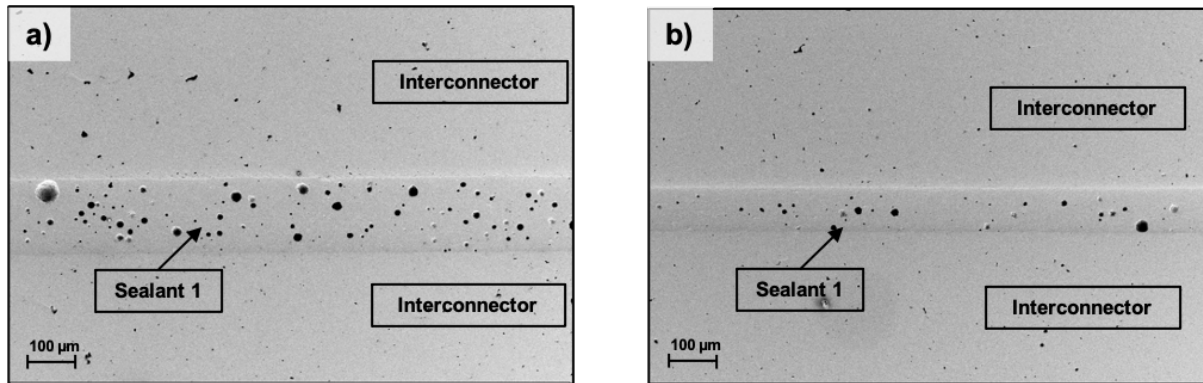


Figure 62: SEM pictures of the joined samples IC-sealant1-coatedIC: joined without the application of a weight (a) joined with the application of a weight (b).

The figure 63 shows the 2 interfaces: the first one between sealant – coating – IC (figure 63a), the second one sealant – IC (figure 63b). In both the cases, the adhesion seems to be perfect in terms of materials compatibility. Also, the coating appears as homogeneous and densified.

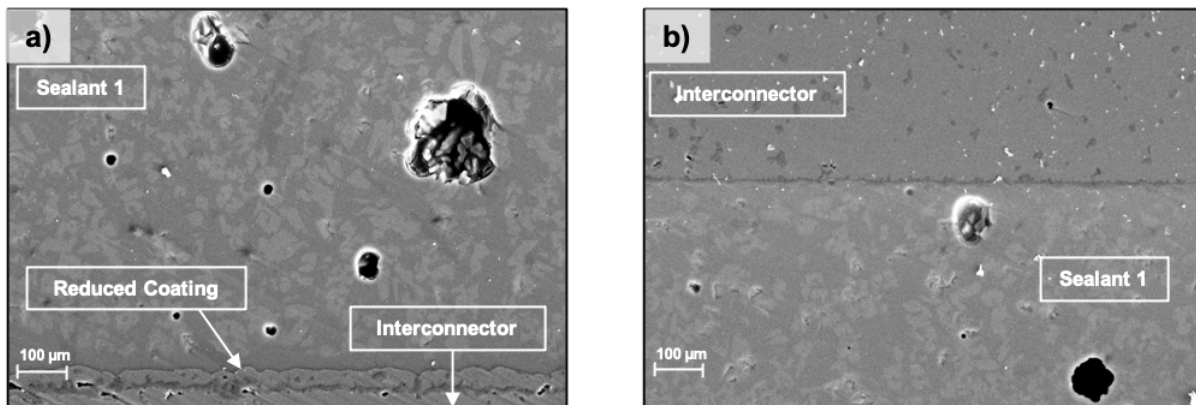


Figure 63: interfaces between the sealant 1 and coated IC (a) and bare IC (b) after the joining thermal treatment.

Sample 7 & 8

Sealant 2 was tested as well in contact with the IC as described for sealant 1. The micrographs related to this samples are reported in figure 64. The thickness of sample 7 is 123 μm, while 75 μm for the sample 8. Once more, adding a weight has been possible obtaining a sufficient thickness decreased in order to guarantee a good contact in the SRU. The joining appears to be intact a free of defects with an exceptionally low level of porosity.

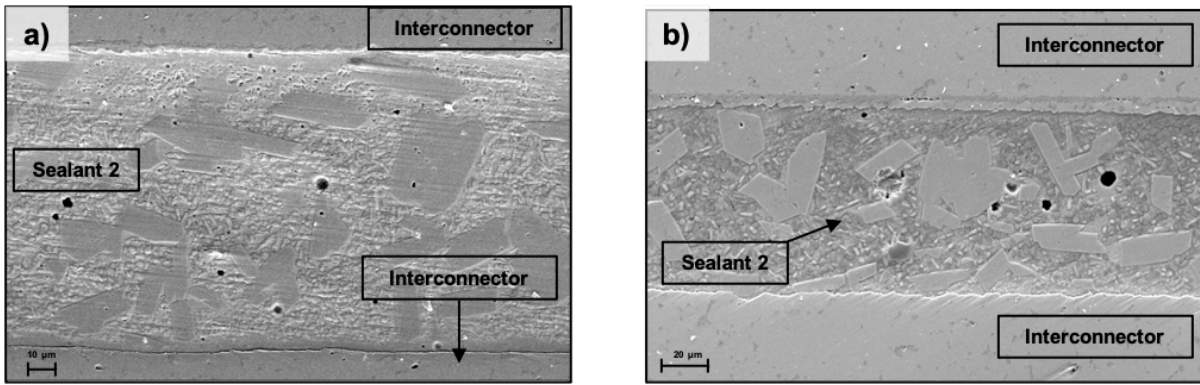


Figure 64: SEM pictures of the joined samples IC-sealant2-coatedIC: joined without the application of a weight (a) joined with the application of a weight (b)

In figure 65 are reported SEM images collected at higher magnification focusing at the interfaces of the sealant with both bare and coated IC. The compatibility of the sealant with these materials appears to be excellent.

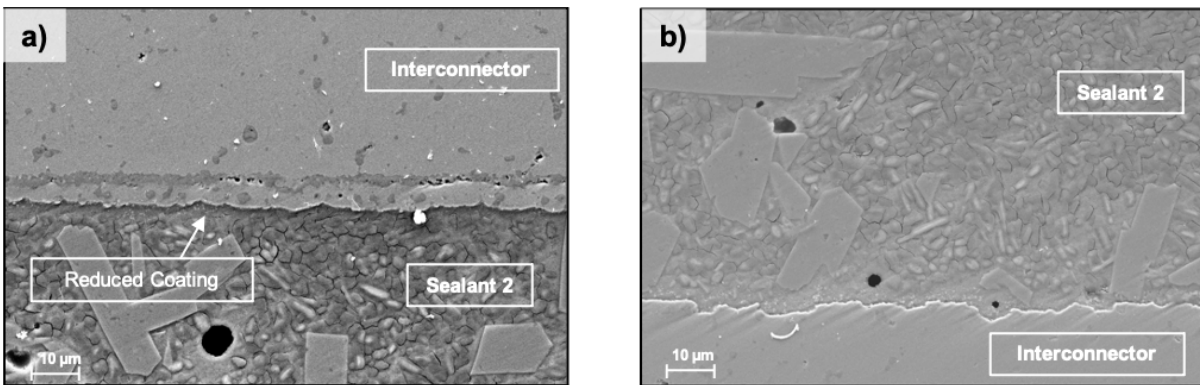


Figure 65: interfaces between the sealant 2 and bare IC (a) coated IC after the joining thermal treatment(b)

Sample with cell – Sealant 2

As described in the introduction part, anode supported cells were used in the present work. Since in the SRU design adopted here, the sealant has to be placed in contact with both the electrolyte and the anode of a cell, small samples were produced in order to study the compatibility of the sealants with these materials. In order to study this, sandwich samples were produced Crofer22APU/sealant/cell/sealant/Crofer22APU, in this way it was possible to interface the sealant with both sides of the cell reproducing the situation of a real operating SRU/cell. The SEM reported in figure 66 confirmed the compatibility of sealant 2 with the cell as well.

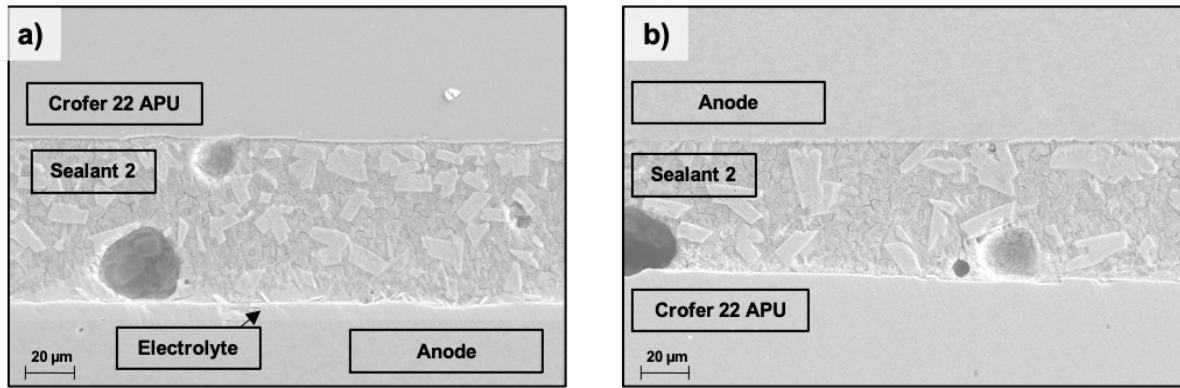


Figure 66: SEM pictures of the joined samples with the cell and sealant 2. Picture of air side (a) Picture of fuel side (b)

Particular attention was dedicated to the interfaces with anode and electrolyte reported in figure 67. The compatibility with the electrolyte is clear, this was not surprising since these sealants are tailored to be compatible with the electrolyte in typical stack design. On the other hand, the interesting results was its compatibility with the anode. Indeed, despite the porous nature of the electrode the sealants did not infiltrated excessively its counterpart without the formation of any defects at the interface. EDX analyses were carried out as well. The EDX results are summarized in table 16.

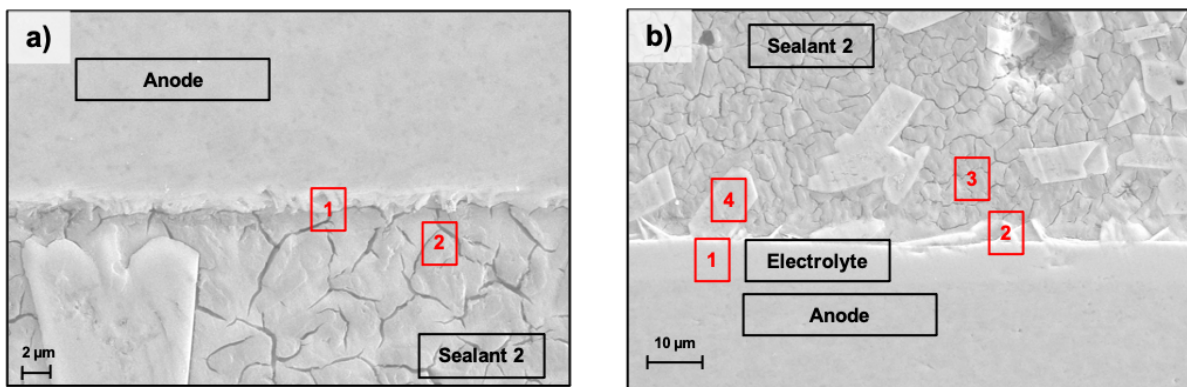


Figure 67: 2 particular interfaces studied by EDS.

Table 16: (a) = EDS related to Figure 13 (a), (b) = EDS related to Figure 13 (b)

a)		EDS point	
		1	2
Element (at%)	O	51.94	58.87
	Al	2.76	5.31
	Zn	-	1.09
	Ni	7.65	1.34
	Si	-	20.48
	Ba	18.22	10.73
	Ca	0.79	2.18

b)		EDS point			
		1	2	3	4
Element (at%)	O	71.57	79.63	73.99	66.83
	Al	-	1.24	3.33	2.98
	Zr	27.56	6.83	6.83	19.43
	Ni	0.88	0.31	0.36	-
	Si	-	6.26	11.66	18.24
	Ba	-	4.11	8.15	8.56
	Ca	-	1.21	1.84	3.38

Sample with cell – Sealant 1

In *figure 68* it is possible to see the interaction between the sealant 1 and the cell, particularly with the anode and the electrolyte side. In the picture on the left side the thickness of the electrolyte is definitely visible, as a dense and constant layer, between the sealant and the anode. On the right side the porous structure of the anode adheres perfectly with the sealant, as described with the previous paragraph.

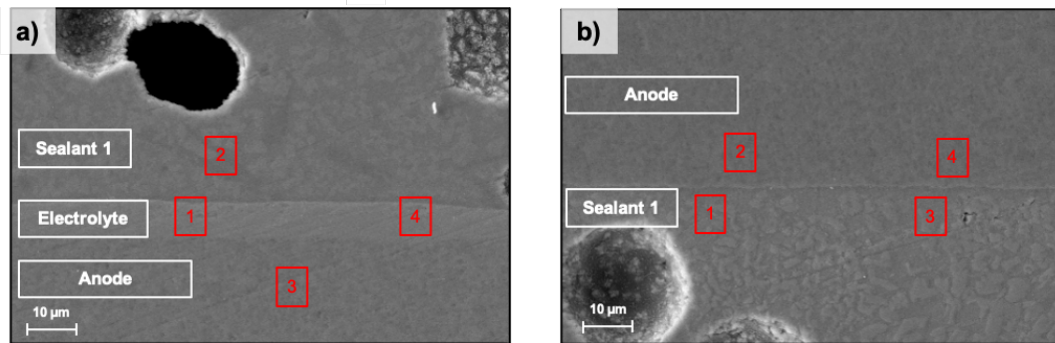


Figure 68: SEM pictures of the joined samples with the cell and sealant 1. Picture interface with the electrolyte (a)
Picture of the interface with anode (b)

Table17: (a) EDS related to Figure 14(a), (b)= EDS related to figure 14 (b)

a)		EDS point			
		1	2	3	4
Element (at%)	O	53.41	54.95	52.58	50.11
	Si	21.51	-	23.50	-
	Ni	1.12	19.85	1.23	30.46
	Zr	-	25.20	-	19.43
	Al	2.27	-	1.82	-
	Mg	4.61	-	3.35	-
	Fe	1.72	-	1.61	-
	Ba	15.37	-	15.91	-

b)		EDS point			
		1	2	3	4
Element (at%)	O	54.50	42.81	49.09	53.60
	Si	-	30.38	-	-
	Ni	1.99	-	24.62	2.11
	Zr	42.34	-	26.29	44.30
	Al	-	1.62	-	-
	Mg	-	3.44	-	-
	Fe	0.70	-	-	-
	Ba	-	21.75	-	-

4.1.3 Coating characterization

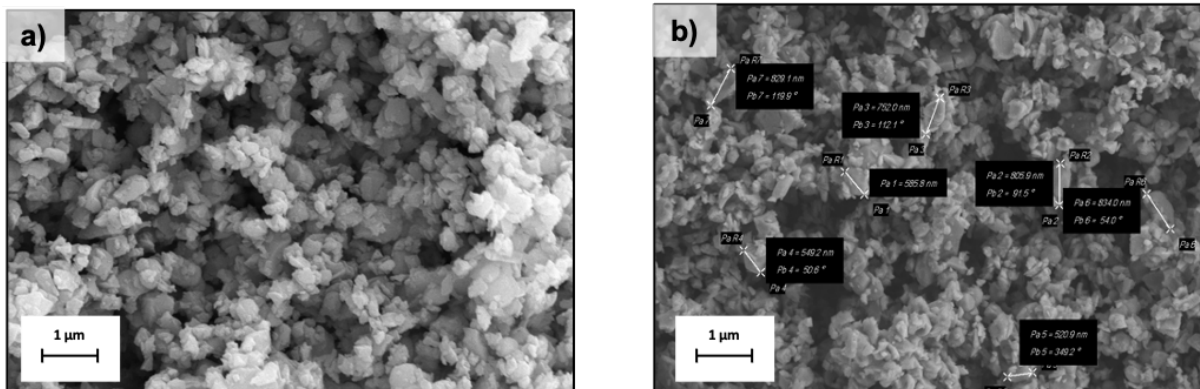


Figure 69: SEM pictures of MC12 powder used for the coating (a). Some details of MC12 material (b)

The microstructure of the coating has been studied by SEM characterization. It shows a various shapes of grain size, particularly an average size of ≈ 700 nm. The composition has been analyzed by EDS (Table 18) and XRD (figure 70 and 71). The atomic percentage of C and Au detected is due to the presence of carbon tape, and the gold for the sputtering deposition, which has been carried out with a gold layer.

Table 18: EDS analysis of MC12 powder.

EDS		
Element	Weight%	Atomic%
C K	6.46	19.52
O K	20.72	46.98
Mn K	14.25	9.41
Co K	30.87	18.99
Au M	27.69	5.10
Totals	100.00	

On the other hand, XRD analyses were carried out: firstly, directly in the powders as received, in order to verify the coating composition, secondly, on the reduced powders to prove effectively the changed composition of MnCo_2O_4 in metallic Co and MnO. As it is possible to verify directly in the XRD analysis illustrated in the figure 17, the composition expected was confirmed.

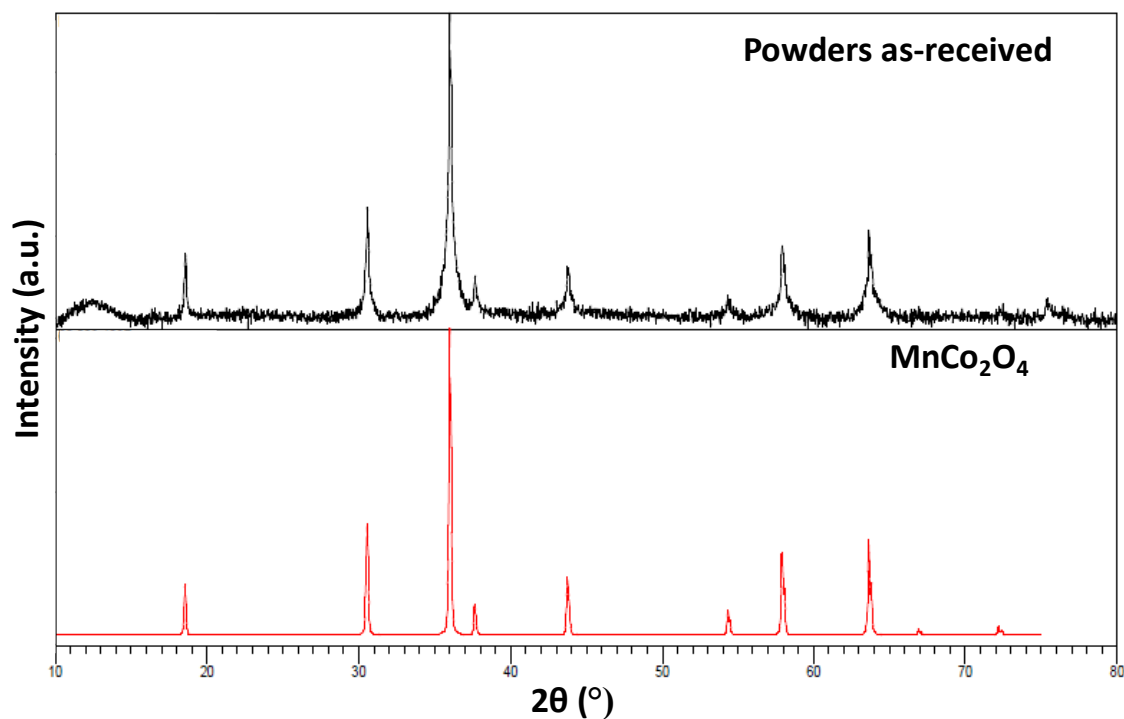


Figure 70: XRD diffraction patterns for MC12 as received.

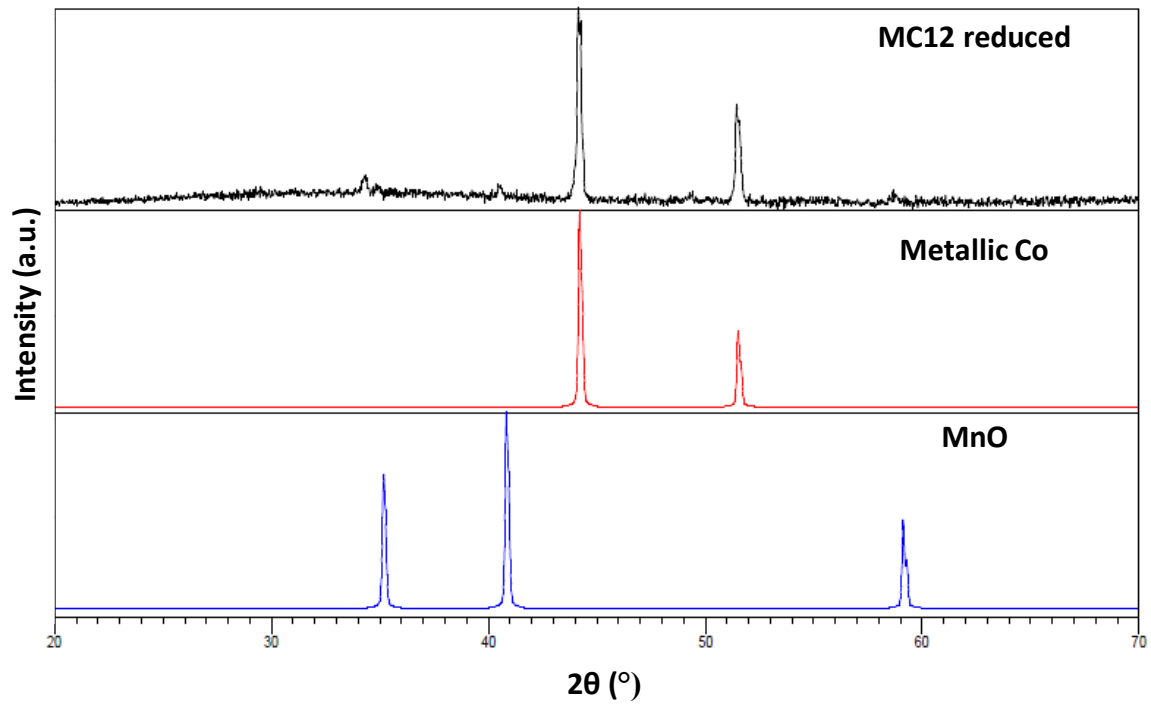


Figure 71: XRD diffraction patterns for the reduced MC12, which has been subjected to the sintering treatment before to be analyzed.

Light scattering

Results of light scattering are reported in figure 72. The measured d50 was 1.46 μm . This value is far higher than the one measured with SEM. This may be due to aggregation of MC12 particles in the ethanol suspension used or aerography.

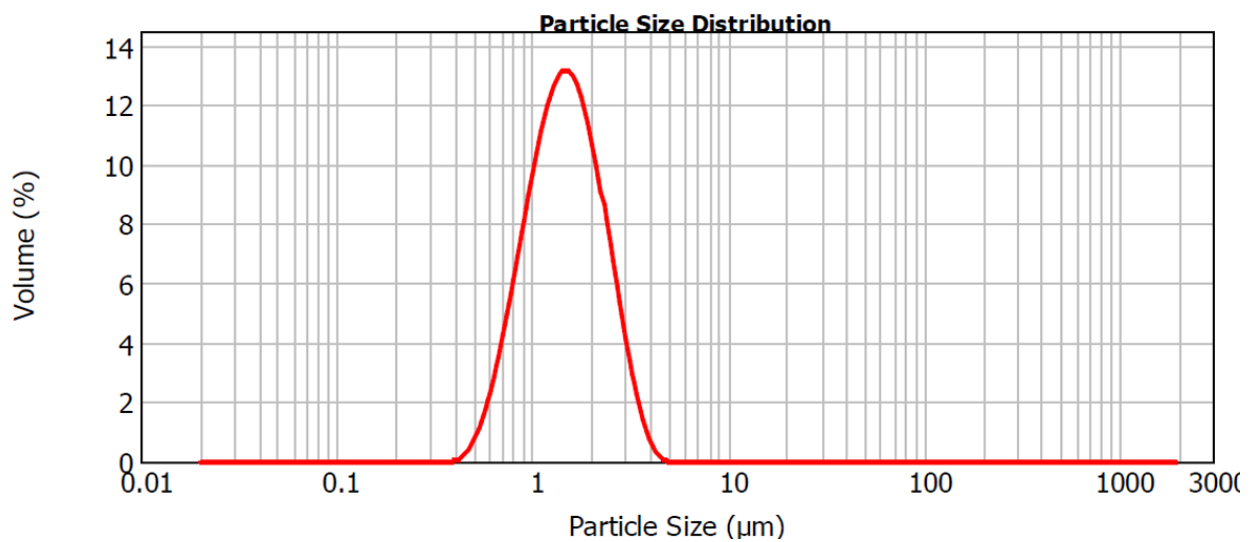


Figure 72: Results of light scattering on MC12 powders.

4.2 Single cell and SRU characterization

Once small samples have been analyzed, the next step has been focusing on the characterization of single cell and the SRU.

4.2.1 Test 1

Electrochemical characterization

Here below is shown the polarization curve of the first test obtained with 0,2 L/min of H₂ and 0,2 L/min of N₂ at the anode and 0,5 L/min of air at the cathode. The current density has been calculated dividing the current value by the cell surface, while, the power has been calculated by multiplying the voltage by the current.

Firstly, it can be seen that the OCV, around 0,7 V, is way lower than the expected value (1,2 V) and can originate from leakages. In the same way, the polarization curve is decreasing sharply, reaching 0 V when producing 3 A, meaning that the cell is not performing as expected. Due to those values, the test had been stopped.

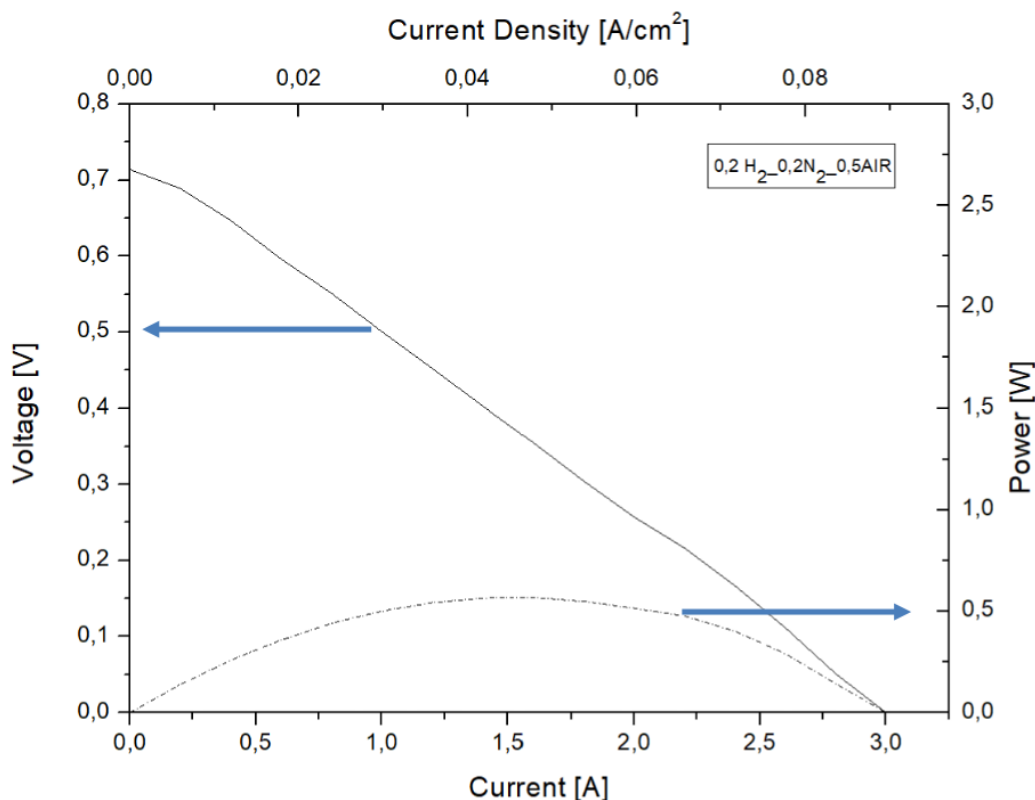


Figure 73: Polarization Curve of test 1.

Post-mortem analysis

Control of the gas tightness

Once the test has been concluded, the next step aimed to identify the origin of the bad performance reported above. The first investigation was performed in-situ, before dismantling the cell from the set-up, to see if gas leak could be detected. The following pictures on Figure 74 show the main problems that have been detected. First, the set-up was not perfectly flat, meaning that the pressure was not applied equally on the glass sealant. Then, by flowing N_2 on the system and using a liquid to detect the leak (commercial liquid composed by water and soap), leakages were found in different zones: on one corner of the cell, in the middle of one side as well as at the interface between the support plate and the lower endplate. It appears that the endplates were not flat enough to allow a perfect sealing of the cell. Moreover, these results evidenced a clear problem of tightness between the support plate and the lower endplate. Compressive sealing was used in this test but applying less weight than what is required. Modification of this part must be conducted for future tests.

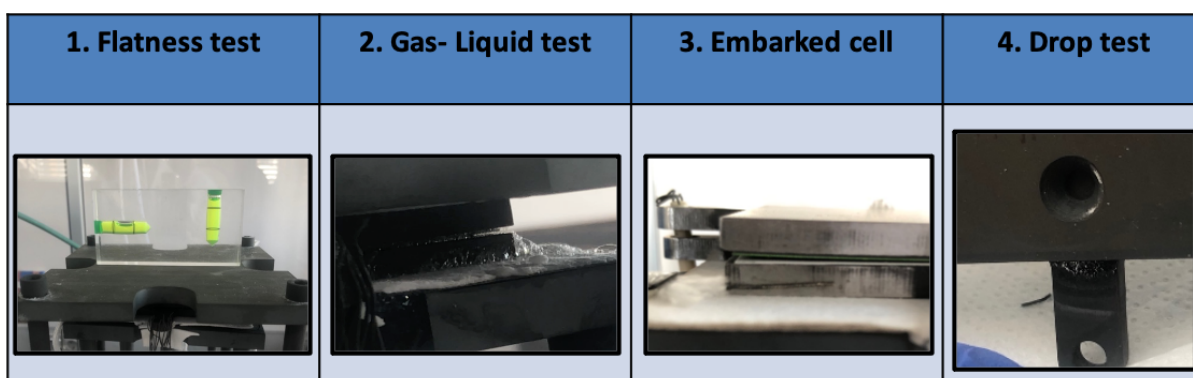


Figure 74: Problems related to test 1.

Analysis of the dismantled cell

The sandwich of endplates and the single cell has been opened in order to observe any issues like lack of electrical contact, broken cell, hotspots, etc... As seen on *Figure 75 (a)*, the endplate is divided in two colors: a grey zone and a black one. This is equivalent to the green and grey color of the anode on *figure 75 (b)*. This corresponds to a gas mixing of H_2 and Air due to an important leakage, that burnt where they met. Consequently, part of the anode that was in contact with air re-oxidized into the NiO (green color), stopping to be operational. In term of performance, the leakage induces the presence of water into the anode chamber (product of the combustion of O_2 and H_2), corresponding to a decrease of the OCV compared to pure H_2 conditions. Moreover, having part of the anode re-oxidized decreases the active area of the cell and then lower the performance.

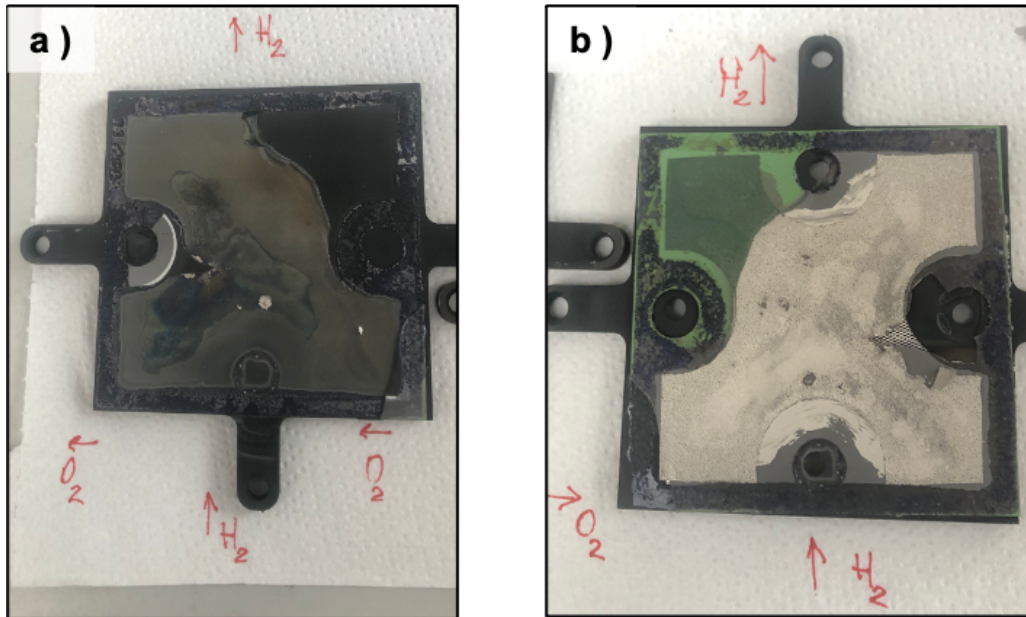


Figure 75: upper Endplate (a), Lowest endplate + coating (b)

Progress # 1

Once the post-mortem has been completed, it has been concluded that particular attention in terms of flatness of the different materials had to be paid to limit gas leakages has to be paid.

4.2.2 Test 2

Considering the results presented in the previous paragraph, the endplate was machined to ensure their perfect flatness, a Mica sealant + 4 rings of sealant 1 and a dynamometric key have been used to improve the tightness of this test. In figure 76, it can be seen the single cell before operation, where there is no gap on the corner in comparison with the test 1.



Figure 76: sandwich of all materials in the test 2.

Electrochemical characterization

The second test showed a clear improvement in terms of OCV, reaching 0.85 V, but still below the theoretical value of 1.2 V. Moreover, the iV-curve presented lower performance than for test 1. The gas flow had been set to 0,5 L/min of H₂ and 1,25 of Air L/min at 800°C.

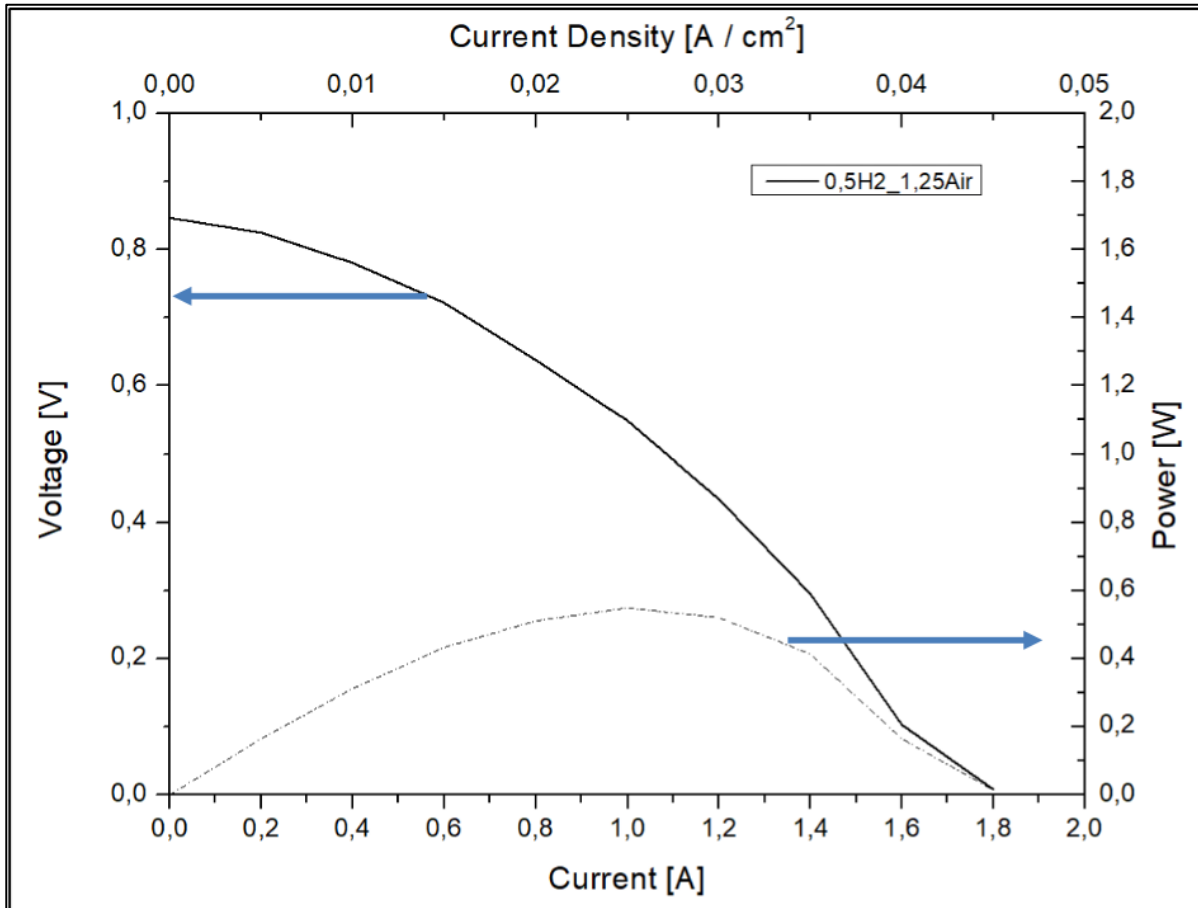


Figure 77: Polarization Curve of test 2.

Post-mortem analysis

Control of the gas tightness

Observing the following pictures, a problem about gas leaks was identified. Especially in the figure 78 (b), it is possible to see that the rings of sealant 1 did not attach to the support plate, probably due to a problem in terms of CTE mismatch between the sealant and support plate. In fact, the support plate is in Inconel material, which has a CTE in the order of 13 [$10^{-6}/^{\circ}\text{K}$], while the sealant 1 has a CTE of 9,9 [$10^{-6}/^{\circ}\text{K}$]. No important leak had been detected around the cell.

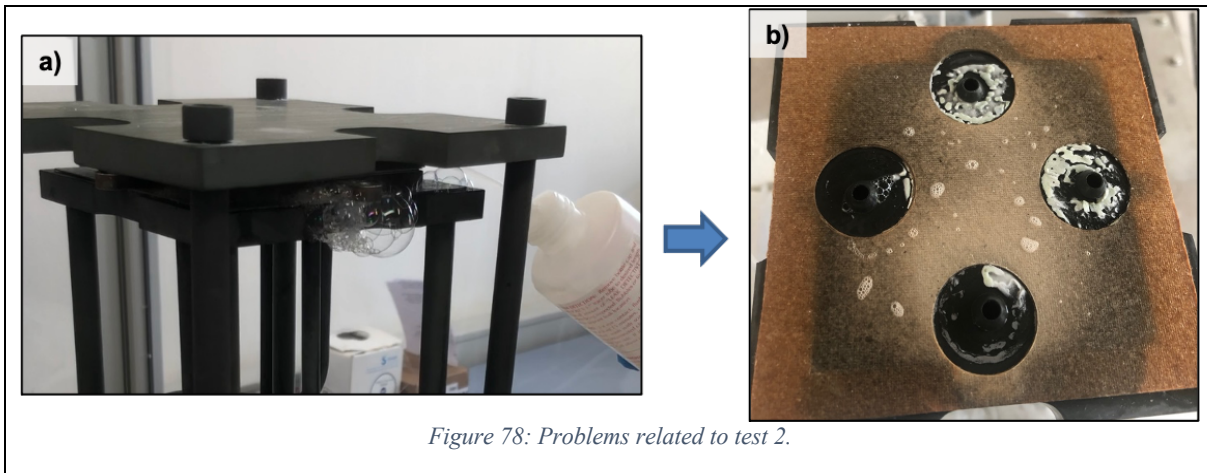


Figure 78: Problems related to test 2.

Analysis of the dismantled cell

In this case, as shown on Figure 79, no leakage was visible at the surface of the cell. The anode was well reduced. Moreover, it could be seen that the LSC paste on top of the cathode was perfectly in contact with the silver mesh, the sealant had a suitable thickness, allowing the different layers to be in contact. In addition, in both picture it is possible to observe a blue color, which corresponds probably to some Co enriched phases, coming from the coating of the endplate in contact with the sealing.

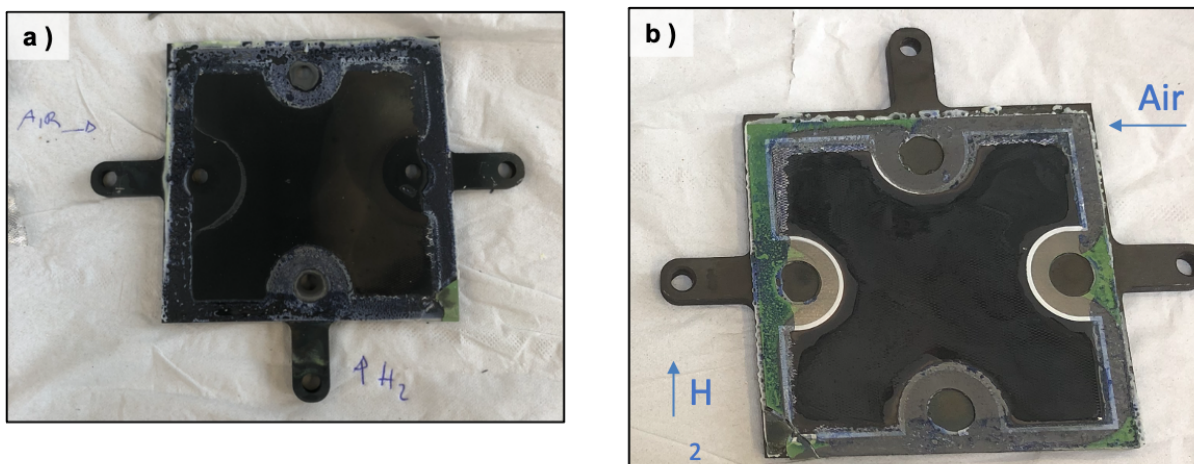


Figure 79: Fuel side view (a), Air side view (b)

Progress # 2

Seeing that the leakage problems on the cells were solved by controlling the flatness of the endplates, the machining step of the endplates entered into the assembling protocol for the next tests. However, the problem of leakages between the support plate and the lower plate could not be solved by using mica. Another solution was decided to be implemented in the next tests: the use of the compressive sealant adding an alumina slurry.

4.2.3 Test 3

Test 3 consisted in testing a single repeat unit (SRU). Adding the IC was a mandatory step in this work but the decision to perform this measurement before improving the one with a single cell was taken to lower the gas pressure on the support plate-lower endplate junction, by facilitating the gas flow thanks to channels of the IC. Figure 80 shows that no defects were visible during the assembling step of the SRU, thanks to perfect flatness of the different layers.



Figure 80: sandwich of all materials in the test 3

Electrochemical characterization

For the first time it has been possible to measure, not only the IV curves, but also Electrochemical Impedance Spectroscopy (EIS) curves, both at 800 °C.

In the Figure 81 (a), it is possible to observe the test performance during different days, sending 1,25 L/min of Air and 0,5 L/min of H₂. The corresponding degradation is presented in the figure 83. On the other hand, in the right picture it is possible to see the evolution of the performance with different gas conditions. First of all, it is possible to see that an OCV higher between 1,1 and 1,2 V was obtained in all the conditions, meaning that there were no gas leakages. Moreover, flowing 2,5 L/min of air and 1 L/min of H₂, the current reached a value around 16 A at 0,65 V corresponding to 10 W of power.

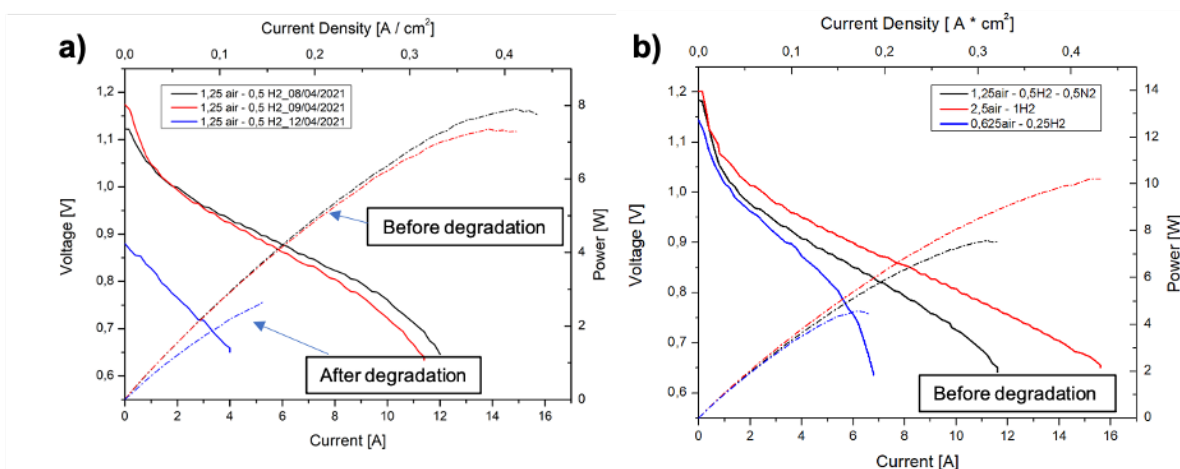


Figure 81: Polarization Curve of test 2, (a) with different time and (b) with different gas flows conditions.

Concerning final results of EIS done for the test 3, they are shown in the *figure 82*. The impedance spectra presented on the left was obtained in OCV condition, meaning without any current applied. Here the value of the serial resistance, which gives information about electrolyte resistance and the electrical contacts between the layers, is, approximately, $0,7 \Omega \cdot \text{cm}^2$. Under current, as seen on the right side applying 2 A, the serial resistance stays unchanged while the total resistance, corresponding to the final intersection of the curve with the x-axis (if the semi-circle was complete) is around $2,5-3 \Omega \cdot \text{cm}^2$. Actually, this value corresponds to the slope of the polarization curve at the same current, 2 A in this case. Both values are high and should be lowered to obtain performance closer to state-of-the-art ones.

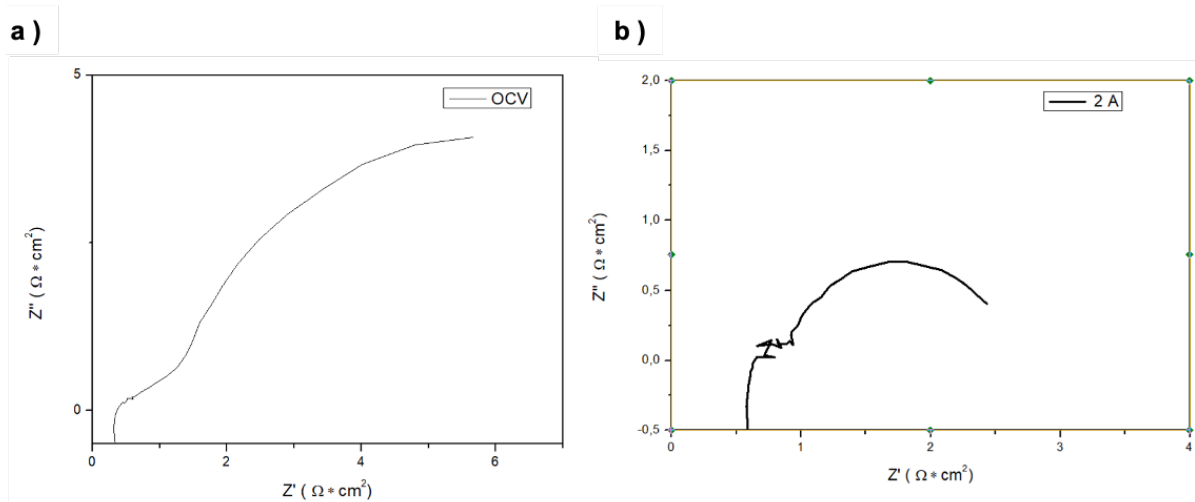


Figure 82: Curves EIS of the test 3 in OCV condition (a) and 2A condition (b).

In the *figure 83* the trend of the degradation test is presented. It consists in applying a constant value of current (in this case 8,5 A), with determined parameters, which are shown in the graph at the top right, monitoring the voltage behavior during the time. In this case it is clear that the test failed only after few hours because the cell voltage rapidly dropped to low values.

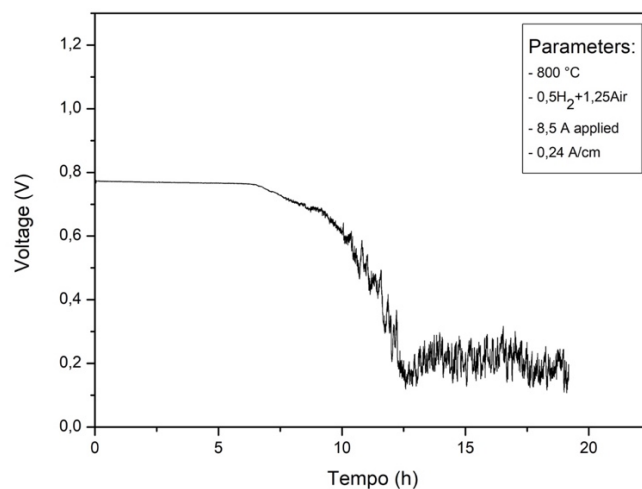


Figure 83: Degradation test of test 3.

Post-mortem analysis

Analysis of the dismantled SRU

In the *figure 84* it is possible to observe the SRU dismantled with the different part presented separately. In the picture a) the coating appears in perfect condition, the sealant has a very adherent aspect to the endplate as well as to the IC frame in b), and few traces of Co enriched phase are present corresponding to junction between the coating and the sealant. In addition, several marks of silver mesh are visible in the coating, which indicates a good contact between those layers. In the end, in c) is shown the cathode side of the IC, where a burning area appears evident on the left part of the IC.

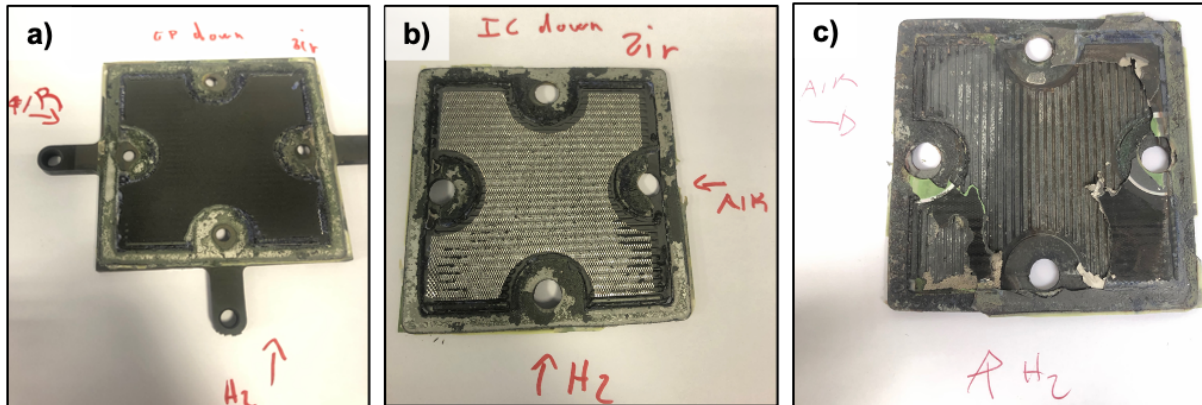


Figure 84: Endplate with coating (a), IC with silver mesh (b) and Air side view (c)

SEM investigation

In the *figure 85 and 86* some SEM pictures are shown, taken from the cell and the IC in contact with the anode, embedded together in a resin and polished. They were taken respectively on the anode side and the cathode side. Sealant 1 seems to adapt perfectly with all materials and it presents a randomly concentration of small crystals. In addition, it has a thickness suitable for this application, around 80 μm , in agreement with the goals described in the 3.3.1 chapter of the Experimental part.

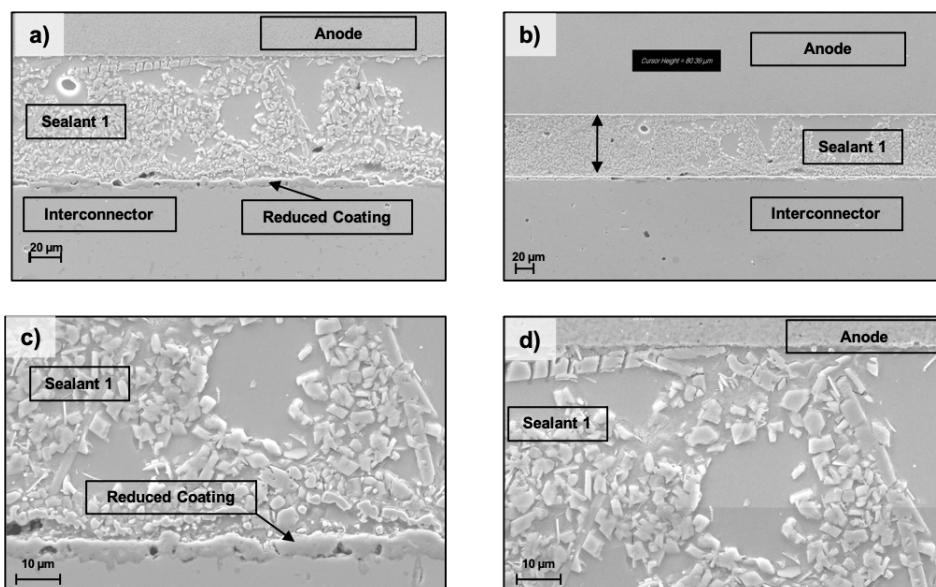


Figure 85: SEM pictures of the joined samples in the Anode side

On the other hand, in the following figure, it is possible to get other information. For example, the **coating**, which covered the IC, appears dense and quite regular, with a thickness of 12,76 μm . At least, another interesting aspect is that it has been possible to observe the typical barrier layer of Gadolinium – doped Ceria (GDC), as shown in (b).

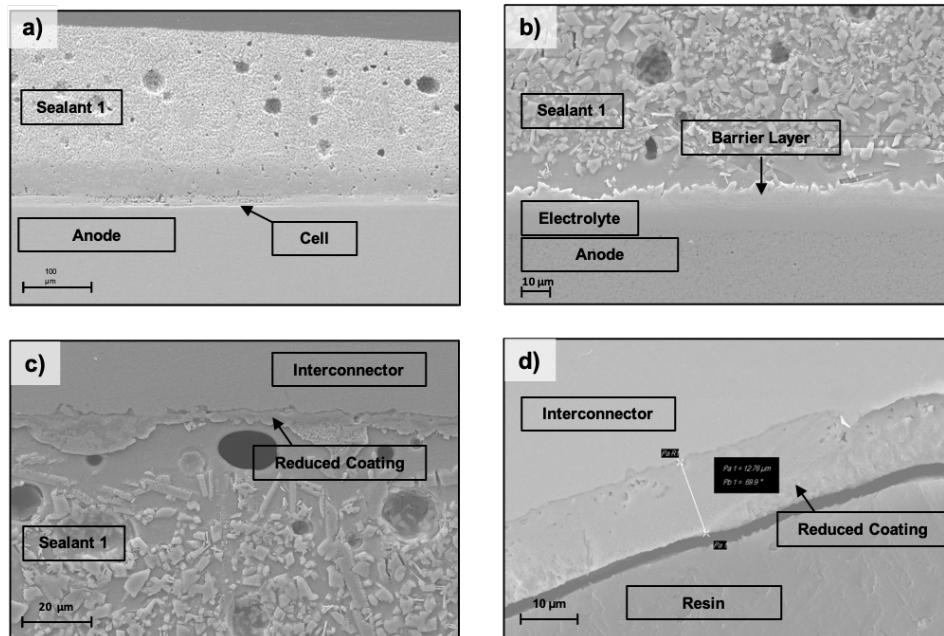


Figure 86: SEM pictures of the joined samples in the cathode side

4.2.4 Test 4

Test 4 has been prepared by using the sealant 2, deposited by robocasting deposition. The flatness of the system after assembling was satisfying to perform the electrochemical characterization of this SRU, as seen in the figure 33.

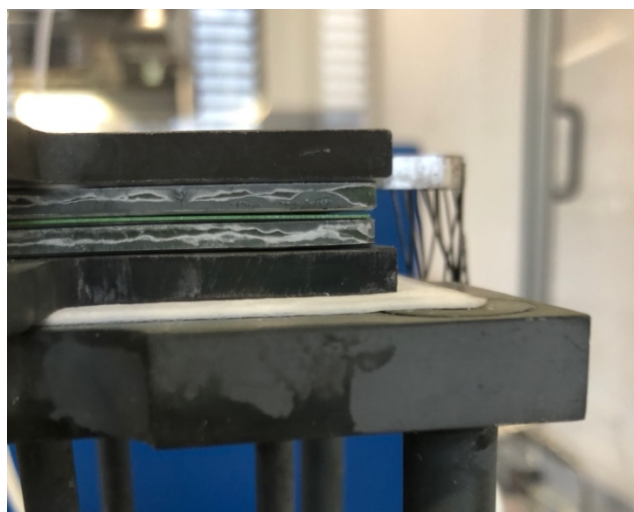


Figure 87: sandwich of all materials in the test 4

Electrochemical characterization

As in the test 3, the electrochemical characterization could be performed by mean of IV curves, EIS and durability test, all performed at 800°C.

Figure 88 shows different initial curves at three different gas conditions. In this case, the OCV values are close to 1,1 V, which is lower than for previous test but still in the range of acceptable values. Polarization curves present good values, reaching a maximum of 14,5 A at 0,65 V for the highest gas flows, corresponding to a power of 9 W. Moreover, it can be seen that adding N₂ to the anode gas atmosphere decreases the performance.

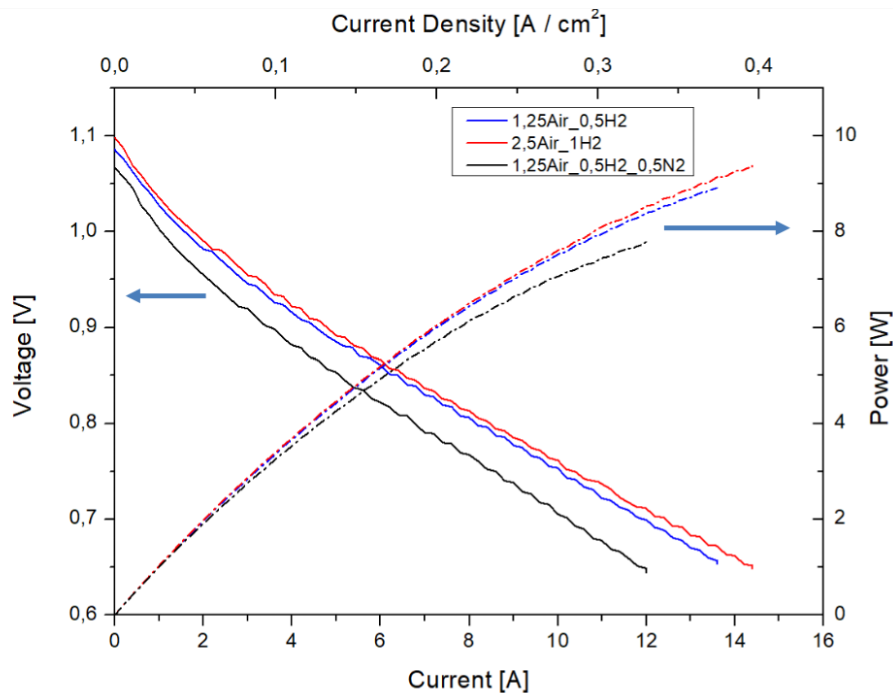


Figure 88: Polarization Curve of test 4.

In the following figure, it is possible to observe the EIS characterization, in particular the spectra obtained at OCV and under current with different gas conditions. In both cases it is clear that the serial resistance is not impacted by different gas condition, while the total resistance seems to change. In fact, the last semicircle changes with different gas condition. In particular, it is possible to see the influence of fuel electrode on the spectra, because in one case the air has been maintained at 1,25 l/min while on the other hand the anode atmosphere changed from H₂ to H₂+N₂. The amplitude of the semicircle rises as consequent. It means that the fuel electrode gas phenomena is limiting at low frequencies range.

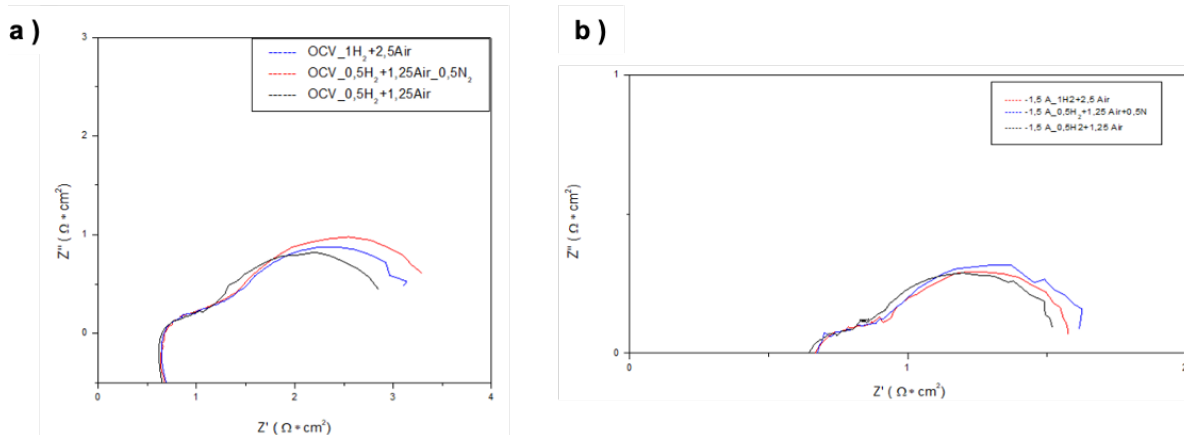


Figure 89: Curves EIS of the test 4 in OCV condition (a) and 2A condition (b).

The last test done in this SRU has been a degradation test. In this case 7,5 A has been applied for a long period of time (more than 800 hours). The details of this test, such as the working temperatures of 800 °C or the current density of 0,21 A/cm² are indicated on the same graph. However, in order to obtain more information about the degradation trends, some studies have been carried out, analyzing the different slopes. In the figure 90, 3 different slopes have been identified. In particular, it is possible to see that the first ramp has the rate degradation faster than the others. This is a typical from SOFC where faster initial degradations were widely reported. This degradation rate decreases from 8,4 % to 3,4 and 4,4 % afterward, which is still too high but promising for the future of this SRU.

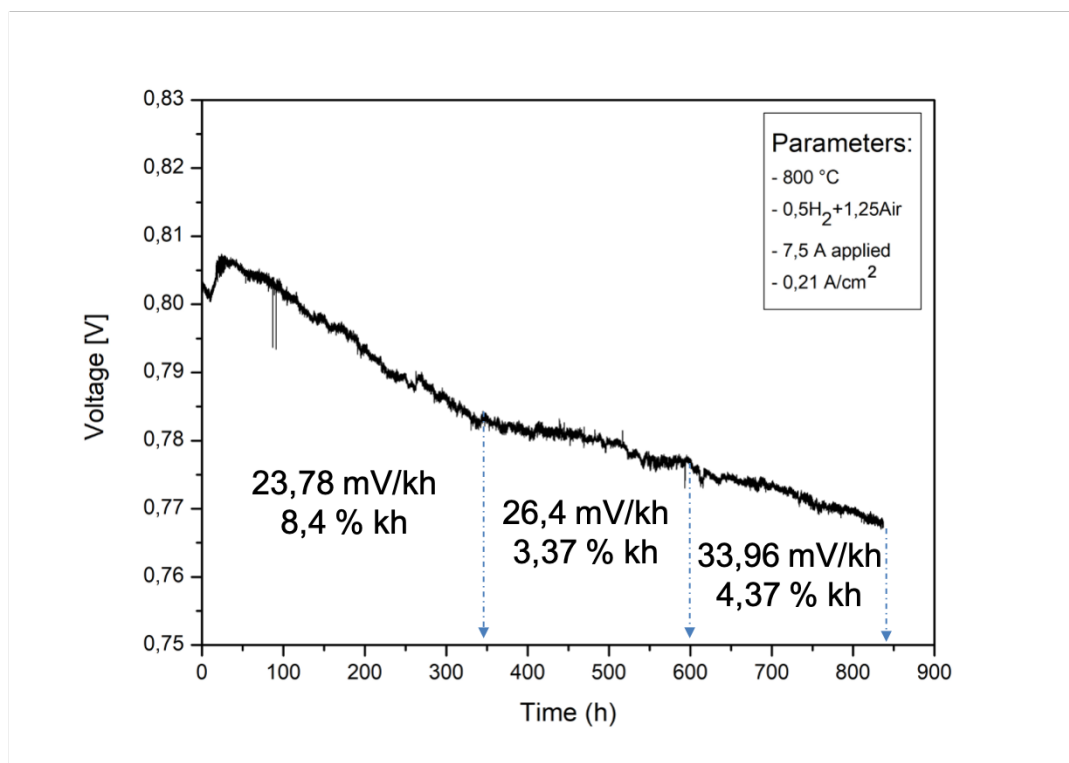


Figure 90: Whole degradation test of test 4.

In the figure 91, it is possible to observe the SRU performance after the degradation test. The value of OCV, which is around 1,05 – 1,1 V, is still comparable with the curve before the degradation.

However, in terms of polarization test, the curve after degradation shows a slightly decreased, with lower performance than the before, but still satisfactory in terms of current value and power.

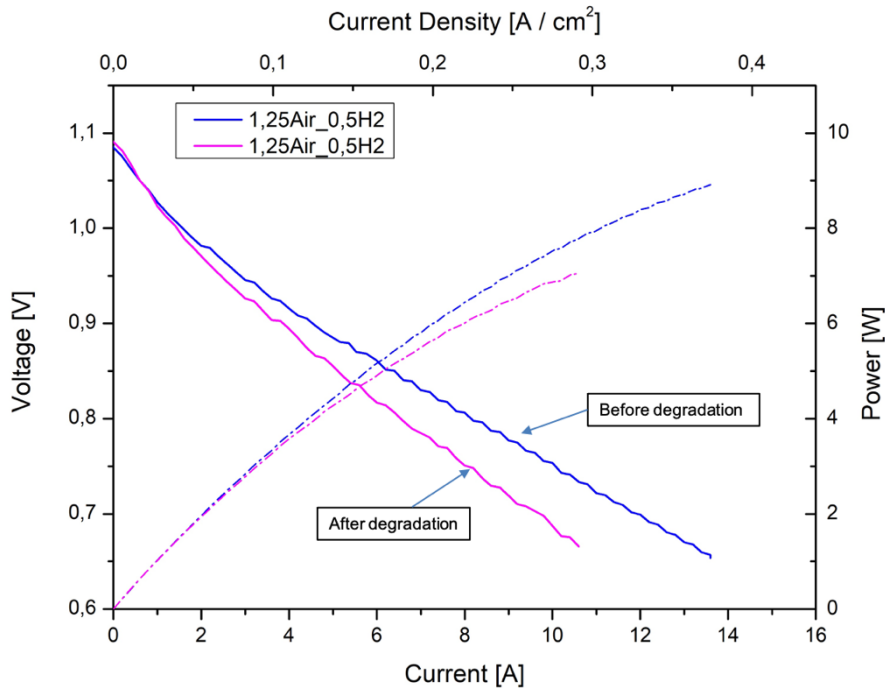


Figure 91: Polarization Curve of test 4, after and before the degradation test.

The last study conducted to characterize this SRU was carried out by the EIS curves at OCV and under current. In both graphs of *figure 92*, a slight shift of the whole spectra is observed without visible changes in terms of semi-circles' size. It corresponds to an increase of the serial resistance, which means a worsening in terms of electrolyte resistance and/or electrical contacts. The electrode performance doesn't seem to have been affected by the degradation. Taking into account that the cells used in this study are commercial and made with a thin layer of electrolyte, the increase in serial resistance is most likely coming from a degradation of the electrical contacts. In this case, it can correspond to the formation of insulating phase at some interlayers such as Cr_2O_3 . Post-mortem characterization of the SRU will be necessary to identify the origin of this degradation.

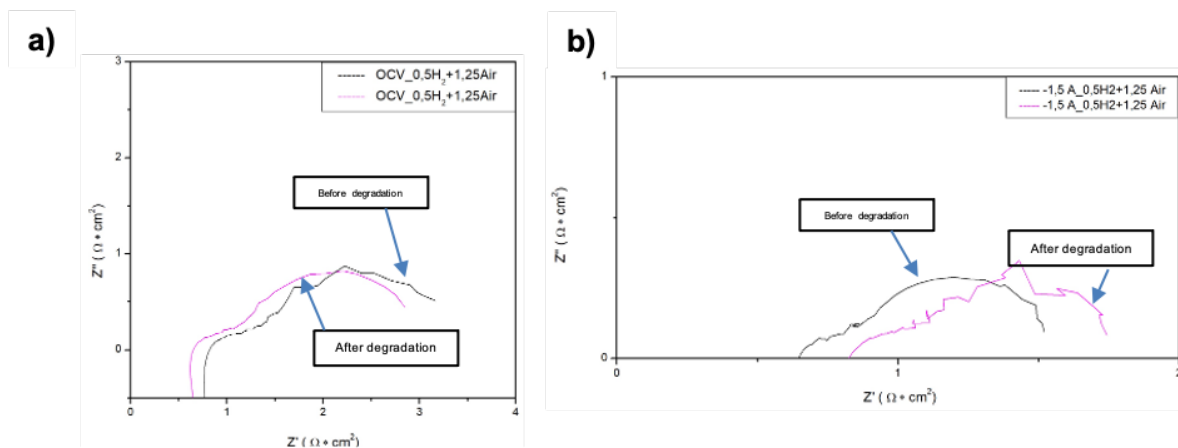


Figure 92: Curves EIS of the test 4 in OCV condition (a) and 2A condition (b).

5. Conclusions and future development

The aim of the present work was to implement the use of glass-ceramic sealants in the setup used for SOFC cells, SRU and stack tests at IREC. Two commercial sealants were taken into account, one produced by tape-casting (sealant 1) and another in form of powder (sealant 2, deposited by robocasting). As a first step the compatibility of these sealants with other materials involved in SRU/stack at IREC was tested. Both sealants showed excellent compatibility with all the interfaced counterparts: bare and coated Crofer22APU, bare and coated IC, anode of the cell, electrolyte of the cell. Sealant 1 partially crystallized in $\text{Ba}_3\text{Si}_2\text{O}_8$ after the joining thermal treatment, while sealant 2 led to the formation of SiO_2 and BaSiO_3 . The presence of cristobalite in the latter led to the formation of microcracks in the sealant that may be detrimental in real operating conditions. Despite this, sealant 2 was also successfully tested.

Large-area single cells and SRU were then tested in fuel cell mode. Single cell characterization was not successful probably due to gas overpressure leading to important leakages. However, those two first tests led to a better understanding of the setup and an improvement of tightening system. Finally, two SRU mounted with either sealant 1 or sealant 2 were successfully characterized. In both cases, good OCV values were obtained, corresponding to limited leakages between the anode and cathode chambers. This proves the effectivity of the tested glass-sealants. SRU performance was then satisfying even though a decrease of the serial and polarization resistance are still necessary. At last, a degradation test of 800 h could be performed for the SRU made with robocasted sealant 2. High degradation rate was observed during the first 300 h (8,4 %) and then decreased to 3-4 %, corresponding to an increase in serial resistance.

Thanks to the implementation of these sealants in the setup at IREC, as future development full stacks will be tested using both sealants. This allows the test in real operating conditions and on a real scale of different commercial and non-commercial components (i.e. interconnects coated by electrophoretic deposition).

6. Bibliography

- [4] Ireneusz Pielecha, January 2019, The potential of fuel cells as a drive source of maritime transport.
- [5] Lucia U. Overview on fuel cells. *Renewable and Sustainable Energy Reviews*. 2014;30:164-9.
- [6] A.ideris, 2014, Carbon Forn 0000096938 i Solid Oxide Fuel Cells (SOFCs) Using H 2 S by
- [8] N.Q. Minh, in *High-Temperature Solid Oxide Fuel Cells for the 21st Century*, 2016
- [10] K.C. Wincewicz, J.S. Cooper / *Journal of Power Sources* 140 (2005)
- [11] Keegan C. Wincewicz, Joyce S. Cooper, 8 august 2005, Taxonomies of SOFC material and manufacturing alternatives, *Journal of Power Sources*, 280-296
- [12] Abed Alaswad, ... Abdul G Olabi, in *Reference Module in Materials Science and Materials Engineering*, 2020
- [13] Keegan C. Wincewicz, Joyce S. Cooper, 8 august 2005, Taxonomies of SOFC material and manufacturing alternatives, *Journal of Power Sources*, 280-296
- [14] A. Stambouli, E. Traversa, Solid oxide fuel cells (SOFCs): a review of an environmentally clean and efficient source of energy, *Renew.Sustain. Energy Rev.* 6 (2002) 433–455.
- [15] M.H.PihlatieabA.KaiseraM.MogensenaM.Chena
- [17] Yesid-Gómez, Current developments in reversible solid oxide fuel cells, *Renewable and sustainable energy reviews* 61 (2016) 155-174
- [18] Lenser,2020,Solid oxide fuel and electrolysis cells
- [19] Anelli_2019_JMCA_Improved mesostructured oxygen electrodes for highly performing SOC for co-electrolysis of steam and carbon dioxide
- [20] W.J. Quadakkers, J. Piron-Abellan, V. Shemet & L. Singheiser (2003) Metallic interconnectors for solid oxide fuel cells – a review, *Materials at High Temperatures*, 20:2, 115-127
- [20] S.P.W. Badwal, 1 June 2001, Stability of solid oxide fuel cell components, volume 143, pages 39-46
- [22] I.BelogolovskyP.Y.HouC.P.JacobsonS.J.Visco, 15 July 2008, Chromia scale adhesion on 430 stainless steel: Effect of different surface treatments, Volume 182, Issue 1, Pages 259 – 264
- [23] Jeffrey W. Fergus, 25 April 2005, Metallic interconnects for solid oxide fuel cells,Volume 397, Pages 271-283

- [24] T. Brylewski, W. Kucka, A. Adameczyk, A. Kruk, M. Stygar, M. Bobruk, J. Dabrowa, November 2014, Microstructure and electrical properties of $Mn_{1+x}Co_{2-x}O_4$ ($0 \leq x \leq 1.5$) spinels synthesized using EDTA-gel processes, volume 40, pages 13873-13882
- [25] N. Shaigan, W. Qu, D.G. Ivey, W. Chen, A review of recent progress in coatings, surface modifications and alloy developments for solid oxide fuel cell ferritic stainless steel interconnects, *J. Power Sources*. 195 (2010) 1529–1542. doi:10.1016/j.jpowsour.2009.09.069.
- [26] A. Petric, H. Ling, Electrical conductivity and thermal expansion of spinels at elevated temperatures, *J. Am. Ceram. Soc.* 90 (2007) 1515–1520. doi:10.1111/j.1551-2916.2007.01522.x.
- [27] Y. Zhang, A. Javed, M. Zhou, S. Liang, P. Xiao, Fabrication of Mn-Co spinel coatings on Crofer 22 APU stainless steel by electrophoretic deposition for interconnect applications in solid oxide fuel cells, *Int. J. Appl. Ceram. Technol.* 11 (2014) 332–341. doi:10.1111/ijac.12013.
- [28] S.-I. Lee, J. Hong, H. Kim, J.-W. Son, J.-H. Lee, B.-K. Kim, H.-W. Lee, K.J. Yoon, Highly dense Mn-Co spinel coating for protection of metallic interconnect of solid oxide fuel cells, *J. Electrochem. Soc.* 161 (2014) F1389–F1394, <https://doi.org/10.1149/2.0541414jes>.
- [29] F. Smeacetto, A. De Miranda, S.M. Sandra Cabanas Polo, D. Boccaccini, M. Salvo, A.R. Boccaccini, Electrophoretic deposition of $Mn_{1.5}Co_{1.5}O_4$ on metallic interconnect and interaction with glass-ceramic sealant for solid oxide fuel cells application, *J. Power Sources*. 280 (2015) 379–386. doi:10.1016/j.ijhydene.2013.04.106.
- [30] P.A. Lessing, A review of sealing technologies applicable to solid oxide electrolysis cells, *J. Mater. Sci.* 42 (2007) 3465–3476. doi:10.1007/s10853-006-0409-9.
- [31] J.W. Fergus, Sealants for solid oxide fuel cells, *J. Power Sources*. 147 (2005) 46–57. doi:10.1016/j.jpowsour.2005.05.002.
- [32] F. Smeacetto, M. Salvo, M. Ferraris, J. Cho, A.R. Boccaccini, Glass – ceramic seal to join Crofer 22 APU alloy to YSZ ceramic in planar SOFCs, *J. Eur. Ceram. Soc.* 28 (2008) 61–68.
- [36] Roberto Spotorno, Marlena Ostrowska, Simona Delsante, Ulf Dahlmann and Paolo Piccardo, 22 October 2020, Characterization of Glass-Ceramic Sealant for Solid Oxide Fuel Cells at Operating Conditions by Electrochemical Impedance Spectroscopy.
- [37] Hassan Javed, Antonio Gianfranco Sabato, Kai Herbrig, Domenico Ferrero, Christian Walter, Milena Salvo, Federico Smeacetto, 21 February 2018, Design and characterization of novel glass-ceramic sealants for solid oxide electrolysis cell (SOEC) applications.

Sitography

- [1] <https://www.piemontetopnews.it/adattamento-ai-cambiamenti-climatici-un-convegno-a-torino/>

[2] <https://unfccc.int/process-and-meetings/the-paris-agreement/the-paris-agreement>

[3] <https://www.irena.org/climatechange>

[7] https://en.wikipedia.org/wiki/Solid_oxide_fuel_cell

[9] https://www.doitpoms.ac.uk/tlplib/fuel-cells/high_temp_sofc.php

[16] <https://www.globalsino.com/EM/page3136.html>

[33] <http://www.sofcman.com/asc.asp>

[34] https://www.vdmmetals.com/fileadmin/user_upload/Downloads/Data_Sheets/Data_Sheet_VD_M_Crofer_22_APU.pdf

[35] http://www.nordson.com/-/media/Files/Nordson/efd/Products/Manuals/Dispense-Robots/Nordson_EFD_EV_Series_Operating_Manual.pdf?la=en

7 Ringraziamenti

Questo percorso tortuoso è stato fondamentale per la mia crescita, sia a livello professionale, come a livello umano. Le persone da ringraziare sono molte. Comincio a parlare dei perni della mia vita, mamma e papà. Da voi ho imparato a superare le paure e le situazioni difficili. Costanza, sacrificio e perseveranza sono stati tre dei valori che voi mi avete insegnato e trasmesso, che mi hanno portato a celebrare questo momento. Quindi godetevi questa laurea, come se fosse la vostra.

Un pensiero va all'intera famiglia Foresta, la quale mi è sempre stata particolarmente vicino, con cui sono cresciuto e a cui devo molto.

Nonostante la distanza, ho avuto la fortuna di continuare a coltivare rapporti che ormai è possibile definire fraterni. Grazie mille Damiano per il supporto che mi hai costantemente dato, per i momenti gloriosi che mi regali ogni volta nella nostra terra e per la tua presenza in ogni momento della mia vita. Grazie Giuseppe per le mille avventure che mi regali da una vita, comprendendo larghe mangiate.

Ancora un grazie a tutti i miei professori del Politecnico di Torino, i quali mi hanno trasmesso passione, voglia ed interesse nei molteplici argomenti trattati durante la mia carriera universitaria. In particolar modo tengo a ringraziare i professori: Valeria Chiadò Piat, Daniel Milanese, Marco Sangermano, Daniele Ugues, Federico Smeacetto e Milena Salvo, i quali, per diverse ragioni, hanno inciso fortemente sulla mia carriera professionale e la mia crescita a livello umano.

Una delle cose più importanti che Torino mi ha regalato penso siano gli amici:

Grazie Giovanni, ormai più fratello che altro, per i bei momenti passati insieme a Torino e non.

Grazie a Giulio e Michele, compagni di studio di scienza delle costruzioni e mangiate natalizie giornalieri, non più "colleghi" ma amici.

Grazie al mio fedele coinquilino Ambrogio, palermitano DOC, con il quale ho avuto la possibilità di condividere momenti belli e brutti, motivandoci e rialzandoci a vicenda per ogni situazione.

Grazie al mio amico pseudo torinese dott.ing Alessandro pagano, con il quale ho condiviso diverse battaglie universitarie e per la splendida amicizia che si è creata in questi contesti bui e tenebrosi.

Grazie ad i miei amici torinesi Alessandro e Lorenzo, con i quali, oltre ad intense giornate di studio, abbiamo potuto condividere scambi culinari e paesaggistici (anche se la Sicilia vi sta ancora aspettando). Felice di avervi conosciuti, con la convinzione di poter mantenere i nostri "meeting" per i prossimi anni.

Grazie a tutti i miei colleghi, in particolare Romina, angelo sceso in terra, Simone, con il quale una risata non manca mai, Vito il napoletano, ai moschettieri Paolo ed Andrea, l'instancabile Marta, lo chef della casa Tonino, il compagno di risate Nicola, compare Erika, Mattia e tutti gli altri.

Grazie a tutto il team di IREC, che mi ha accolto e mi ha permesso di vivere una delle esperienze più belle della mia vita. Ringrazio particolarmente Gianfranco, tutor, consigliere ed amico, il quale mi ha saputo guidare egregiamente nel mio progetto di tesi e sempre pronto ad aiutarmi nei momenti difficili. Altro ringraziamento va alla mia tutor Lucile. Merci beaucoup pour ce que tu m'a enseigné et pour le rapport d'estime que nous avons créé.

Gracias a el mi hermano major Manuel, con quien he vivido esta mi experiencia española, estableciendo una hermosa relación que espero vas a durar. Siempre viva Andalucía.

Ed infine, grazie a chi mi protegge e mi ha aiutato da lontano.

Questo traguardo è grazie a voi.